



ELSEVIER

Available online at [www.sciencedirect.com](http://www.sciencedirect.com)

SCIENCE @ DIRECT®

**NUCLEAR  
INSTRUMENTS  
& METHODS  
IN PHYSICS  
RESEARCH**  
Section A

[www.elsevier.com/locate/nima](http://www.elsevier.com/locate/nima)

Nuclear Instruments and Methods in Physics Research A 527 (2004) 329–410

## Design, construction and tests of the ICARUS T600 detector

S. Amerio<sup>a</sup>, S. Amoruso<sup>b</sup>, M. Antonello<sup>c</sup>, P. Aprili<sup>d</sup>, M. Armenante<sup>b</sup>, F. Arneodo<sup>d</sup>, A. Badertscher<sup>e</sup>, B. Baiboussinov<sup>a</sup>, M. Baldo Ceolin<sup>a</sup>, G. Battistoni<sup>f</sup>, B. Bekman<sup>g</sup>, P. Benetti<sup>h</sup>, E. Bernardini<sup>d</sup>, M. Bischofberger<sup>e</sup>, A. Borio di Tigliole<sup>h</sup>, R. Brunetti<sup>h</sup>, R. Bruzzese<sup>b</sup>, A. Bueno<sup>e,i</sup>, E. Calligarich<sup>h</sup>, M. Campanelli<sup>e</sup>, F. Carbonara<sup>b</sup>, C. Carpanese<sup>e</sup>, D. Cavalli<sup>f</sup>, F. Cavanna<sup>c</sup>, P. Cennini<sup>j</sup>, S. Centro<sup>a</sup>, A. Cesana<sup>k,f</sup>, C. Chen<sup>l</sup>, D. Chen<sup>l</sup>, D.B. Chen<sup>a</sup>, Y. Chen<sup>l</sup>, R. Cid<sup>i</sup>, D.B. Cline<sup>m</sup>, K. Cieřlik<sup>n</sup>, A.G. Cocco<sup>b</sup>, D. Corti<sup>a</sup>, Z. Dai<sup>e</sup>, C. De Vecchi<sup>h</sup>, A. Dąbrowska<sup>n</sup>, A. Di Cicco<sup>b</sup>, R. Dolfini<sup>h</sup>, A. Ereditato<sup>b</sup>, M. Felcini<sup>e</sup>, A. Ferella<sup>c</sup>, A. Ferrari<sup>i,f</sup>, F. Ferri<sup>c</sup>, G. Fiorillo<sup>b</sup>, S. Galli<sup>c</sup>, D. Garcia Gamez<sup>i</sup>, Y. Ge<sup>e</sup>, D. Gibin<sup>a</sup>, A. Gigli Berzolari<sup>h</sup>, I. Gil-Botella<sup>e</sup>, K. Graczyk<sup>o</sup>, L. Grandi<sup>h</sup>, A. Guglielmi<sup>a</sup>, K. He<sup>l</sup>, J. Holeczek<sup>g</sup>, X. Huang<sup>l</sup>, C. Juszczak<sup>o</sup>, D. Kielczewska<sup>p,q</sup>, J. Kisiel<sup>g</sup>, T. Kozłowski<sup>p</sup>, H. Kuna-Ciska<sup>f</sup>, M. Laffranchi<sup>e</sup>, J. Łagoda<sup>q</sup>, Z. Li<sup>l</sup>, B. Lisowski<sup>m</sup>, F. Lu<sup>l</sup>, J. Ma<sup>l</sup>, G. Mangano<sup>b</sup>, G. Mannonchi<sup>s,t</sup>, M. Markiewicz<sup>n</sup>, A. Martinez de la Ossa<sup>i</sup>, C. Matthey<sup>m</sup>, F. Mauri<sup>h</sup>, D. Mazza<sup>c</sup>, A.J. Melgarejo<sup>i</sup>, A. Menegolli<sup>h</sup>, G. Meng<sup>a</sup>, M. Messina<sup>e</sup>, J.W. Mielinski<sup>n</sup>, C. Montanari<sup>h</sup>, S. Muraro<sup>f</sup>, S. Navas-Concha<sup>e,i</sup>, M. Nicoletto<sup>a</sup>, J. Nowak<sup>o</sup>, G. Nurzia<sup>c</sup>, C. Osuna<sup>i</sup>, S. Otwinowski<sup>m</sup>, Q. Ouyang<sup>l</sup>, O. Palamara<sup>d</sup>, D. Pascoli<sup>a</sup>, L. Periale<sup>s,t</sup>, G. Piano Mortari<sup>c</sup>, A. Piazzoli<sup>h</sup>, P. Picchi<sup>u,t,s</sup>, F. Pietropaolo<sup>a</sup>, W. Półchłopek<sup>v</sup>, M. Prata<sup>h</sup>, T. Rancati<sup>f</sup>, A. Rappoldi<sup>h</sup>, G.L. Raselli<sup>h</sup>, J. Rico<sup>e</sup>, E. Rondio<sup>p</sup>, M. Rossella<sup>h</sup>, A. Rubbia<sup>e</sup>, C. Rubbia<sup>h,\*</sup>, P. Sala<sup>f,e</sup>, R. Santorelli<sup>b</sup>, D. Scannicchio<sup>h</sup>, E. Segreto<sup>c</sup>, Y. Seo<sup>m</sup>, F. Sergiampietri<sup>m,w</sup>, J. Sobczyk<sup>o</sup>, N. Spinelli<sup>b</sup>, J. Stepaniak<sup>p</sup>, R. Sulej<sup>x</sup>, M. Szeptycka<sup>p</sup>, M. Szarska<sup>n</sup>, M. Terrani<sup>k,f</sup>, G. Trincheri<sup>s,t</sup>, R. Velotta<sup>b</sup>, S. Ventura<sup>a</sup>, C. Vignoli<sup>h</sup>, H. Wang<sup>m</sup>, X. Wang<sup>b</sup>, J. Woo<sup>m</sup>, G. Xu<sup>l</sup>, Z. Xu<sup>l</sup>, X. Yang<sup>m</sup>, A. Zalewska<sup>n</sup>, J. Zalipska<sup>p</sup>, C. Zhang<sup>l</sup>, Q. Zhang<sup>l</sup>, S. Zhen<sup>l</sup>, W. Zipper<sup>g</sup>

<sup>a</sup> *Università di Padova e INFN, Padova, Italy*

<sup>b</sup> *Università Federico II di Napoli e INFN, Napoli, Italy*

<sup>c</sup> *Università dell'Aquila e INFN, L'Aquila, Italy*

<sup>d</sup> *INFN—Laboratori Nazionali del Gran Sasso, Assergi, Italy*

<sup>e</sup> *Institute for Particle Physics, ETH Hönggerberg, Zürich, Switzerland*

<sup>f</sup> *Università di Milano e INFN, Milano, Italy*

<sup>g</sup> *Institute of Physics, University of Silesia, Katowice, Poland*

\*Corresponding author. Tel.: +41-22-7676338; fax: +41-22-7677960.

E-mail address: [carlo.rubbia@cern.ch](mailto:carlo.rubbia@cern.ch) (C. Rubbia).

<sup>h</sup> Dipartimento di Fisica Nucleare e Teorica, Università di Pavia e INFN, Via Bassi 6, I-27100 Pavia, Italy

<sup>i</sup> Dpto de Física Teórica y del Cosmos & C.A.F.P.E., Universidad de Granada, Granada, Spain

<sup>j</sup> CERN, Geneva, Switzerland

<sup>k</sup> Politecnico di Milano (CESNEF), Milano, Italy

<sup>l</sup> IHEP—Academia Sinica, Beijing, People's Republic of China

<sup>m</sup> Department of Physics, UCLA, Los Angeles, USA

<sup>n</sup> H.Niewodniczański Institute of Nuclear Physics, Kraków, Poland

<sup>o</sup> Institute of Theoretical Physics, Wrocław University, Wrocław, Poland

<sup>p</sup> A.Soltan Institute for Nuclear Studies, Warszawa, Poland

<sup>q</sup> Institute of Experimental Physics, Warsaw University, Warszawa, Poland

<sup>r</sup> Institute of Mechanics and Machine Design, Cracow University of Technology, Kraków, Poland

<sup>s</sup> IFSI, Torino, Italy

<sup>t</sup> INFN - Laboratori Nazionali di Frascati, Frascati, Italy

<sup>u</sup> Università di Torino, Torino, Italy

<sup>v</sup> University of Mining and Metallurgy, Kraków, Poland

<sup>w</sup> INFN, Pisa, Italy

<sup>x</sup> Warsaw University of Technology, Warszawa, Poland

Received 12 January 2004; received in revised form 6 February 2004; accepted 12 February 2004

## Abstract

We have constructed and operated the ICARUS T600 liquid argon (LAr) time projection chamber (TPC). The ICARUS T600 detector is the largest LAr TPC ever built, with a size of about 500 tons of fully imaging mass. The design and assembly of the detector relied on industrial support and represents the applications of concepts matured in laboratory tests to the kton scale.

The ICARUS T600 was commissioned for a technical run that lasted about 3 months. During this period all the detector features were extensively tested with an exposure to cosmic-rays at surface with a resulting data collection of about 30 000 events.

The detector was developed as the first element of a modular design. Thanks to the concept of modularity, it will be possible to realize a detector with several kttons active mass, to act as an observatory for astroparticle and neutrino physics at the Gran Sasso Underground Laboratory and a second-generation nucleon decay experiment.

In this paper a description of the ICARUS T600 is given, detailing its design specifications, assembly procedures and acceptance tests. Commissioning procedures and results of the technical run are also reported, as well as results from the off-line event reconstruction.

© 2004 Elsevier B.V. All rights reserved.

PACS: 14.60.P; 26.65; 96.60.J; 13.30; 14.20.D; 29.40; 29.40.G

Keywords: Liquid Argon; TPC; Calorimetry; Neutrino interaction; Nucleon decay

## 1. Introduction

The technology of the liquid argon time projection chamber (LAr TPC), first proposed by Rubbia in 1977 [1], was conceived as a tool for a completely uniform imaging with high accuracy of massive volumes. The operational principle of the LAr

TPC is based on the fact that in highly purified LAr ionization tracks can be transported practically undistorted by a uniform electric field over macroscopic distances. Imaging is provided by a suitable set of electrodes (wires) placed at the end of the drift path continuously sensing and recording the signals induced by the drifting electrons.

Non-destructive read-out of ionization electrons by charge induction allows to detect the signal of electrons crossing subsequent wire planes with different orientation. This provides several projective views of the same event, hence allowing space point reconstruction and precise calorimetric measurement.

The LAr TPC was developed in the context of the ICARUS programme and currently finds its application in studies concerning some of the major issues of particle and astroparticle physics:

- the study of solar and atmospheric neutrino interactions;
- the study of nucleon decay for some channels predicted by GUTs;
- the detection of neutrinos following a Supernova explosion;
- the study of neutrino oscillations with beams from particle accelerators.

After the original proposal, the feasibility of the technology has been demonstrated by an extensive R&D programme, which included 10 years of studies on small LAr volumes (proof of principle, LAr purification methods, read-out schemes, electronics) and 5 years of studies with several prototypes of increasing mass (purification technology, collection of physics events, pattern recognition, long duration tests, read-out technology). The largest of these devices had a mass of 3 tons of LAr [2,3] and has been operated continuously for more than 4 years, collecting a large sample of cosmic-ray and  $\gamma$ -source events. Furthermore, a smaller device (50 l of LAr [4]) was exposed to the CERN neutrino beam, demonstrating the high recognition capability of the technique for neutrino interaction events.

The main technological challenges of the ICARUS detection technique that have been addressed in the R&D studies are briefly summarized in the following [2,3,5–14]:

- (1) *Argon purification*: LAr must be ultra-pure, even in the presence of a large number of feedthroughs for the signals and the high voltage (HV), and with wire chambers, cables, etc. in the clean volume. The contamination of electronegative molecules must be as low as

0.1 ppb to allow drifts over long distances (meters) without capture of the ionization electrons. This has been achieved by using commercial gas purification systems to remove Oxygen and polar molecules ( $\text{H}_2\text{O}$ ,  $\text{CO}_2$ , fluorinated and chlorinated compounds) combined with ultra-high-vacuum techniques to avoid recontamination of the liquid through leaks and with the use of low outgassing materials for the detector components. Concentration of impurities at the level of  $\approx 0.1$  ppb or less are easily and constantly reachable. Liquid phase purification allows fast filling of large detectors. Continuous recirculation of the liquid through the purifier during normal operation is used to keep the lifetime stable (against micro-leaks and outgassing).

- (2) *Wire chambers*: the wire chambers must be able to perform non-destructive read-out with several planes with a few millimeters pitch; they have to be built out of non-contaminating materials and must stand the thermal stress of going from room to LAr temperature; the precision and the reliability of the mechanics has to be high, and a good knowledge of the electric field in the detector must be granted.
- (3) *Analog electronics*: in order to obtain high signal-to-noise ratio, very low noise pre-amplifiers must be developed. Since the signal is very small ( $\approx 15\,000$  electrons for a minimum ionizing track with 3 mm wire pitch) the equivalent noise charge has to be less than 1000 electrons. This has been reached by means of jFET technology.
- (4) *Data acquisition*: the ICARUS detector read-out system behaves like a large multi-channel waveform recorder. The digital conversion is performed by means of continuously active fast ADC sampling at a rate of 40 MHz. Taking into account the multiplexing of 16 channels, each channel is then sampled every 400 ns. The system effectively stores the charge information collected by each sense wire during a time corresponding to at least the maximum drift time of the electrons (few milliseconds). The high resolution that has to be achieved, both in space and time sampling,

brings the size of a single event to over hundreds of kilobytes. The useful signal occupies only a small fraction of the data sample. Although in the initial phases of the experiment the complete information is useful for troubleshooting and debugging purposes, this is the real bottleneck of the whole data taking system, overloading both the on-line and off-line processing. To speed up the performance of the detector and reduce the dead time, a great effort has been devoted to the development of the software architecture and the algorithms for data reduction.

Thereafter, the ICARUS project has entered an industrial phase, a necessary path to proceed towards the realization of large volume detectors for astroparticle and neutrino physics. The first step was the realization of a large cryogenic prototype (14 tons of LAr [15,16]) to test the final industrial solutions that were adopted. This detector was successively transformed into a module operated at the INFN Gran Sasso Laboratory (LNGS).

The second step was represented by the construction of the T600 module: a detector employing about 600 tons of LAr to be operated at LNGS. This step-wise strategy allowed to progressively develop the necessary know-how to build a multi-kton LAr detector.

The realization of the T600 detector (from design to construction) lasted about 4 years and culminated with a full test of the experimental setup, carried out at surface during 2001. This test demonstrated the maturity of the project. All technical aspects of the system, namely, cryogenics, LAr purification, read-out chambers, detection of LAr scintillation light, electronics and DAQ had been tested and performed as expected. Statistically significant samples of cosmic-ray events (long muon tracks, spectacular high-multiplicity muon bundles, electromagnetic and hadronic showers, low-energy events) were recorded. The analysis of these events has allowed the development and fine tuning of the off-line tools for the event reconstruction and the extraction of physical quantities. It has also demonstrated the performance of the detector in a quantitative way.

Beyond the T600, the ICARUS Collaboration has proposed an extension of the sensitive mass to about 3000 tons, also in view of the realization of experiments in the CNGS [17] neutrino beam from CERN to Gran Sasso, by cloning the present T600 module [18]. This scientific programme has been approved by both CERN and INFN.

The main goal of this paper is to give a description of the T600 detector and of its technical performance as obtained from acceptance tests. This description complements the experimental results obtained from the data collected during the test run. Such results are reported in a series of papers dealing with the following subjects:

- observation of very long ionizing tracks [19];
- analysis of the LAr purity in the T600 detector [20];
- study of ionization quenching in LAr [21];
- measurement of the muon decay spectrum [22];
- momentum estimation via multiple scattering [23].

The present paper is organized as follows:

- a basic outline of the detector is given in Section 2;
- a brief description of the relevant LAr properties is presented in Section 3;
- a detailed description of the various T600 components is provided in Sections 4–12. For all sections a brief presentation of the respective basic specifications is followed by a description of the design, of the components construction, of the results from acceptance tests and of the final assembly.

In particular:

- Section 4 is dedicated to the construction of the main LAr containers, of the cryogenics and of the purification plants;
- Section 5 presents the system for the LAr purification;
- the monitoring system for the LAr purity is described in Section 6;
- in Section 7 the inner-detector mechanical structure is presented, including the wire chambers;
- the system to read out the scintillation light in LAr is presented in Section 8;

- the auxiliary instrumentation to monitor the inner detector and its read-out system are described in Section 9;
- Section 10 is dedicated to the HV system providing the electric field for the electron drift;
- in Sections 11 and 12, respectively, the read-out electronics and the data-acquisition system are described;
- in Section 13 the external trigger system used to collect cosmic-ray events during the test run is described;
- a report on the test run is given in Section 14: commissioning and decommissioning procedures are described and the performance of the various detector components are presented and discussed;
- Section 15 contains a commented gallery of cosmic-ray events recorded during the data taking;
- the description of the basic off-line analysis tools to extract the physics information from the imaging is given in Section 16;
- conclusions are drawn in Section 17.

## 2. Detector overview

ICARUS T600 (Fig. 1) is composed of a large cryostat split into two identical, adjacent half-modules, each one with internal dimensions of 3.6 m (width)×3.9 m (height)×19.6 m (length). Each half-module houses an inner detector made of two TPC, the field-shaping system, monitors and probes, and of a system for the LAr scintillation light detection. The half-modules are externally surrounded by thermal insulation layers. In the following, we shall refer to each half-module as “T300”. The full-scale test reported in Section 14 was carried on after the commissioning of one T300.

Dimensions and shape of the cryostat were defined by the requirement that the LAr containers (cold vessels) had to be transported through the Italian highways into the underground Gran Sasso Laboratory and installed there. In order to collect significant samples of solar and atmospheric

neutrino events, the ICARUS Collaboration adopted a solution with two coupled containers with dimensions corresponding to a total LAr volume of about 550 m<sup>3</sup>.

Outside the detector are located the read-out electronics, on the top side of the cryostat, and the cryogenic plant composed of a liquid nitrogen (LN<sub>2</sub>) cooling circuit and of a system of purifiers needed to achieve the required LAr purity.

The inner detector structure of each T300 consists of two TPCs (called *left* and *right* chambers) separated by a common cathode. Each TPC is made of three parallel wire planes, 3 mm apart, oriented at 60° with respect to each other, with a wire pitch of 3 mm. The three wire planes of each TPC are held by a sustaining frame (Fig. 2) positioned onto the longest walls of the half-module. The total number of wires in the T600 detector is 53 248. The read out of the signals induced on the TPC wires by the electron drift allows a full three-dimensional (3D) image reconstruction of the event topology.

For each of the two volumes of the T600 cryostat the size of the inner volume and of the active volume<sup>1</sup> is given in Table 1. Fig. 1 shows some details of the system.

A uniform electric field perpendicular to the wires is established in the LAr volume of each half-module by means of a HV system, as required to allow and guide the drift of the ionization electrons. The system is composed of a cathode plane, parallel to the wire planes, placed in the centre of the LAr volume of each half-module at a distance of about 1.5 m from the wires of each side. This distance defines the maximum drift path (Fig. 2). The HV system is completed by field-shaping electrodes to guarantee the uniformity of the field along the drift direction, and by an HV feedthrough to set the required voltage on the cathode. At the nominal voltage of 75 kV, corresponding to an electric field of 500 V/cm, the maximum drift time in LAr is about 1 ms.

<sup>1</sup>The active volumes are defined as the parallelepipeds with the side surfaces equal to the wire chamber surface and with width equal to twice the distance between the first wire plane (0°) and the cathode.

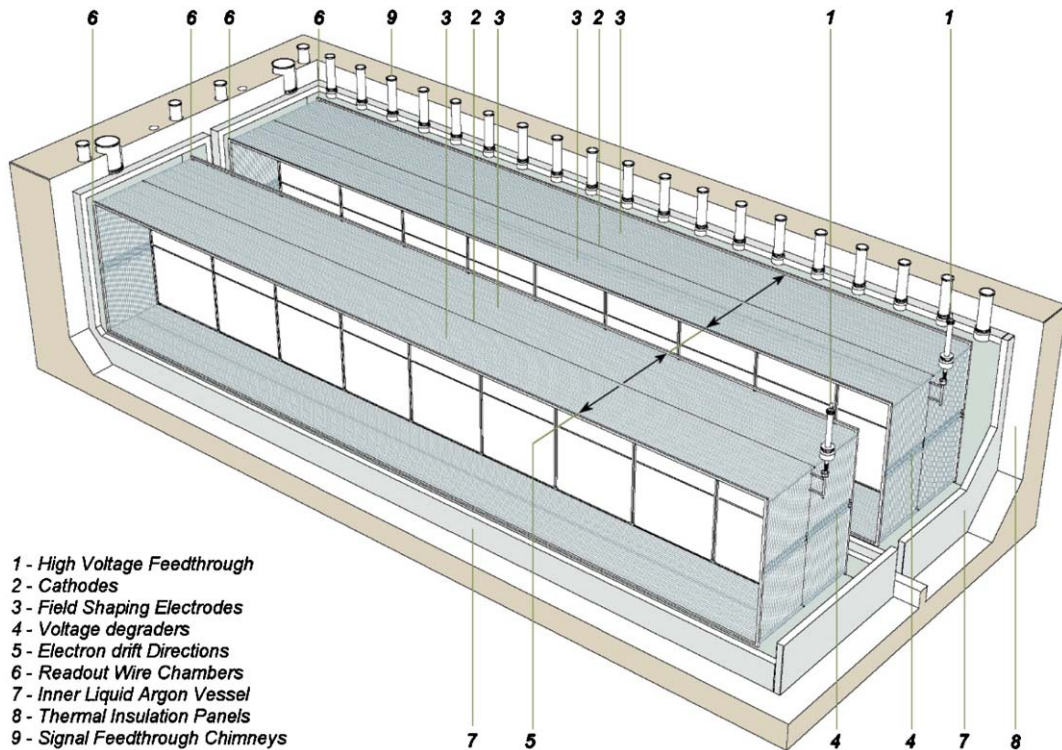


Fig. 1. Artist cutaway view of the ICARUS T600 detector.

The top side of the cryostat hosts the exit flanges equipped with cryogenic feedthroughs for the electrical connection of the wires with the read-out electronics, and for all the internal instrumentation (photo-multipliers (PMTs), LAr purity monitors, level and temperature probes, etc.).

The electronic chain is designed to allow for continuous read-out, digitization and waveform recording of the signals from each wire of the TPC. It is composed of three basic units serving 32 channels:

- (1) The decoupling board receives analog signals from the TPC wires via vacuum-tight feedthrough flanges and passes them to the analog board. It also provides biasing of the wires and distribution of calibration signals.
- (2) The analog board houses the signal amplifiers, performs 16:1 multiplexing and the data conversion (10 bit) at a 40 MHz rate.

- (3) The digital board uses custom programmable chips (two per board) specially developed for ICARUS, called DAEDALUS, that implement a hit finding algorithm. Each board receives the multiplexed digital data via an external serial-link cable.

Ionization in LAr is accompanied by scintillation light emission. Detection of this light can provide an effective method for absolute time measurement of the event as well as an internal trigger signal. A system to detect this LAr scintillation light has been implemented based on large surface (8 in.) PMTs directly immersed in the LAr.

The spatial reconstruction of ionizing tracks inside the LAr volume is performed by the simultaneous exploitation of the charge and of the light release following the energy loss processes of charged particles which cross the detector:

- (1) electrons from ionization induce detectable signals on the TPC wires during their drift



Fig. 2. Picture of the inner detector layout inside the first half-module: the cathode (vertical plane on the right) divides the volume in two symmetric sectors (*chambers*). The picture refers to the left sector where wires and mechanical structure of the TPC and some PMTs are visible.

motion towards and across the wire planes (wire coordinate);

- (2) UV photons from scintillation provide a prompt signal on the PMTs that allows the measurement of the absolute drift time and, hence, of the distance travelled by the drifting electrons (drift coordinate).

In this way, each of the planes of the TPC provides a two-dimensional projection of the event

image, with one coordinate given by the wire position and the other by the drift distance. The various projections have a common coordinate (the drift distance). A full 3D reconstruction of the event is obtained by correlating the signals from two different planes at the same drift distance.

The calorimetric measurement of the energy deposited by the ionizing particle in the LAr

Table 1  
Dimension of the inner and active volumes for each T300 half-module

Inner length	$L_I = 19\,600$ mm	$V_I = 275.2$ m <sup>3</sup>
Inner width	$W_I = 3600$ mm	
Inner height	$H_I = 3900$ mm	
Active length	$L_A = 17\,950$ mm	$V_A = 170.2$ m <sup>3</sup>
Active width	$W_A = 3000$ mm	
Active height	$H_A = 3160$ mm	
<i>Distance of active volume from</i>		
Front and back walls	$\Delta L_F = \Delta L_B = 825.0$ mm	
Left and right walls	$\Delta W_L = \Delta W_R = 300.0$ mm	
Top and bottom walls	$\Delta H_T = \Delta H_B = 370.0$ mm	

volume is obtained by collecting information from the last of the three wire planes, working in charge collection mode.

### 3. LAr as active medium

The motivations leading to the choice of the LAr as target material for a liquid TPC were clearly identified in the original ICARUS conceptual design paper [1]. These motivations are still valid. Quoting that document:

There are several reasons why pure LAr can be considered as an almost ideal material for a liquid target TPC: it is dense, it does not attach electrons and hence it permits long drift-times, it has a high electron mobility, it is easy to obtain and to purify, it is inert, it is cheap. ... From the physical point of view, LAr has properties which make it very similar to the freon of the celebrated Gargamelle experiment.

Free electron separation and scintillation light emission are the two processes that characterize the use of LAr as active medium. The average energy to produce an electron–ion pair is  $W_{\text{ion}} = 23.6$  eV, while the energy required for a scintillation photon emission is  $W_{\text{ph}} = 19.5$  eV. The two processes are complementary and their relative weight depends on the actual strength of the

electric field applied to the active LAr volume. The free-electron yield (ionization) rises with the field value while the photon yield (scintillation) decreases. In both cases saturation occurs for fields higher than  $\sim 10$  kV/cm. At the nominal value of 500 V/cm both processes are active.

Charge collection and track imaging is performed by the TPC wire planes biased at suitable voltage. Track charge collection is affected by electron–ion recombination processes, initial (or geminate) recombination and columnar recombination. Suitable models have been developed to describe the recombination factors in LAr as a function of the particle stopping power and of the drift electric field [21].

The scintillation light emission in LAr has been investigated in great detail by many authors since the pioneering studies of Doke et al. [24]. A narrow-band intrinsic VUV light (around 128 nm) is observed in LAr. It is explained as the radiative decay of excited molecules ( $\text{Ar}_2^*$ ) produced by ionizing radiation, which emit ultra-violet photons in transitions from the lowest excited molecular state to the dissociative ground state. Detection of the scintillation light is provided by the array of PMTs immersed in LAr, coated with a proper fluorescent compound acting as wavelength shifter from the VUV-light region to the PMT-sensitive spectrum.

A collection of the main physical [24–26], chemical [25,27] and thermal [25,28] properties of LAr is reported in Tables 2 and 3.

#### 4. The LAr cryostats

The dimensions, shape, material and, related to all these factors, the choice of the production

Table 2  
(I) LAr chemical and physical properties [24–27]

Atomic number, mass	18, 40
Atomic weight	39.948 $m_u$
$\langle Z/A \rangle$	0.45059
Concentration in air	0.934%
$W_{\text{ion}}$ (1 MeV $e^-$ )	23.6 eV
Energy loss $\langle dE/dx \rangle$ (minimum ionizing particle)	1.519 MeV $\text{cm}^2/\text{g}$
Critical energy (electrons)	31.7 MeV
$W_{\text{ph}}$ (1 MeV $e^-$ )	19.5 eV
Photon yield—scintillation—at 128 nm) (0-field)	$\sim 4.0 \times 10^4$ ph/MeV
Decay time constants	$\sim 6$ ns (23%), $\sim 1.6$ $\mu\text{s}$ (77%)
Radiation length	19.55 $\text{g}/\text{cm}^2$
Molière radius	12.95 $\text{g}/\text{cm}^2$
Nuclear interaction length	117.2 $\text{g}/\text{cm}^2$
Max breakdown strength (depending on purity level)	1.1–1.4 MV/cm
Dielectric constant at 128 nm (550 nm)	1.9 (1.5)
Refractive index at 128 nm (550 nm)	1.38 (1.23)
Rayleigh scattering length at 128 nm (550 nm)	0.9 m ( $10^3$ m)

Table 3  
(II) LAr thermal and physical properties [27,28]

	Pressure (bar)	Temperature (K)	Density ( $\text{g}/\text{cm}^3$ )
Solid phase		83.0	1.625
Triple point	0.689	83.8	
Liquid phase	1.00	87.2	1.396
Boiling point (at 1 atm =)	1.013	87.3	1.395
	1.15	88.5	1.388
	1.20	88.9	1.385
	1.25	89.3	1.383
Critical point	48.63	150.7	0.553
Heat capacity ( $C_p$ ) (boiling point)	0.2670 cal/g K		
Thermal conductivity (boiling point)	$3.00 \times 10^{-4}$ cal/s cm K		
Latent heat of vapourization (boiling point)	38.4 cal/g		
Gas/liquid ratio (1 atm, 15°/BPT)	835 vol/vol		
$e^-$ Mobility (boiling point)	500 $\text{cm}^2/\text{V s}$		
$e^-$ Drift velocity (500 V/cm—nominal field, 89 K)	1.55 mm/ $\mu\text{s}$		
$e^-$ Diffusion coefficient (89 K)	4.8 $\text{cm}^2/\text{s}$		
$e^-$ -O <sub>2</sub> trapping rate (500 V/cm, 89 K)	$\sim 7 \times 10^{10}$ l/mol s		

technology of the ICARUS cryostats are defined by the requirement that the LAr containers have to be transported through the Italian highways, to pass through the entrance gate of the underground Gran Sasso laboratory and to be installed in the laboratory Hall B. The basic constituents of the T600 cryostats are the aluminium LAr containers, the thermal insulation and the cooling system. They are described in detail in the following subsections.

##### 4.1. The aluminium containers of the LAr

The LAr containers are of parallelepiped shape with external dimensions of  $4.2 \times 3.9 \times 19.9 \text{ m}^3$  (Fig. 3). The basic elements of the cold vessels are panels with a thickness of 150 mm and a surface of  $2.0 \times 3.9 \text{ m}^2$  in the case of side walls and a surface of  $2.0 \times 3.6 \text{ m}^2$  in the case of top and bottom walls. They are made of aluminium honeycomb, surrounded by frames of aluminium profiles and sandwiched between two aluminium skins (Fig. 4). The main characteristics of the panels are listed in Table 4.

For the first half-module cooling pipes for LN<sub>2</sub> circulation are directly inserted in the middle of the panel honeycomb structure. Aluminium honeycomb is perforated to allow the circulation of



Fig. 3. Inner view of one of the two cryostats during construction. The side, bottom and top walls, their construction panels and angular frames, the backward end cap and the holes in the top wall are visible.

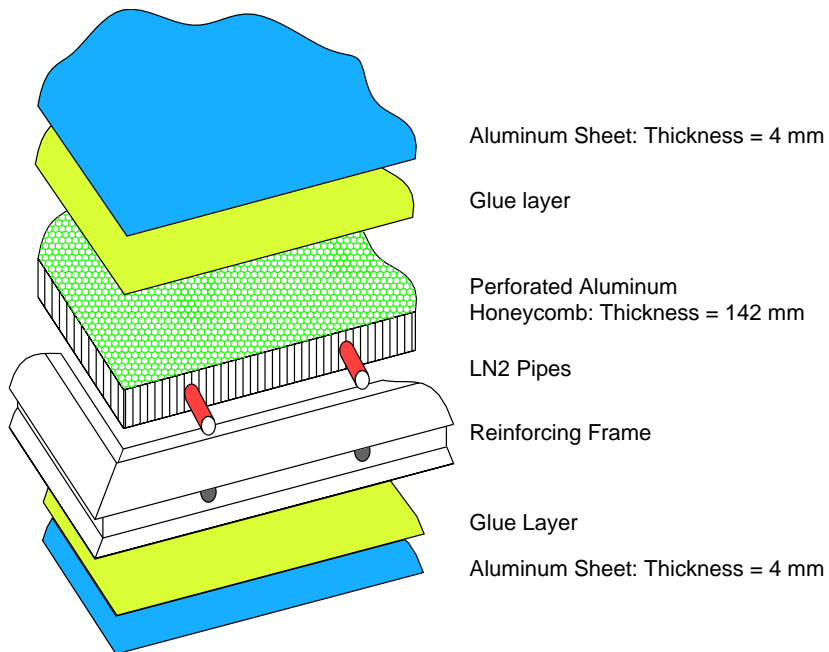


Fig. 4. Cross-section of the basic aluminium panel with cooling pipes going through the honeycomb structure.

Table 4  
Main characteristics of the aluminium honeycomb panels

Dimensions	
Side walls	$1873.5 \times 3816 \times 150 \text{ mm}^3$
Top and bottom walls	$1873.5 \times 3516 \times 150 \text{ mm}^3$
End caps	$1500 \times 3816 \times 150 \text{ mm}^3$
Thickness of the skins	4 mm
Thickness of the honeycomb aluminium type	142 mm UNI 3104
Mean density	$\sim 0.35 \text{ g/cm}^3$

nitrogen gas or evacuation of the whole panel. Connections between adjacent panels is performed by simultaneous welding of the skins and the aluminium profiles underneath (Fig. 5). Ten panels form a wall. The walls are connected by means of angular frames, also made of aluminium profiles.

According to the past experience with prototypes, the cold vessels must be evacuated to about  $10^{-4}$  mbar or better, in order to efficiently out gas the inner detector surfaces and to attain the required LAr purity. This implies that the containers have to mechanically stand the vacuum and that they have to be tight to better than  $10^{-2}$  mbar l/s. Maximum overpressure inside the cold vessels is limited to less than 1.5 bar abs. Wall position meters monitor inward and outward deformations during the different detector operations (Section 9.2).

The two end caps ( $3.6 \times 3.9 \text{ m}^2$ ), both formed by two special panels joined by an H-shaped profile, are added at the end. One end cap (the backward one) is welded to the side walls through angular profiles, while the other one is removable in order to allow the installation of the inner detector. On the front side there is a flange with the same dimensions as the cryostat, and the end cap is bolted on it. A thin aluminium plate welded all around the flange ensures the vacuum tightness of the container. The aluminium plate has to be cut and the bolts removed in order to open the vessel.

Particularly important for the mechanical resistance of the panels is the connection between the honeycomb and the surrounding frame, especially



Fig. 5. Detail of the assembly of the aluminium panels to form the cryostat walls.

in the regions near the corners of the cryostat. In these regions the shear stresses are the largest. In order to increase the safety factor, 10 mm thick aluminium plates were added to the panels in the connection regions. The plates covering a length of 500 mm close to the edges were glued on both sides of the panels after their assembly.

Holes for the way out of signal cables (Section 7.5) of the internal detectors and control instrumentation are located on the ceiling of the container, in correspondence with the two frames of the wire chambers. For each container there are 36 holes of 200 mm diameter and four holes of 250 mm diameter at the corners. The holes are equally spaced, 1 m from each other, and are arranged in two rows along the long sides of the top wall.

The ports for LAr filling, gaseous argon (GAr) recirculation and other services like vacuum instrumentation and safety disks, as well as two

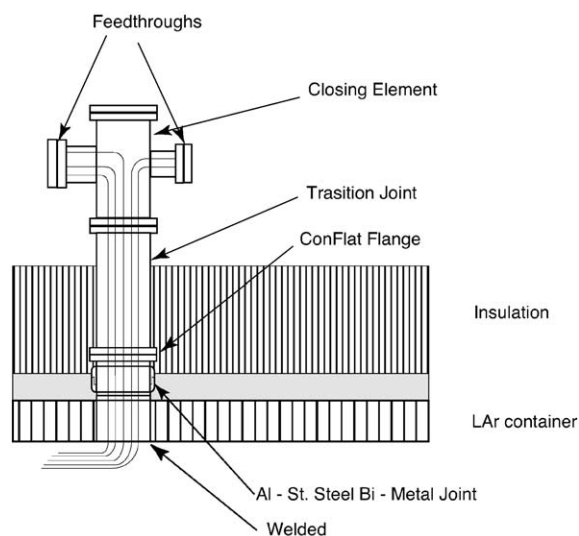


Fig. 6. Drawing scheme of the DN200CF ports for wire chamber read-out.

flanges (manholes) of 500 mm diameter used for inspection and for the final assembly operations, are also located on the top side. The output port to the LAr recirculation system is approximately at the centre of the backward end cap. Finally, a hole in the backward bottom edge is used to empty the container.

On each hole of the LAr containers special vacuum-tight, bi-metal (aluminium to stainless-steel) joints are mounted with the inner aluminium part welded to the container body and the outer stainless-steel part machined as a standard ConFlat flange (Fig. 6). Feedthrough flanges are mounted outside the insulation, at room temperature.

Ten special inserts (laminated aluminium pads) are mounted in the container bottom wall in correspondence of the stainless-steel feet of the wire chambers structure. They are placed in two rows of equally spaced points and were machined after the assembly of the whole container to attain the required mutual alignment and planarity of  $\pm 2$  mm. The feet are adjustable in order to allow for longitudinal and transverse movements (Section 7.1) to compensate differential thermal contractions of the stainless-steel structure and of the aluminium container.

The LAr containers were assembled in a workshop of the Air Liquide company.<sup>2</sup> All the welds, apart from those of the bi-metal joints, were tested for helium tightness by vacuum pumping in the volume of the walls themselves. It is worth noting that since the aluminium honeycomb is perforated, the walls and the removable end cap constitute a completely interconnected, tight volume. All detected leaks were repaired down to the sensitivity limit of the leak detector ( $\sim 10^{-8}$  mbar l/s).

The surfaces of the container were finally subject to pickling, by using a diluted solution of nitric acid, and to passivation. They were rinsed with demineralized water and dried with clean air. The containers were then completely sealed and the final acceptance test was performed by vacuum pumping of the whole container volume. After 36 h of pumping the vacuum was  $10^{-4}$  mbar.

#### 4.2. Thermal insulation

The solution adopted for the thermal insulation layer is based on passive honeycomb structures made of Nomex, a kind of non-flammable, pre-impregnated paper. The size of the honeycomb cells, or more appropriately, the ratio between the cross-section and the length, is chosen in such a way that air convective motions into the cells are largely suppressed.

The basic elements of the thermal insulation layer (Fig. 7) are pre-assembled panels with dimensions of 4.5 m (height)  $\times$  2 m (width)  $\times$  0.465 m (thickness) made of Nomex honeycomb sandwiched between an external aluminium skin (2 mm thick) at room temperature and an internal layer made of Kevlar cross-fibres in Epoxy resin, at LAr temperature. The inner, Kevlar reinforced skin was introduced to minimize thermal contraction of the internal side of the insulation layer, in order to reduce the relative displacements between adjacent panels during and after the cool down. An additional panel made of perforated aluminium honeycomb is inserted in the middle of the insulation panels.

The cryostat supports in the form of I-shaped stainless-steel beams, 0.48 m height and 21 m long,

<sup>2</sup> Air Liquide Italia, Pero (Milan), Italy.

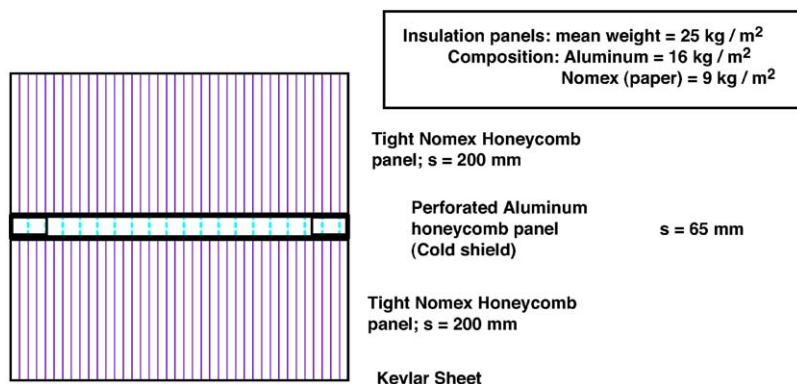


Fig. 7. Basic structure of the insulation panels.

were anchored to the hall floor by means of chemical expansion joints and roughly aligned to  $\pm 10$  mm with respect to the horizontal plane. Single insulation panels were joined together by aluminium plates (10 mm thick and 100 mm wide) screwed on the external skins of two adjacent panels, to form a  $5 \times 21$  m<sup>2</sup> long wall. Two such walls were positioned on the cryostat supports and then joined together by means of aluminium plates to constitute the insulation basement with a surface of  $10 \times 21$  m<sup>2</sup>.

The LAr container supports, made of stainless-steel hemispherical heads, were then installed on sliding rails, placed on the insulation basement in correspondence to the cryostat supports. The rails allow the reciprocal movements between the insulation and the LAr containers caused by differential thermal contractions. For both containers, fixed positions are those near the centre of the insulation basement. The set of four internal supports could slide only along the long cryostat axis (of 21 m length), while the five external supports could move on the horizontal plane. The empty space between the insulation basement and the bottom walls of LAr containers was filled, before the positioning of the LAr containers on their supports, with 40 mm thick, low-density polyurethane foam panels.

After positioning and alignment of the LAr containers, the work on the insulation of the side and top walls was performed. Additional 40 mm thick panels made of polyurethane foam were glued on the walls to partially fill the empty space

between the main insulation and the containers. A structure made of INVAR profiles, lining on the bottom insulation layer, was installed in the interspace between the two LAr containers, to sustain the two halves of the top insulation layer. This makes the insulation structurally independent from the inner LAr containers.

The chimneys, i.e. the stainless-steel, straight joints for the signal cables of the wire chambers and other internal instrumentation as well as for the nitrogen and argon transfer lines, were installed on the ceiling of the container, in correspondence with the holes, to be passed through the insulation (Fig. 6). Side and top insulation layers were then assembled in a similar way as for the bottom layer. A series of vetronite tie rods were used to connect and tighten the side with the top and bottom layer. Aluminium plates, 10 mm thick and 40 mm wide, screwed on the corners were added to connect the side to the top and bottom walls and to close the external surface.

Extra space in the holes around the joints for the transfer lines and for the signal cables was filled with small, expanded polyurethane spheres enclosed into polyethylene bags. Flexible, rubber joints, tied to the transfer lines or to the chimneys were used in addition, closing the insulation in these regions but at the same time allowing for mutual movements between the insulation and the transfer lines due to thermal contraction. After complete assembly of the insulation, low viscosity polyurethane foam was injected (by using hot

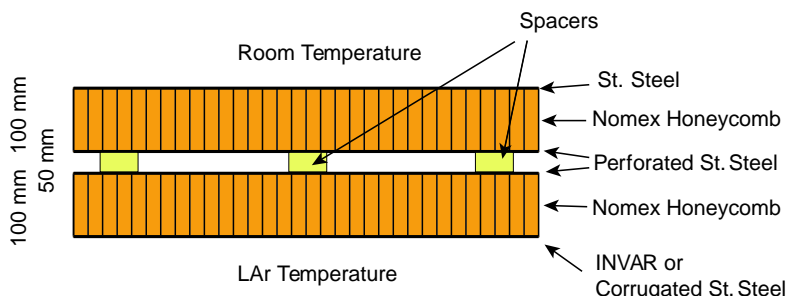


Fig. 8. Schematic drawing of the evacuated insulation panels.

water as solvent) into “ad hoc” holes located near the bottom layer, to fill all the remaining empty space between adjacent panels and between the insulation and the LAr containers. The foam dried in about 1 month after injection.

During the T600 tests in Pavia also a different, more advanced thermal insulation was tried in order to test its performance for future implementations. It is based on evacuated, honeycomb-structured insulation panels (Fig. 8). Two Nomex honeycomb panels, which are 100 mm thick and have metal sheets glued on their surfaces, are separated by a set of polyethylene spacers.

Three such panels with dimensions of 6.0 m (length)  $\times$  4.5 m (height)  $\times$  0.2 m (thickness) were installed on the side wall near the second half-module. The panels had been pre-assembled in the Air Liquide workshop, tested for vacuum tightness, evacuated, sealed and then delivered to the assembly hall in Pavia. After installation the panels were connected to three rotary vacuum pumps and remained under pumping until the end of the test run. According to the results of measurements and computations the performance of the evacuated panels is three times better than that of the former panels, as the thermal conductivity decreases from the initial 22 to about  $7 \text{ W/m}^2$  for the evacuated panels, when going from the room to the LAr temperature.

#### 4.3. Cooling system

The main requirement for the cooling system is to keep the LAr temperature uniform and stable within  $1^\circ\text{C}$ . This is needed to avoid changes with

temperature of the electron drift velocity and to prevent large convective motions inside the LAr volume. A set of platinum resistors was installed inside the cryostat for precise temperature monitoring over the whole detector volume (Section 9.4).

Cooling of the cryostat is performed by circulating pressurized  $\text{LN}_2$  at 2.7 bar abs and nominal temperature of 89 K, inside the cooling circuits of the two LAr containers. The circulation speed is defined by the request to maintain a maximum thermal gradient lower than  $1^\circ\text{C}$  on the nitrogen circuit.

Taking into account the actual thermal losses of the insulation, this leads to a  $\text{LN}_2$  circulation speed of about  $10 \text{ m}^3/\text{h}/\text{LAr}$  container, i.e. of  $8000 \text{ kg}/\text{h}/\text{LAr}$  container. The corresponding  $\text{LN}_2$  consumption due to the power injected by the circulation pumps themselves is about 25% of the total  $\text{LN}_2$  consumption, as verified during the runs of the  $10 \text{ m}^3$  prototype [15].

The cooling circuits of the first and of the second half-module are different. The first one is based on aluminium pipes inserted in the middle of honeycomb panels of the LAr container (Fig. 4). It offers the advantage of a compact and elegant solution which also minimizes the number of operations to be performed outside the manufacturer workshop. However, this solution has two main disadvantages which led us to abandon it for the second half-module. The first disadvantage is that once the LAr container is completely assembled, the circuit is no longer accessible for inspection or repair. The second one is that, due to the tight mechanical coupling between the circuit and the

LAr container structures, one is forced to follow a very slow cooling down procedure to prevent possible stresses caused by a thermal shrinking of the circuit faster than the one of the container structure. The cooling circuit adopted for the second half-module envisages a standard solution for the cooling shield which surrounds the whole LAr container.

Cooling circuits for both half-modules are described more in detail in the following. Aluminium pipes of the circuit of the first half-module are at a distance of about 60 cm from each other. There are two pipes per panel crossing the honeycomb cells and one pipe which passes through the aluminium profiles of each frame connecting two adjacent panels. According to simulations, the gradient in the regions between the cooling pipes is lower than  $0.1^{\circ}\text{C}$ .

The pipes are interconnected with collectors and corner joints in such a way that the complete circuit is subdivided into three parallel branches. One of the branches is C-shaped and covers the bottom, external side and top walls, in sequence. The second branch is for the two end caps, while

the third one is for the internal side wall (the one in front of the second T300).

The cooling shield of the second T300 is made of preformed aluminium panels joined together to form a sort of “skin” surrounding the whole LAr container at a distance of about 4 cm. The dimensions of the cooling panels are  $100 \times 40 \times 1 \text{ cm}^3$ . The resulting circuit has a conductance much larger than the one of the cooling circuit of the first half-module. For the test run operation, a pure  $\text{LN}_2$  circulation was implemented (Fig. 9). However, thanks to the large conductance of the cooling shield, a two-phase gas and  $\text{LN}_2$  circulation can be envisaged with two major advantages with respect to a pure liquid circulation:

- excellent temperature uniformity ensured by the thermal equilibrium between gas and liquid phase;
- much lower mass circulation with respect to the pure liquid phase circulation, with considerable savings on the  $\text{LN}_2$  consumption due to a much lower power injected by the Nitrogen circulation pumps.



Fig. 9. Detail of the cryostat insulation and cooling system.

The minimum circulating gas-to-liquid mass ratio is about five, in order to ensure saturated gas properties, i.e. the thermal equilibrium with liquid. Taking into account the expected thermal losses from the insulation (for the evacuated panel solution) the estimated LN<sub>2</sub> mass circulation speed is only about 600 kg/h/LAr container, while the volume circulation speed of gaseous nitrogen is about 30 m<sup>3</sup>/h/LAr container. This solution is foreseen for the T600 operation at LNGS.

The cooling shield of the second half-module is subdivided into four sections in which the cooling nitrogen flows in parallel. One section covers the front and backward walls, while other three, C-shaped, cover the bottom, side and top walls. Single panels of the cooling shield were pre-assembled on light aluminium frames (for transportation and handling) into shielding sections of about 4 × 4 m<sup>2</sup>. Each section was tested for helium tightness before delivery. The cooling shield was finally assembled on the second half-module in the assembly hall in Pavia. After assembly it was tested both for vacuum tightness and for over-pressurization to 9 bar abs (the maximum operating pressure is 6 bar abs, the normal operation is at 4.5 bar abs).

The cooling circuit has three additional branches per LAr container serving, respectively, the two gaseous Ar recirculation units and the LAr recirculation plus the main purifier units. The cooling nitrogen is injected by the circulation pumps into a common collector running around the two containers (externally to the insulation) at the bottom level. The nitrogen flow is then shared between the different circuit branches and is recuperated by a common collector placed outside the insulation, running around the two containers at the top level.

A set of proportional-aperture valves placed at the exit of each circuit section is used to regulate the relative amount of nitrogen flowing into the different branches. After the cryostat cooling down the aperture of the valves is manually regulated on the basis of the temperature read-out at the exit point of the different branches. Once the temperatures are set to the desired values, the valve aperture is definitively fixed. For the two GAR recirculation units, the flow into

the cooling circuit is regulated in order to yield the desired recirculation speed.

Two standard LN<sub>2</sub> cryogenic circulation pumps are installed. The speed (24 m<sup>3</sup>/h, nominal maximum) and prevalence (5 bar maximum) are regulated by a variable aperture bypass and a frequency controller (inverter). During normal, steady-state operation, the two pumps run in parallel. In case of stoppage of one of the two pumps (for maintenance or replacement) the speed of the second one is doubled and the circuit is automatically switched to operation with a single pump. The circulation pumps are fed in by a small buffer dewar of 800 l which in turn is filled by the primary LN<sub>2</sub> storage tanks, two of 20 000 l each. The pressure in the buffer dewar is regulated to the desired value in order to set the temperature of the circulating LN<sub>2</sub> (89 K for the normal working conditions).

The nitrogen return flow is sent back to the buffer dewar through a pressure-regulated proportional valve. The pressure upstream of the valve is set in a way to ensure that the nitrogen remains liquid all over the circuit (typical pressure is 3.5 bar abs). Behind the valve, the LN<sub>2</sub> separates into two phases. The excess gas is exhausted while the liquid returns to the circulating flow. This describes the steady-state cooling operation. During detector start-up a different two-step procedure is followed.

## 5. LAr purification

The basic requirements of the purification system can be summarized stating that: the system has to be able to purify and keep pure LAr with a concentration of electronegative impurities lower than 0.1 part per 10<sup>9</sup> (ppb) O<sub>2</sub> equivalent for a period of several years.

A few features extensively studied with prototypes have driven the basic choices:

- by using standard procedures for high vacuum (suitable materials, cleaning, design of internal components) and vacuum conditioning of the internal surfaces, a high LAr purity after filling can be achieved;

- pollution of the LAr is mainly due to outgassing of the inner surfaces in contact with the GAr, while contamination from objects immersed in the liquid is negligible; in the absence of large convective motions, recirculation of the gas is sufficient to keep the LAr purity;
- filling speed has to be as high as possible in order to limit the LAr contamination from the large exposed surfaces;
- standard Oxysorb/Hydrosorb filters provide a purity level which is well above the experimental requirements.

The purification speed during detector filling (2 m<sup>3</sup>/h of LAr) is defined by extrapolating data from small size prototypes, and taking into account the outgassing rates of materials used for the T600 inner detector. The gas recirculation power (50 GAr m<sup>3</sup>/h/LAr container) was also defined by extrapolating data from the 3 ton prototype to the gas volume of the T600.

A fast recirculation system working in the liquid phase was added to the gas recirculation to restore the purity of the liquid in case of accidental contamination during the run. The LAr recirculation was dimensioned (recirculation speed of 2 m<sup>3</sup>/h) in order to restore the operating conditions in less than 1 month, starting from an electronegative impurity contamination of 10 ppb (O<sub>2</sub> equivalent).

Injection of argon (either gaseous or liquid) in the main volume from the external storage dewar is performed through two sets of Oxysorb/Hydrosorb filters (purifier units) placed in series. Each unit is made of four identical cartridges in parallel and filled for  $\frac{1}{3}$  with Hydrosorb<sup>3</sup> (molecular sieves 5A) and for  $\frac{2}{3}$  with Oxysorb. A circulation of LN<sub>2</sub> around the cartridges prevents the gasification of the argon, that would drastically reduce the mass-flow rate. The four filters sets are placed in evacuated stainless-steel containers for thermal isolation purposes.

Each set of filters is dimensioned (oxygen absorption capability) to allow for the purification of the LAr volume of a half-module starting from standard commercial LAr (concentration of H<sub>2</sub>O

and O<sub>2</sub> of about 0.5 ppm). The nominal purification speed is 2 LAr m<sup>3</sup>/h and is obtained by regulating the pressure inside the external storage tank. The presence of four cartridges in series adds a safety margin in case of unexpected contamination of the industrial LAr from the storage dewars and allows to start LAr recirculation (that uses the second set of cartridges) immediately after the filling, with no need to replace the filters. The scheme of the LAr recirculation system is shown in Fig. 10.

Both gas and liquid recirculation are needed to attain the desired free-electron lifetime. The two LAr containers are separately handled with respect to the Argon purification. Each container is instrumented with:

- (1) two gas recirculation units with nominal speed of 25 GAr m<sup>3</sup>/h/unit and
- (2) one liquid recirculation unit with nominal speed of 2.5 LAr m<sup>3</sup>/h.

The two gas recirculation units (Fig. 11) collect the gas from the chimneys that host the cables for the wire chamber read-out. The gas is re-condensed into a LN<sub>2</sub> re-condenser with the liquid dropping into an Oxysorb filter placed below the re-condenser. The purified argon is sent back into the LAr container just below the LAr surface. The gas recirculation units are designed to stay continuously active during the whole detector run-time. The importance of gas recirculation has been widely demonstrated by the operation of various prototypes, starting from the 3 ton detector [2,4,15].

The main purpose of the liquid recirculation is to purify the argon just after filling and until the required LAr purity is reached. In addition, it has to restore the purity in case of accidental pollution during the detector run, e.g. due to a sudden depressurization of the gas volume.

Liquid recirculation units consist of an immersed, cryogenic, liquid transfer pump placed inside an independent dewar located on the backward side of the LAr container. The dewar is fed in through a vacuum insulated transfer line connected to the backward wall of the container at about 2 m from the floor. The LAr in the pump cryostat is kept at same level of the container by

<sup>3</sup>Hydrosorb and Oxysorb are registered trademarks of Messers-Griesheim GmbH, Krefeld, Germany.

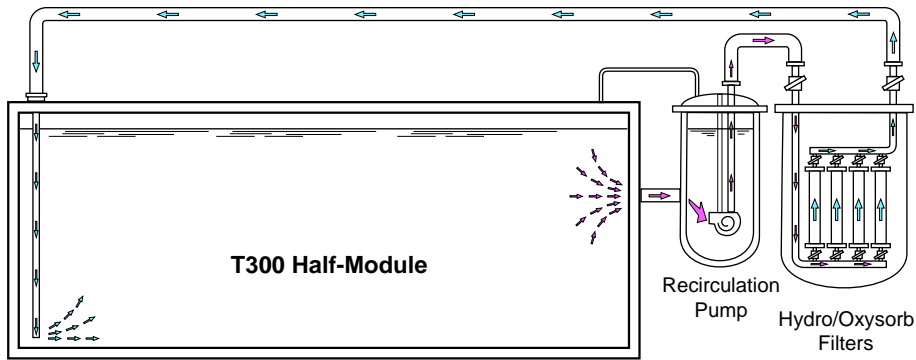


Fig. 10. T300 LAr recirculation scheme.

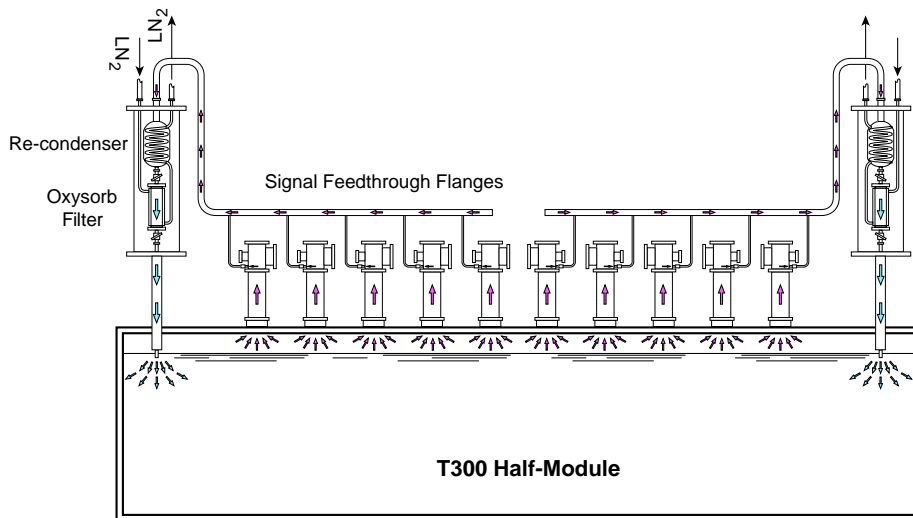


Fig. 11. GAR recirculation scheme of one half-module.

means of a connection between the two gas phases. The pump pushes the LAr into the second purifier used for the container filling, and the purified liquid is sent back to the front side of the LAr container, near the floor, about 20 m apart from the input of the pump, in order to maximize the recirculation efficiency.

The excellent performance of the liquid recirculation system was already demonstrated for the 10 m<sup>3</sup> prototype, for which a speed of about 0.5 m<sup>3</sup>/h was achieved [15]. During the test run it was also verified that the LAr recirculation system does not induce any microphonic noise to the wires, demonstrating that liquid recirculation can be accomplished while reading out the detector.

## 6. The LAr purity monitor system

A dedicated monitoring device, the so-called purity monitor, was first developed in 1989 by the ICARUS Collaboration [30]. Successively, several purity monitor units have been assembled and extensively used for operation of the various ICARUS prototypes.

The basic purity monitor design consists of a small, double-gridded drift chamber immersed in the LAr volume and located outside the imaging volume boundaries. Bunches of electrons can be extracted from the cathode via photoelectric effect. The electron bunch moves towards the anode along the electric field lines crossing a drift region

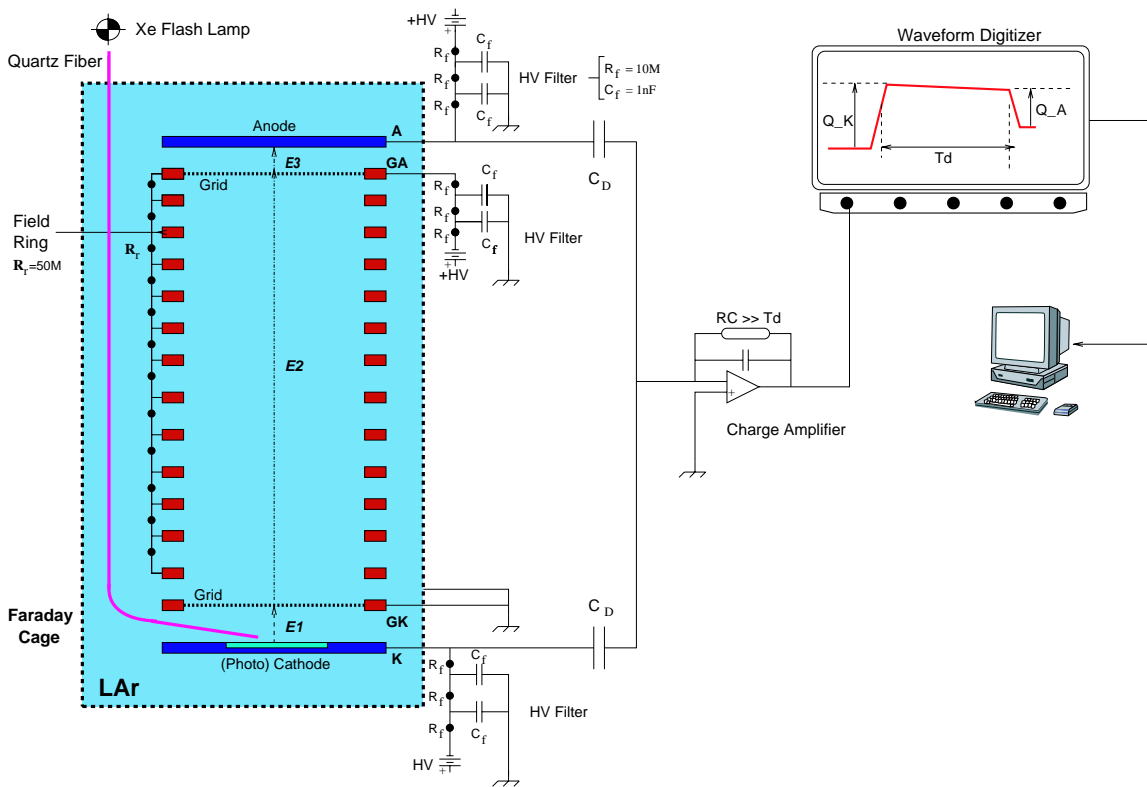


Fig. 12. Layout of the purity monitor and read-out scheme.

between two parallel, transparent grids. During the drift path, attachment to impurities may take place reducing the amount of electron charge collected by the anode, compared to the extracted charge. The ratio of these charges is a function of the electron lifetime in LAr that can therefore be estimated.

The lifetime is directly connected to the impurity concentration  $N(\text{O}_2)$ , i.e. the total concentration of impurities equivalent to Oxygen contaminant, by an inverse linear relationship. The lifetime estimate thus provides a direct measurement of the LAr impurity content.

In view of the realization of the purity monitor units to be installed in the T600 module the working principle has been retained while the original design has been revised. The major modifications concern the mechanics, the signal read-out system and the choice of the photo-cathode material and of the light source.

Each T300 detector hosts six custom-made purity monitor units located outside the LAr imaging volume at different heights. Once assembled and before installation each unit was individually cleaned and tested in vacuum, in argon gas and in LAr with a dedicated cryogenics facility. The test allowed to check the correct functionality of the monitor and to obtain a cross-reference list of the working parameters.

Each purity monitor unit is realized according to the scheme presented in Fig. 12. The main geometrical parameters and characteristics of the device are listed in Table 5. The purity monitor drift chamber consists of four parallel, coaxial electrodes: the photo-cathode disk K, a first grid GK at short distance from the cathode, a second grid GA facing the anode and the anode disk A at short distance from GA. A field-shaping system is formed by an array of 15 coaxial rings between GK and GA. All the elements are made of stainless-steel.

Table 5  
Geometrical characteristics of the purity monitor

Purity monitor mechanical structure	Stainless steel
K, A disk diameter	80 mm
K—A total drift distance	188 mm
K—GK gap	18 mm
GK—GA gap	160 mm
GA—A gap	10 mm
Number of field-shaping rings	15
Field-shaping ring diam./pitch	80 mm, 10 mm
Grids (GK, GA)	Nikel mesh
Grid diameter	60 mm
Grid inter-wire spacing	1.9 mm
Grid wire diameter	0.1 mm
Purity monitor optical fibre	
Type/material	Quartz (all silica)
Diameter	940 or 1550 $\mu\text{m}$
Inclination	20°
Attenuation	1 db/m at $\lambda = 95 \text{ nm}$
Photo-cathode	Material
(I half-module)	
Monitor Id.	
#1, #2	Metal (Gold deposit on brass)
#4	Semiconductor (CdZnTe)
#3, #5, #6	Semiconductor (GaAs)
(II half-module)	
Monitor Id.	
#1–#6	Semiconductor (GaAs)

The two grids are electro-formed Nikel meshes<sup>4</sup> with 1.9 mm wire spacing, 100  $\mu\text{m}$  wire diameter and 89.7% geometrical transparency. The flatness of the grid plane is guaranteed by a mesh holder made of two rings pinching the mesh in between. A mechanical structure formed by a system of vetronite-threaded rods, spacers and bolts, holds together the electrodes. Both materials, stainless-steel and vetronite, have similar thermal coefficient to guarantee negligible thermal stresses during cooling down operations. The mechanical stability of the device results to be completely satisfactory and matching the requirement of long operation in cryogenics environment.

HV potential can be applied independently from a multi-channel HV supply to the K, GA, A electrodes (GK is referred to ground) by electrical connections to the corresponding pins of a vacuum-tight feedthrough mounted onto one of the exit flanges of the cryostat. Three coaxial cables are used inside the cryostat, with the shieldings soldered together and connected to an independent pin of the feedthrough for the ground connection. The length of the cables (from 5 to 8 m) is determined by the position of the purity monitor inside the LAr vessel.

The two grids and the field-shaping rings are connected by a high-value resistor chain (50 M $\Omega$  each) in order to realize a resistive divider for the electric potential applied between the two grids. This scheme ensures the uniformity of the electric fields ( $E_1, E_2, E_3$ ) in the three drift regions (between K—GK, GK—GA and GA—A, respectively). Typical field values according to  $E_3 > 2E_2 > 2E_1$  proportions, range between few tens of V/cm in the first gap and some hundreds of V/cm in the other gaps. The grid geometry combined with the HV bias applied to the electrodes guarantees maximum transparency (i.e. the minimum number of drifting electrons lost crossing a grid) and maximum shielding, since the drift of the electrons before a grid does not affect the field after the grid.

Each purity monitor is contained in a stainless-steel, pierced Faraday cage to isolate the system from the outside electrostatic interference. After installation in the LAr vessel of the T600 the cage is mechanically and electrically connected to the stainless-steel frame of the wire chamber. In Fig. 13 two fully mounted purity monitor units of the first half-module are shown before (after) insertion in the electrostatic cage.

The photo-cathode is the most important component of the purity monitor. The precision on the lifetime determination depends on the actual signal-to-noise conditions provided by the system, the signal being the charge amplitude extracted from the cathode and subsequently collected by the anode. In the first half-module four purity monitor units are equipped with elemental semiconductor (GaAs and Cd(Zn)Te) photo-cathode and two with metal (Au)

<sup>4</sup>Produced by BMC Buckbee-Mears, St. Paul, MN, USA; Nikel mesh type: MN-73.



Fig. 13. Purity monitors after mounting in the first half-module: (left) purity monitor #3 in the final configuration (inside the Faraday cage), (right) purity monitor #2 before insertion in the Faraday cage.

photo-cathode. In the second half-module all six purity monitor units are equipped with GaAs photo-cathodes.

The quantum efficiency of the elemental semiconductors is normally higher than for metals (by about one order of magnitude). When compared with other semiconductor photo-cathodes, e.g. those formed by compounds of alkaline elements, the elemental semiconductors show indeed considerably lower quantum efficiency, due to their higher surface barrier ( $\geq 4$  eV). However, only the latter have stable chemical characteristics, necessary for a long-term operation in cryogenics, ultra-pure environment. Both semiconductor and metal photo-cathodes employed in the T600 purity monitor show large photo-emission under UV-light with wavelength below about 300 nm. This requires a suitable choice of the UV-light source and of the light transport means (from the source to the photo-cathode).

A quartz optical fibre of 0.94 or 1.55 mm core diameter,<sup>5</sup> all silica, allows to drive the light from the source (down to 180 nm of wavelength), outside the vessel, onto the photo-cathode. A fibre

holder realized in PEEK<sup>6</sup> and mounted onto the cathode disk keeps the fibre end in place at a distance of 2 mm to the cathode centre and at an angle of  $20^\circ$  with respect to the cathode plane.

A cryogenics indium sealed feedthrough allows the fibre to exit the LAr vessel without break up to the light source at the other end. The length of the fibre (from 4 to 7 m) is determined by the position of the purity monitor inside the LAr vessel. The UV-light source is a commercial available pulsed xenon flash lamp. The pulse width is of few  $\mu\text{s}$  with wavelength spectrum ranging from  $\lambda \sim 185$  to  $\sim 2000$  nm. The emission peak is centred around  $\lambda \sim 240$  nm ( $\sim 4.9$  eV).

When the purity monitor is immersed in LAr and a short UV-light pulse generated by the Xe lamp impinges on the photo-cathode, the photo-extracted electron bunch drifts towards the first grid inducing a current on the cathode during a time interval  $t_1$ . After crossing GK, the electron bunch drifts along the distance between the grids. During this time ( $t_2$ ) no current is induced on K or A due to the shielding effect of the grids. Later on, a current flows through the anode during the time  $t_3$  when the electrons move towards A after

<sup>5</sup>Produced by SPECTRAN Spec. Opt. Company, CT, USA; type: HGC-M0940T, core diam. 940  $\mu\text{m}$ , and by SENTRONIC GmbH, Dresden, Germany; type UV-T2, core diam. 1550  $\mu\text{m}$ .

<sup>6</sup>PEEK (PolyEtherEtherKetone) is an advanced plastic material with adequate mechanical properties at low temperature.

crossing GA. The extension of each time interval depends on the strength of the electric field in the corresponding gap. A charge amplifier allows to measure the charge  $Q_K$  and  $Q_A$  from integration of the anode and cathode signals in  $t_1$  and  $t_2$ , respectively. The current is approximately constant, assuming that the lamp pulse width is short compared to the time interval.

A dedicated system has been designed for the read-out and storage of the charge information from each purity monitor unit. It consists of (1) a decoupling stage formed by an HV filter and a pick-up capacitor ( $C_D$ ), (2) a single charge amplifier and (3) a waveform digitizer (Fig. 12). An aluminium, cylindrical case mounted directly onto the electrical feedthrough (outer side) hosts the Decoupling Stage as well as the charge Amplifier (AMPTEK-A250). On the top flange of the case there are the input HV and the output signal connectors. This set up minimizes ambient noise pick-up and the amplifier input capacitance due to the signal cable length.

Both anode and cathode signals feed the input stage of the amplifier (AC coupling) so to avoid the necessity of an inter-calibration of two signal amplitudes. The current signals from the anode and from the cathode are opposite in sign. Therefore, the charge amplifier output signal results in a trapezoidal waveform as a function of time, whose three main features (rising edge, flat top, falling edge) correspond to the three drifting gaps of the purity monitor.

Waveforms recorded with purity monitor #3 during the test run of the first half-module are shown in Fig. 14. The measurement of the rise and fall amplitudes, corresponding to  $Q_K$  and  $Q_A$ , along with the pulse duration (the drift time  $T_d$ ) gives a direct estimate of the lifetime ( $\tau_e$ ) at the time of the measurement [13].

## 7. Inner detector

Each of the two LAr containers, described in Section 4 and shown in Fig. 3, hosts a mechanical structure that sustains the different internal detector subsystems and the control instrumentation, namely, (1) the TPC wire planes and the

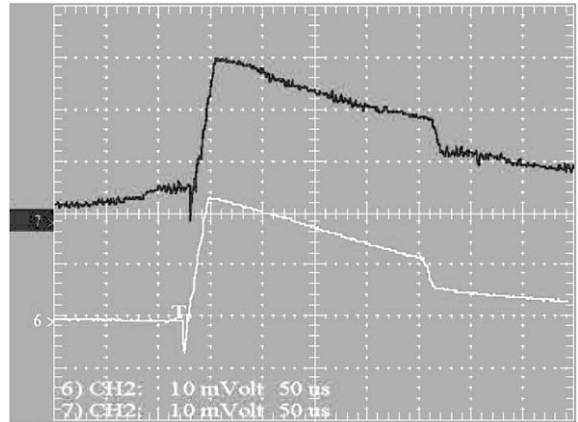


Fig. 14. Typical purity monitor waveforms: single Xe lamp shot (upper graph), averaged over several shots (lower graph).

relative HV electrode system (cathode and field-shaping electrodes) for the read out of the ionization charge, (2) the PMT system for the scintillation light detection, (3) sensors and probes of the slow control system and (4) the dedicated devices for the LAr purity monitoring. The complete design of the mechanics, including the TPC field-shaping system, has been developed in cooperation with BREME TECNICA, Italy.

Once the cryostat is filled, the structure is totally immersed in LAr. The stainless-steel chimneys, aligned in two rows on the aluminium ceiling of each T300 cryostat (20 per row) and terminated with special vacuum-tight feedthrough flanges, allow the passage of the signal cables for the various detector subsystems and control instrumentation.

### 7.1. Inner mechanical structure

All materials of the mechanical structure were chosen and treated to guarantee the LAr purity and the minimum radioactive contamination: the main components (beams and pillars) have been built with AISI 304L stainless-steel; other parts (supports, spacers, etc.) are made of PEEK. Stainless-steel surfaces, after machining, were subject to pickling and passivation. All components were finally washed in ultrasound bath with de-mineralized water, dried in a vacuum oven

(whenever allowed by their dimensions) and then packed in dry air atmosphere, ready for assembly.

The assembly of the mechanical structure for each half-module has been performed in a large, dedicated clean room at INFN Pavia. The stainless-steel structure has dimensions of 19.6 m in length, 3.6 m in width and 3.9 m in height, for a total weight of  $\sim 20$  ton, including the TPCs field-shaping electrodes. This structure has been progressively pushed inside the aluminium cryostat by means of a suitably designed lift, by sliding on rails that guarantee the correct alignment. A picture of the mechanical structure in its final position inside one T300 cryostat is shown in Fig. 15.

The integrated thermal shrinking between room temperature ( $\sim 300$  K) and LAr temperature ( $\sim 89$  K) is different for aluminium ( $\delta L/L = -3.8$  mm/m) and for stainless-steel ( $\delta L/L = -2.8$  mm/m). In order to cope with the different thermal shrinking, the stainless-steel structure leans on the cryostat aluminium floor by means of 10 adjustable feet basing on corresponding reinforced pads (Fig. 16 and also Section 4.1), and

rigidly linked to it only in two pads at half-module length; in this way, the structure is practically independent from deformations of the cryostat induced by cooling and by the different operating conditions (vacuum and overpressure); moreover, the sustaining structure is self-supporting and is rigid enough to allow for transportation.

Rocking frames to hold the TPC wires are positioned on the vertical long sides of the mechanical structure. The latter was dimensioned in such a way to sustain the total mechanical tension of the wires applied to the two wire frames.

The wire-frame design is based on an innovative concept: the variable geometry design (weight bridge). The beams of the wire frame are, in fact, movable. The upper and the lower horizontal beams are rigidly connected to each other on the back side of the frame by a set of calibrated springs, while the vertical beams are connected to the sustaining structure, also in this case by springs (Figs. 17 and 16).

The spring system is composed by three bucket-spring tie rods every 2 m along both the horizontal

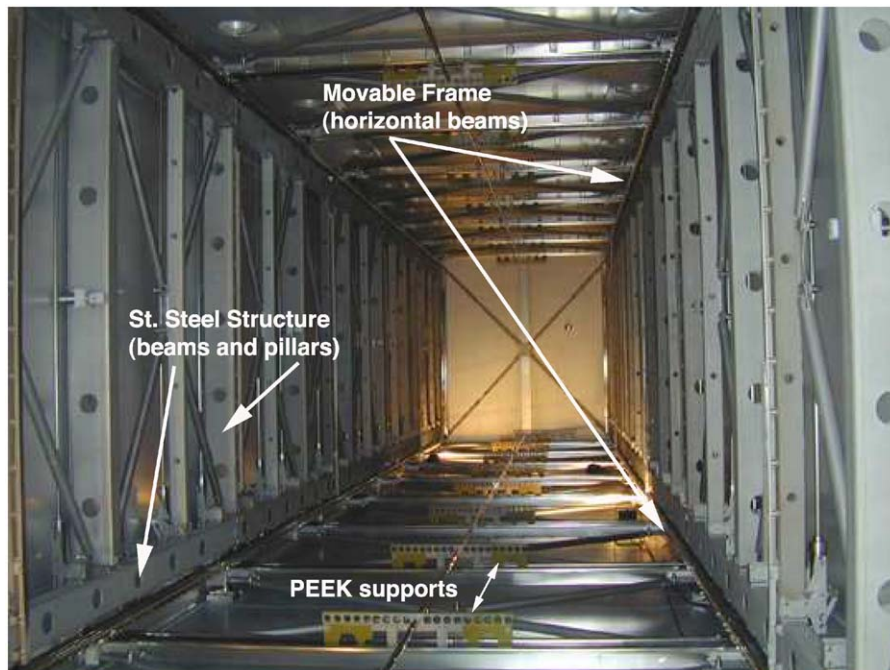


Fig. 15. The internal supporting structure.

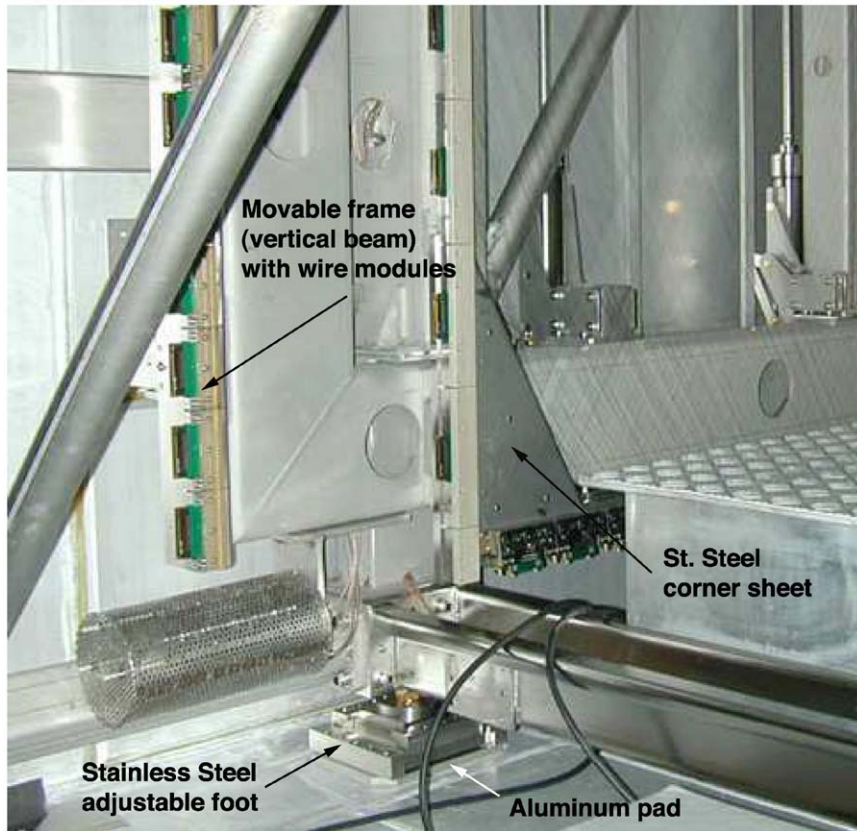


Fig. 16. Detail of the internal structure showing an adjustable foot.

and vertical beam lengths. This allows: (1) to set the tension of the wires anchored to the frame (Section 7.3) after easy installation, by appropriate loading of the springs (i.e. increasing the distance between the opposite beams of the frame), (2) to compensate for the tension increase on the wires due to possible overstress during the cooling and LAr filling phases (i.e. the wire mechanical tension is kept constant) and (3) to overcome the flexibility of the wide dimensions of the structure. Dedicated devices have been installed to measure the movement of the spring mechanism during the cooling phase (Section 9.3).

Due to the complexity of the mechanical design and aiming at the optimization of the wires installation and tensioning procedures, the construction and test of prototype mechanical structures of reduced dimensions have been considered

as a necessary milestone to proceed towards the realization of the T600 inner detector mechanics.

## 7.2. Test modules

A first test module of the sustaining structure and of its wire chamber (with dimensions of about  $6.0 \times 3.9 \times 1.5 \text{ m}^3$ ) was built in 1997 to check all mechanical aspects of the design. Later, another test module of further reduced dimensions ( $2.1 \times 3.9 \times 0.9 \text{ m}^3$ , for  $\sim 2$  ton of weight) was assembled. The structure of this test module housed a single TPC positioned at one side, made of two wire planes ( $2.0 \times 3.3 \text{ m}^2$  of common surface, 928 wires per plane) at  $\pm 60^\circ$  with respect to the horizontal direction. Wire production for the test modules was performed with a dedicated semi-automatic wiring table operated in the Pavia laboratory.

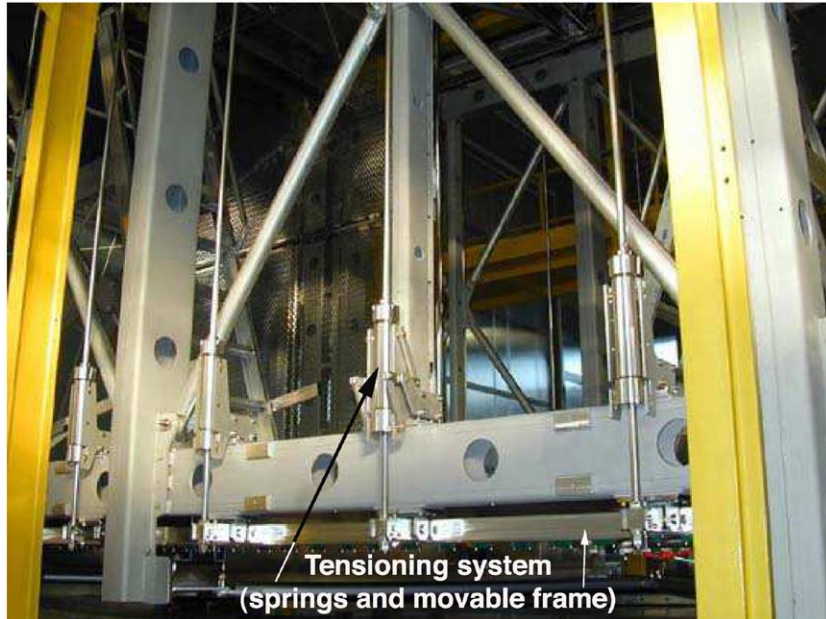


Fig. 17. Detail of the wire tensioning mechanics: a 2 m long portion of the wire frame equipped with three tensioning springs.

All main technical solutions envisaged for the T600 design have been adopted in the realization of both test modules. Wire installation on the wire frame and tensioning (by spring loading) procedures were followed and experienced successfully.

At the beginning of 1998, the smaller test module was placed inside the 10 m<sup>3</sup> LAr cryostat in order to study the cryogenic behaviour of the mechanics and, in particular, the reaction to thermal stresses during the cooling and LAr filling phases.

The results of the cryogenic test, consisting of a full thermal cycle from room temperature to LAr temperature (after cryostat filling) and back to room temperature (after cryostat emptying), were satisfactory and are reported in Ref. [15]. In summary, the main outcome can be summarized as follows:

- the mechanical structure resulted not to be deformed;
- none of the 1856 wires broke;
- none of the 1856 wires reached the wire elasticity limit;

- the individual wire tension measured after the thermal cycle resulted to be only slightly different (systematically higher by a few percent) compared to the value measured before the test.

After analysing the test module results minor design adjustments were made for the T600. In order to minimize frictions in correspondence of the moving parts of the elastic frames, possibly leading to the observed wire tension difference, the contact surfaces of various components were gold-plated and reduced whenever possible. Moreover, evacuation holes were added in order to speed up the outgassing.

### 7.3. Wiring

The wire production for the T600 TPCs was started well before the assembly of the mechanical structure. Wiring speed was increased compared to test phase by employing a second wiring table with improved automation capabilities. In particular, the wiring table is made of two lathes, controlled

by two stepping motors, which realize a pre-defined number (eight) of windings (slipknots), contemporary at both ends of the wire, around two ferrules inserted inside the lathes themselves. Two constant couple motors for the stretching of the wire, equipped with automatic control of the mechanical tension, are also mounted onto the wire table.

Wires are made of AISI 304V stainless-steel<sup>7</sup> with a wire diameter of  $150 \pm 5 \mu\text{m}$ . The length of the wires ranges from 9.42 to 0.49 m (Section 7.4) depending on the TPC plane type and on the actual position of the wire in the plane itself.

From the mechanical point of view one requires wires strung with a tension high enough to limit sagittas (due to gravity and to electrostatic forces) to values which are negligible with respect to the distance between the wires. The choice of a nominal tension force of 12 N (5 N for the longest wires) guarantees that (1) sagittas are limited to acceptable values in all cases and (2) wire elongation is still well below the elastic limit (39 N nominal value). Tension measurement is provided by one of the two different available methods, depending on the wire length: by means of a commercial wire stretch meter<sup>8</sup> or by using a custom-built device performing the analysis of forced harmonic oscillations induced on the wire.

The wiring procedure is organized according to a modular scheme, the basic unit being a 32-wire module. At first, each wire of the module is cut at a pre-defined length after stretching it at nominal tension; after that, the wire is tied at both ends with a secure slipknot to gold-plated stainless-steel ferrules. In this way a very safe holding is guaranteed by the wire friction itself. Then, a suitably designed PEEK shell holding 32 ferrules terminates the module at both ends. Finally, the 32-wire module is rolled up on suitable spools for subsequent cleaning and storage.

Both modules with wires of equal length and decreasing length were produced according to the design prescriptions (416 modules per TPC, 1664 modules in total). The wire production speed of

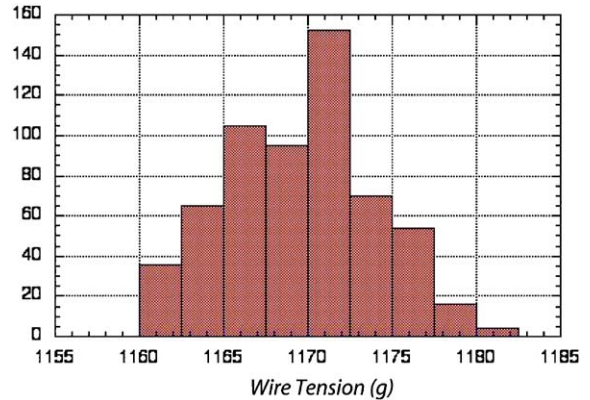


Fig. 18. Wire tension distribution for a sample of 576 wires. Individual wire tension is measured at the end of the assembly procedure of the 32-wire module. Entries to this distribution refer to the first wire of the 580-wire modules of equal length (3.77 m for the Collection and Induction-2 planes).

1 h for the assembly of a 32-wire module was found to be well within the early estimates based on the test module experience. After wiring, each 32-wire spool was washed in ultrasound bath, rinsed in de-mineralized water and dried in an oven under vacuum, and finally packed in dry air atmosphere.

The quality of the wiring procedure was found to be very satisfactory. As an example, the distribution of the wire tension measured after assembly of the module, for a sample of 576 wires (selecting one wire, the first one, per module of equal length) is reported in Fig. 18. An average value  $1169 \pm 4 \text{ g}$  (i.e. 11.5 N) was found. Dispersion around the mean value is acceptable, the systematic shift from the nominal tension value is within the mechanical error of the assembly procedure of the wire modules. The breaking tension (sampling few wires per day during wiring operation) was measured to have a mean value of  $2923 \pm 98 \text{ g}$ , hence assuring a sufficient safety margin, also considering the elasticity of the mechanical system.

Once the construction of the inner mechanical structure was completed and after positioning inside the cryostat, the 32-wire modules were individually unrolled from the spools and installed in the wire frames, as shown in Fig. 19. Wire

<sup>7</sup>Produced by MICROFIL, Lausanne, Switzerland.

<sup>8</sup>Wire stretch meter by CAEN, mod. SY 502.



Fig. 19. Sustaining structure and inner detector during the posing of wires.

holders allowed ease mounting of the wire modules onto the detensioned frames, as shown in the next section.

#### 7.4. Time projection chambers

Each TPC consists of a system of three vertical, parallel wire planes ( $17.95 \times 3.16 \text{ m}^2$  of common surface), 3 mm apart from each other. Two TPCs are installed in each T300, positioned on the opposite, vertical long sides of the sustaining structure. The distance between the two TPCs is 3.00 m, with the cathode plane (parallel to the wire planes) placed in the middle. This sets at 1.50 m the drift length of the active volume for both *left* and *right* chambers.<sup>9</sup>

<sup>9</sup>Due to thermal shrinking at LAr temperature, the actual maximum drift length (from cathode to the first plane) is reduced to 1482 mm.

Wire directions in the three planes run at  $0^\circ$  and  $\pm 60^\circ$  with respect to the horizontal direction. The first plane ( $0^\circ$ ) and the second plane ( $+60^\circ$  in both right and left chamber) facing the drift volume work in induction mode and are called Induction-1 plane and Induction-2 plane. The third plane ( $-60^\circ$  in both right and left chamber) works in charge collection mode (Collection plane). The wire pitch<sup>10</sup> is 3 mm for all planes.

The wires are stretched in the elastic frame sustained by the mechanical structure, as described above. Two coplanar, adjacent sets of horizontal wires (1056 units), all 9.42 m long, form the Induction-1 plane, stretched between the vertical beams of the wire frame and a central fixed beam; in both the Induction-2 and Collection planes (wires inclined at  $\pm 60^\circ$ ) the standard length of the wires stretched between the upper and lower beams of the frame is 3.77 m (4640 wires per plane), while wires of decreasing length (960 wires per plane) are used in the triangular-shaped portions, between one vertical and one horizontal beam, at the corners of the planes<sup>11</sup> (Fig. 16). The single wire capacitance in the various planes has been calculated to be 20 pF/m for the first (Induction-1) plane and the third (Collection) plane and 21 pF/m for the intermediate (Induction-2) plane.

In Table 6 the main characteristics of the wire chamber system are listed and in Fig. 20 a picture of the three wire planes for one of the assembled TPCs is shown.

The wires are anchored by special holders onto the wire frame in groups of 32 units (the wire modules). Each holder is formed either by one or two (according to the different cases) PEEK combs contained in stainless-steel supports which also embed one or two printed boards. The wire ferrules held by the PEEK shell terminating the wire module at each end are hung on the comb pins. A circuit printed on the board establishes the electric connection

<sup>10</sup>In each wire plane, the pitch is intended as orthogonal to the wires' direction.

<sup>11</sup>Since the shortest wire which can be made by the wiring device is 0.49 m long, the 64 wires in the extreme corners of the inclined planes have been replaced by triangular stainless-steel sheets in order to guarantee the required potential.

Table 6  
Main features of the TPCs inner detector

Number of read-out chambers (TPC) in T600	4
Number of wire planes per chamber	3
Distance between wire planes	3 mm
Wire orientation with respect to horizontal	0°, ±60°
Wire diameter	150 μm
Wire length	
Horizontal wires	9.42 m
Wires at ±60°	3.77 m
Wires at the corners (±60°)	3.81–0.49 m
Wire pitch (normal to the wire direction)	3 mm
Wire capacitance Ind.-1, Ind.-2, Coll.	20, 21, 20 pF/m
Wire nominal tension	12 N (5 N for hor. wires)
Number of wires/wire module	32
Number of wire modules/chamber	
Horizontal wires	66
Wires at ±60°	2 × 145
wires at the corners (±60°)	2 × 30
Number of wires/chamber	
Horizontal	2112
At ±60°	2 × 4640
At the corners (±60°)	2 × 960
Total	13 312
Total number of wires in T600	53 248
Wire plane voltage biasing (typical)	–220 V, 0 V, +280 V
Cathode HV (nominal)	75 kV
Cathode to Collection plane distance	1.50 m
Sensitive volume/chamber	85 m <sup>3</sup>
Length	17.95 m
Width	1.50 m
Height	3.16 m
Maximum drift length in LAr	1482 mm
Maximum drift time in LAr (at nominal field)	950 μs

between the 32 pins of the comb and a single connector also mounted onto the board. Fig. 21 shows the technical design of the mechanical system holding 2 × 32-wire modules for the wires at ±60°.

The wire modules are individually mounted onto the beams of the elastic frame (de-tensioned position). The elastic frame is schematically subdivided into portions (about 2 m long). Each portion comprises 18 × 2 combs/connectors. Once the installation of the TPC wire modules is completed, wire tension is restored by loading the springs of the movable wire frame (Fig. 20).

During detector operation, the read out of the ionization tracks from the various planes (*non-destructive* read-out) is accomplished by biasing the planes at suitable potentials. Assuming an electric field  $E_d$  in the LAr active volume (with nominal value  $E_d = 500$  V/cm from cathode to Induction-1 plane), a good “transparency” of the successive wire planes to the drifting electrons is obtained when  $E_2 \geq F \times E_1$ ,  $E_1 \geq F \times E_d$ .  $E_1$  and  $E_2$  are the field values in the Induction-1 to Induction-2 gap and in the Induction-2 to Collection gap, respectively.  $F = 1.2$ – $1.5$  is the range of the required field scaling factor. Typical biasing voltage for the TPC planes are reported in Table 6.

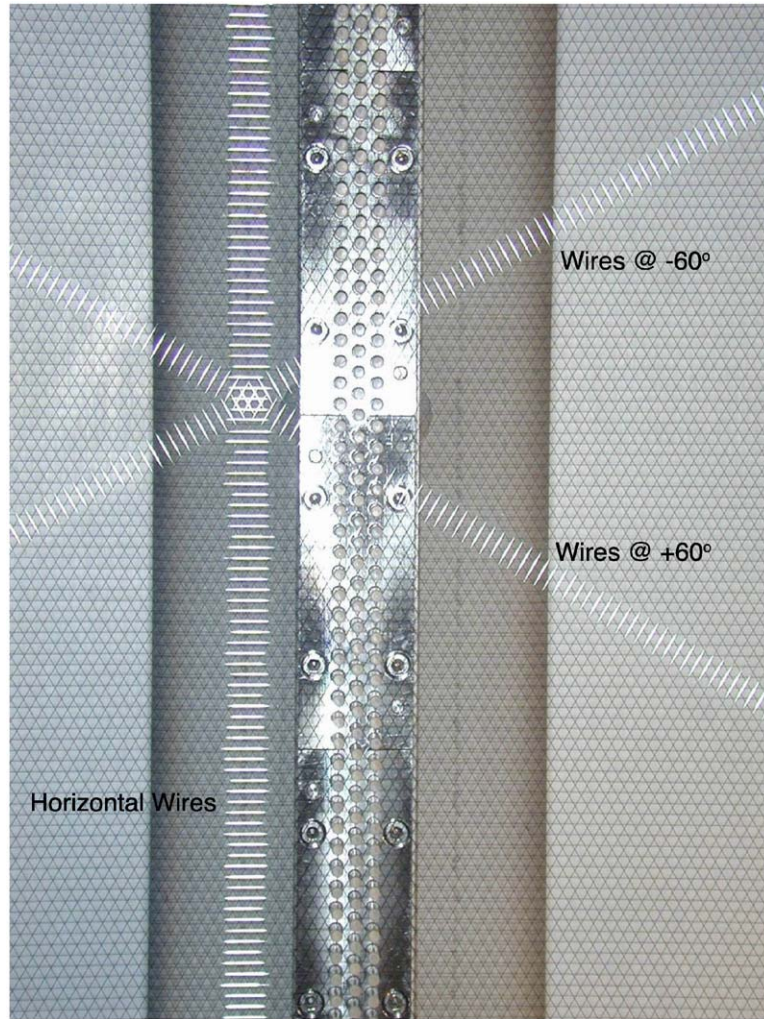


Fig. 20. The three wire planes of a TPC installed in the T600 detector.

### 7.5. Cabling

The individual wire signal transfer to the read-out electronics outside the cryostat is provided by twisted-pair flat cables<sup>12</sup> (34 pairs, flexible, halogen free). Thirty-two pair lines (pairs #1–32) of the 68 available contacts are dedicated to wire signals, one (pair #34) to the test-pulse signal and pair #33, referred to ground, is used as a screen between

signal and calibration conductors. Inside the cryostat (Fig. 22) the flat cables, suitably terminated with male connectors at both ends, are plugged at one end to the female connectors<sup>13</sup> (32-wire channels + 1 test pulse channel + 1 screen channel) mounted onto the printed boards of the wire modules. At the other end, the cables are plugged to similar connectors embedded (inner side) in specially designed vacuum-tight feedthrough flanges.

<sup>12</sup>Produced by 3M, Milan, Italy; Flat cable type KFTC-HP-30AWG-P270A.

<sup>13</sup>Produced by KEL, Tokyo, Japan; Connector type P25E-068S-TG.

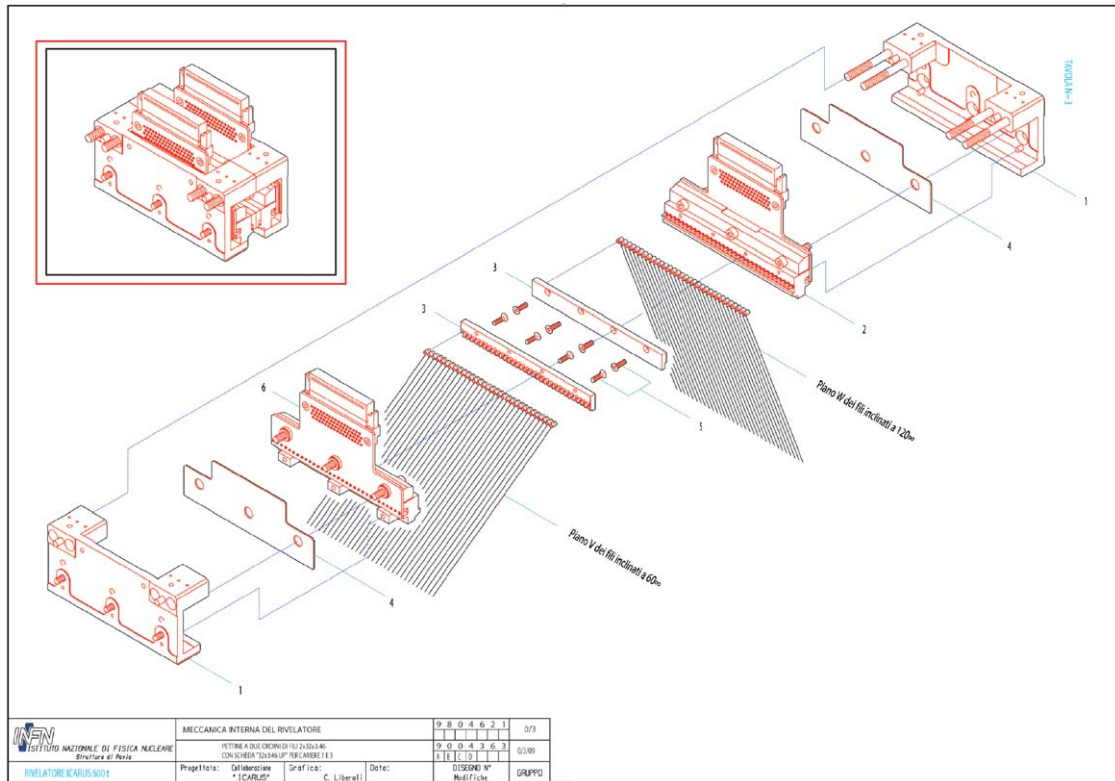


Fig. 21. Technical design of the mechanical system holding the 32-wire modules at  $\pm 60^\circ$ . Detail of the components (from left): mechanical support, spacer, printed board with connector, PEEK shell with 32-wire ferrules, PEEK comb (and reverse).

The flanges are mounted onto the top of the cryostat, at the end of the way-out chimneys (Section 4.1), close to the back side of the electronics racks. Each of the 96 feedthrough flanges installed in the T600 detector can provide the in-to-out signal transmission for 18-wire modules (576 wires)<sup>14</sup> and for eight coaxial cables for test pulse calibration. Short external flat cables for wire signals about 50 cm long, of the same type of those used inside, are employed to establish the final step connection between the feedthrough flanges (outer side) and the first stage of the electronic chain (decoupling board, as discussed in Section 11.2.1).

<sup>14</sup>The total number of wires is slightly smaller than the available number of transmission lines. In fact, inclined wires at the extreme corners of the wire planes are missing (or replaced by triangular stainless-steel sheets).

In order to achieve a proper signal shielding and transmission, the screen conductor in each twisted-pair line is connected to ground at the amplifier end, namely, the analog stage of the electronic chain. At the wire end, all screen conductors are connected together for all wire planes. This common connection is obtained through rectangular-shaped, low impedance, conducting rings, aligned along the sides of the wire frame.

The length of the internal flat cables varies depending on the actual position of the wire connectors on the wire-frame beams. The flat cable length is minimized in order to reduce the input capacitance at the entry point of the analog stage of the read-out electronics. The individual pair capacitance of the flat cables is 47.0 pF/m, according to specifications. For the Induction-1 plane ( $0^\circ$ ) the cable length ranges from 3510 to

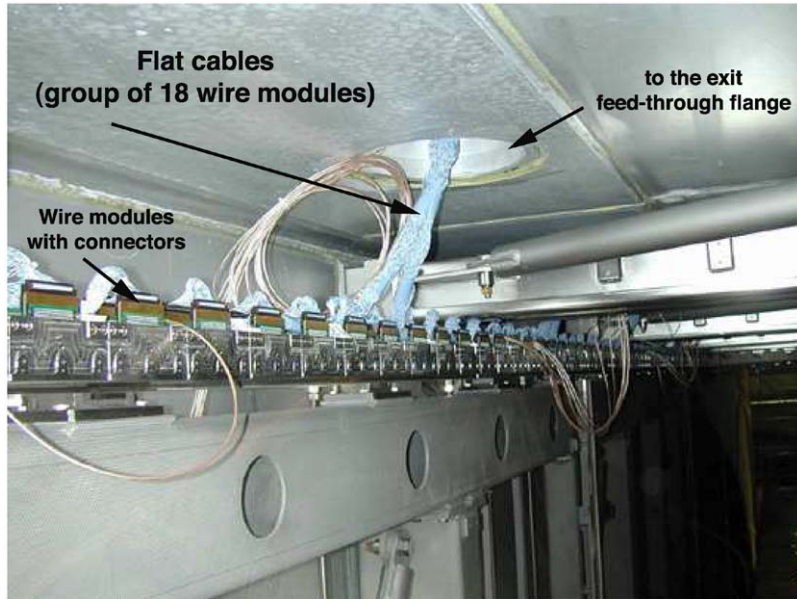


Fig. 22. Signal flat cables connection to the wire modules and extraction from the exit chimney (towards the feedthrough flange).

6210 mm, with an average length of 4860 mm and a mean capacitance of 229 pF. For both Induction-2 and Collection planes the cable length ranges between 1890 and 2430 mm (average length 2220 mm, average pair capacitance 104 pF). The length of the flat cables for the wires at the corners of the Induction-2 plane and the Collection plane is longer: the average length is 4237 mm, for an average capacitance of 199 pF. The complete connection layout from wires to the read-out electronics is schematically displayed in Fig. 23.

Cables were all individually inspected for electrical continuity after crimping of the connectors. Afterwards, they were washed and packed according to the standard cleaning procedure. Installation of the cables was made after the completion of the assembly of the wire chambers. All flat cables belonging to a 2 m long portion of each wire plane (18-wire modules corresponding to 576 channels) were grouped together and pre-assembled following the final assembly scheme (Fig. 22). Each group of flat cables serves one signal feedthrough flange, through which it brings wire signals to one rack of electronics.

### 7.6. Test pulse calibration

Four sets of test pulse signals are foreseen for calibration purposes (Section 11.2.1). The first one ( $V_1^{\text{cal}}$ ) is fed in via the coaxial cables of the feedthrough flanges (with screens connected to ground via the conducting ring on the wire frame). Test capacitors are mounted onto the printed board of the wire modules to provide test pulse signals injected to the wire far end. This allows for the absolute calibration of the entire chain from the wires to the electronics (up to the digital board stage) taking into account the different length of the signal cables; it also allows for checks of the correct connection of each wire and for the evaluation of the overall cross-talk between adjacent wires.

The second calibration set ( $V_2^{\text{cal}}$ ) is fed in via the dedicated twisted pair in each of the signal flat cables and the printed board capacitors to the closer wire ends. This is useful for the absolute calibration. The third calibration set ( $V_3^{\text{cal}}$ ) is fed in at the decoupling board stage, upstream of the decoupling HV capacitors.

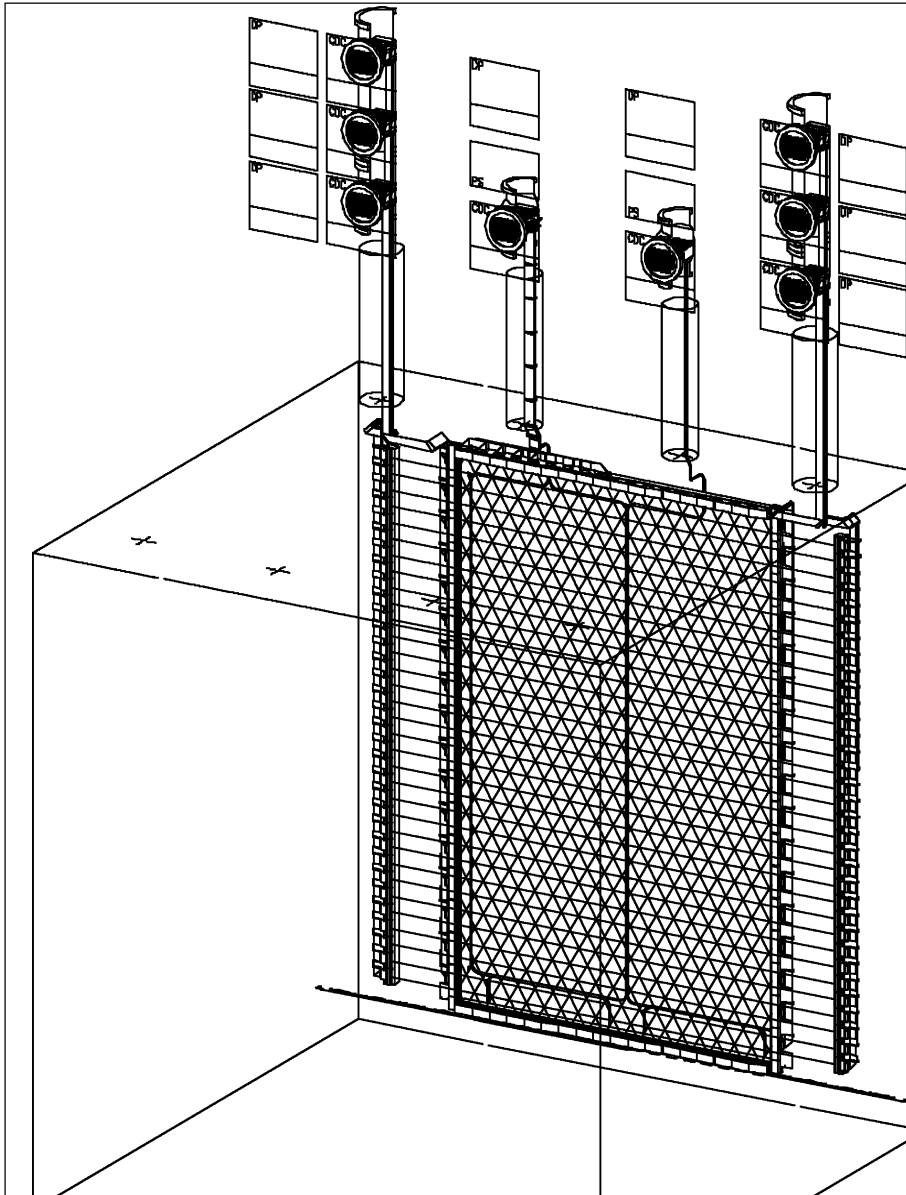


Fig. 23. Wires, cables, chimney and feedthrough layout. The back side of the electronic racks is indicated. Note that the wire chamber longitudinal dimension is not in scale, i.e. the figure includes only the non-repetitive portions of the TPC.

This set is used for gain calibration, measurement of the decoupling attenuation and cross-talk evaluation. The fourth calibration set ( $V_4^{\text{cal}}$ ) is fed in at the analog electronic board stage to the pre-amplifier inputs, and is

useful for card bench calibration and card layout cross-talk.

The use of the four test pulse calibration is redundant. Normally,  $V_1^{\text{cal}}$  or  $V_2^{\text{cal}}$  are used for periodic calibration during the detector operation.

## 8. The internal PMT system

Charged particles interacting in the LAr volume create ionized and excited Ar molecular states, which produce scintillation radiation through recombination and de-excitation processes. Extensive studies of scintillation light in LAr have been performed by several authors (see, for instance, Ref. [24] and references therein). In summary, scintillation in LAr is characterized by a prompt ( $<2 \mu\text{s}$ ) photon emission in the VUV spectrum with  $\lambda = 128 \text{ nm}$  and by a yield of the order of  $10^4/\text{MeV}$ , hence providing an absolute time measurement and a trigger for ionizing events occurring in LAr.

### 8.1. PMT type, cryogenics tests and selection

The experimental results from an R&D study [7,29] on different methods and devices able to detect the LAr scintillation light certified the use of a system based on PMTs directly immersed in the liquid.

The practical and economical solution adopted for the T600 detector consisted in adopting large surface 9357FLA Electron Tubes PMTs: 12-stage

dynode PMTs with hemispherical 200 mm (8 in.) diameter glass window, manufactured to work at cryogenics temperatures. Fig. 24 and Table 7 illustrate the main design features of the device.

A careful evaluation of the performance of each PMT before the final mounting in the T600 detector was carried out. The measurements were focused on the main PMT parameters which are temperature dependent in order to select the best PMT sample to be used in the T600. In particular, the following features were investigated for each PMT:

- (1) shape of the anode pulse;
- (2) single-electron response of the anode pulse;
- (3) gain;
- (4) single-electron transit time (spread, pre- and late-pulsing);
- (5) after-pulses;
- (6) dark-count rate and spectrum.

For this purpose a dedicated test facility was set up. The system made use of three cylindrical dewars (30 cm of internal diameter, 80 cm high) which were filled with  $\text{LN}_2$  during the measurement at cryogenic temperature. Each PMT to be tested, provided with its voltage divider, was

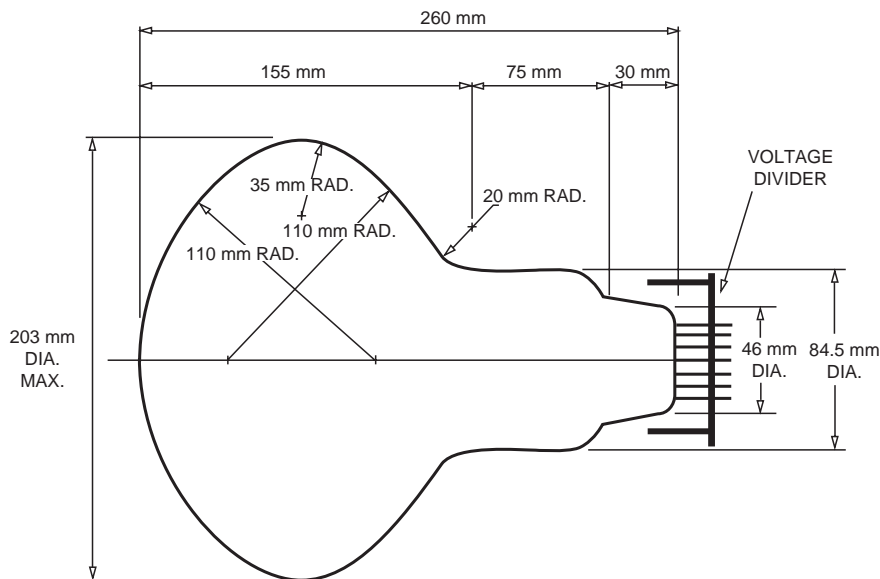


Fig. 24. The Electron Tubes Limited 9357FLA PMT outline drawing.

Table 7  
Nominal physical and electric characteristics of the 9357FLA  
Electron Tubes PMT

Length and diameter	293 mm; 203 mm
Cathode size	190 mm
Spectral response	300–500 nm
Dynodes	12LF CsSb
SER p/v	2
Dark counts	1500 CPS
Rise time and FWHM	5 ns; 8 ns
Maximum gain	$5 \times 10^7$
Quantum efficiency (blue)	$\sim 10\%$ (cold)
HV supply	1200 V

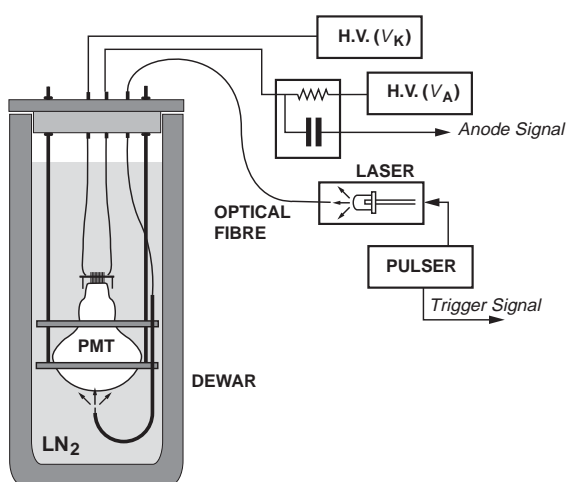


Fig. 25. Experimental set-up for the PMT testing.

mounted onto a sustaining structure together with an optical fibre and electric cables, as shown in Fig. 25. The PMTs were inserted in the dewars and left for 3 days at cryogenic temperature and in the dark prior to the measurements. The thermal insulation and the darkness conditions were preserved by means of proper caps, through which the electrical cables and the optical fibres were allowed to pass.

Two HV power supplies were used for the tests. The first one was used to provide the cathode with the proper focusing voltage ( $-600$  V); the second one fed in the dynode chain with a positive voltage to operate at the desired gain. The HV were brought to the base by means of two RG316

cables. The PMT signal was directly derived from the anode by means of a 10 nF decoupling capacitor. A 1 GHz oscilloscope was used to check the signal shape of the anode pulses (about 4 ns leading edge, 7 ns FWHM).

A laser diode emitting at a wavelength of 670 nm was used as light source. The diode was excited by a fast pulser (about  $3 \text{ V} \times 4 \text{ ns}$ , 50 kHz repetition rate). The light was brought to the photo-cathode by means of an optical fibre of 1 mm diameter and 2 m long. The main features of the lighting system were: fast output light pulse, high repetition rate and output triggering capability.

The response of the tubes to single photoelectrons (SER) were carried out by measuring the charge distribution of the PMT pulses to single-electron excitation. For this purpose the PMT output was integrated ( $40 \mu\text{s}$ ) and shaped ( $500 \mu\text{s}$ ). The output distributions were recorded by means of a multi-channel analyzer for different HV power supply values to the anode in order to obtain the PMT gain dependence as a function of the operating temperature.

Two typical curves obtained, respectively, at room and cryogenic temperature by using the same PMT sample are shown in Fig. 26. One can observe the exponential behaviour of the gain as a function of the voltage applied to the anode (dynode chain) and the appreciable reduction of the multiplier factor (to about 30%) at 77 K with

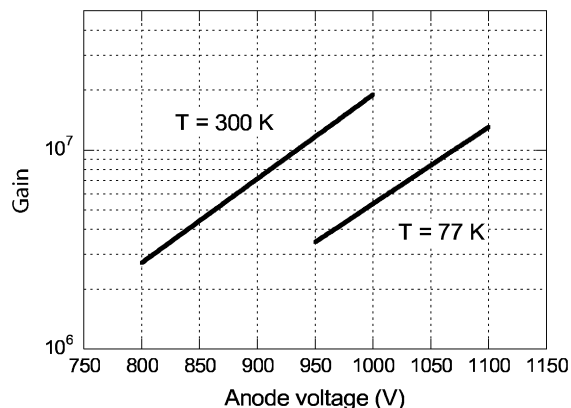


Fig. 26. PMT gain as a function of the anode voltage at room and cryogenics temperature, respectively.

respect to room temperature. However, the nominal PMT gain ( $10^7$ ) can be restored at cryogenic temperature by a suitable increase of the anode voltage.

For each PMT the dark count rate was measured by operating in complete darkness condition. The output pulses from the PMT were discriminated and counted during consecutive cycles in which the discrimination threshold was set at about 2 photoelectrons (pe). The measurement yielded a very low counting rate at room temperature ( $\approx 700$  Hz at 0.2 pe threshold) with an appreciable rise when operating in  $\text{LN}_2$  ( $\approx 1200$  Hz at 0.2 pe threshold).

The PMT transit-time spread was measured under the single-photon illumination conditions of the device and making use of a time-to-amplitude converter. The results show an intrinsically low transit-time spread of the tubes (about 1 ns) for both temperature conditions. This test was also used to reveal the presence of after-pulses, related to the internal vacuum level of the PMT.

About one hundred of 9357FLA photomultipliers were tested and 74 were selected on the basis of the following requirements:

- (1) narrow and fast anode pulse;
- (2) good single-electron response and resolution;
- (3) narrow and regular single photoelectron transit-time distribution;
- (4) low dark noise rate;
- (5) low after-pulsing rate.

### 8.2. Wavelength shifter

The PMT glass window is not transparent to the 128 nm scintillation light. However, the device can be made sensitive to the LAr VUV photons by coating the windows with a proper fluorescent wavelength shifter. Therefore, one needs a compound which is sensitive to the 128 nm radiation with an emission probability peaked in the blue region, where the transmittance of the glass window and the photo-cathode quantum efficiency are sufficiently high. Among the possible candidates reported in literature, the sodium salicylate (SS) and the tetraphenyl-butadiene (TPB) were selected and tested. By employing a solution with

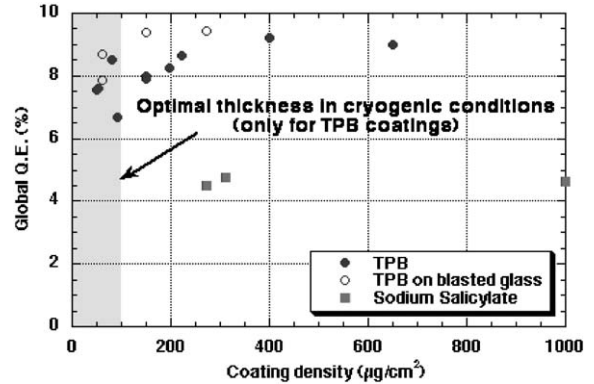


Fig. 27. Global quantum efficiency (PMT + wavelength shifter) as a function of different coating thickness and compounds.

the proper solvent (methyl alcohol or toluene) both compounds can be easily coated on glass surfaces by means of a nebulizer. This method provides a fine-grained and uniform layer of shifter on large surfaces.

Coatings of different thickness were tested to verify the adhesion after immersion in cryogenic liquid. The TPB samples showed mechanical instability for layer thickness larger than  $100 \mu\text{g}/\text{cm}^2$ . The tests carried out on sand-blasted glass showed better adhesion and performance.

The light response was measured as a global quantum efficiency of the system (PMT + wavelength shifter) by means of a monochromator and flat 30 mm PMTs, with the same characteristics of the selected ones (Fig. 27). The TPB compound was preferred because of its higher conversion efficiency; the global quantum efficiency with the optimized thickness is about 8%.

A final test on the TBP compound, carried out by means of a purity monitor, showed no affection of the LAr electron lifetime.

### 8.3. PMT mounting

The PMTs were mounted onto the wire-chamber frames by means of PEEK slabs with dimensions of  $350 \times 250 \text{ mm}^2$  and stainless-steel bars 3 m long (Fig. 20). The holding system allowed the PMT positioning behind the collection planes 5 mm far from the wires. In the first half-module

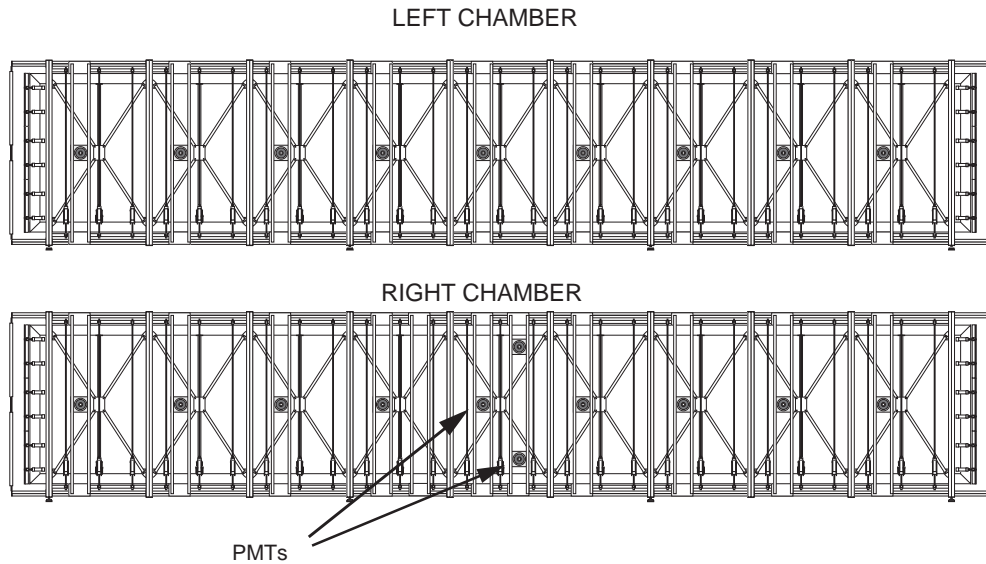


Fig. 28. PMT mounting in the first half-module structure.

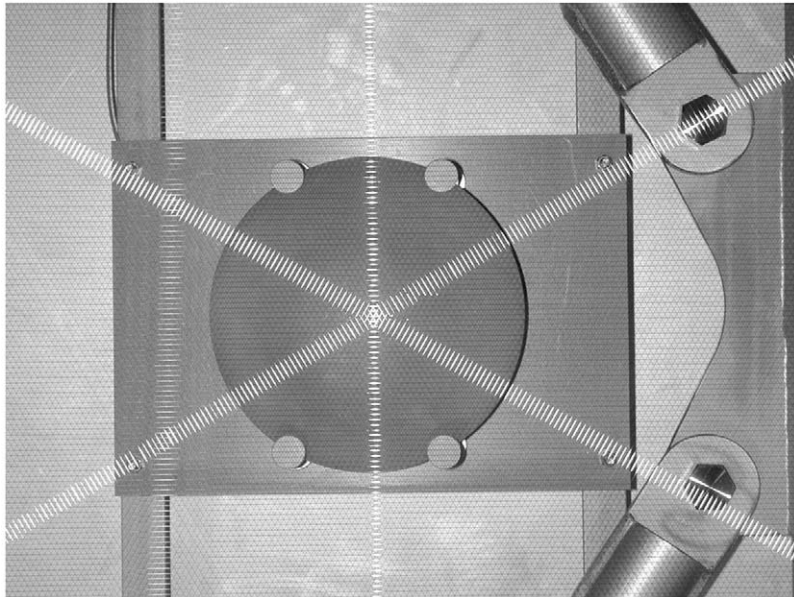


Fig. 29. Picture of the three wire planes. One of the PMTs is visible behind the wires.

a minimal set of 20 PMTs was installed (Fig. 28) behind the wires (Fig. 29).

The PMT location was defined by means of simulations taking into account the PMT dimen-

sions, position and detection efficiency to VUV photons, the light transmission of the window (at 128 nm) and the necessity to detect low-energy events (with an energy threshold down to 5 MeV)

with the highest efficiency. In the second T300 a more complete coverage of the detector inner surface was adopted, employing 54 PMTs.

#### 8.4. Electronic set-up

For each PMT a voltage divider designed to operate at low temperature was welded directly to the PMT output leads. The PMT bases were connected to dedicated HV feedthrough flanged on the detector signal chimneys by means of 8 m long RG316 cables. HV distributors were used to provide each PMT with the proper power supply and to pick up the anode signals.

An electronic system based on discriminator and coincidence units was used to provide a PMT pulse for the detector trigger logic. During the test run, the output signal of some PMTs was acquired by means of the same electronics used for the wire read-out. This allowed determination of the actual event position along the drift coordinate by studying the correlation between the ionization signals and the PMT pulses.

The PMT read-out system was structured as a multi-channel recorder that stores the anode current information during the drift of the free electrons. Each channel is equipped with an amplifier that integrates over 10  $\mu$ s followed by a 10-bit ADC, sampling the signal every 50 ns. To this purpose a custom analog board CAEN V791PM was designed and employed.

### 9. Auxiliary instrumentation and slow control system

During the different phases of leak testing with overpressure, evacuating, cooling and filling with LAr (Section 14), the cryostat and the inner detector are exposed to severe pressure and temperature conditions. In order to monitor the behaviour of the first T300 under such conditions, several slow control sensors with the corresponding read-out electronics were developed and installed on the detector. The system is also used to control such parameters of the detector as LAr level and temperature during the data taking phase. During the Pavia test the cryogenics basic

features, i.e. vacuum tightness, cooling process, temperature gradients, etc., were tested for the first time in such a large-size LAr vessel [31].

The slow control system consists of five different types of sensors:

- 16 LAr level meters;
- eight wall position meters to measure the inward/outward movements of the cryostat walls during the pumping and filling operations;
- seven wire position meters to measure the movement of the springs, which are attached to the wires of the chambers to compensate the thermal contraction during the cooling phase;
- 30 platinum resistors (PT1000) for the temperature measurement inside the cryostat and 15 resistors mounted onto the outer walls;
- 1 vacuum/pressure gauge.

The level and position measurements are based on a capacitance measurement, while the temperature is determined through the measurement of the resistance of the PT1000 resistors.

Fig. 30 shows a schematic top view of the cryostat with the position of the slow control sensors.  $FL_i$  and  $FR_i$  ( $i = 1, 2, 3, 4$ ) are the LAr level meters at the front-left and front-right corners, respectively;  $BL_i$  and  $BR_i$  are the level meters mounted at the two back-side corners.  $H_i$  ( $i = 1-6$ ) are the position meters for the horizontal wires.  $W_i$  ( $i = 1-8$ ) are the wall position meters mounted at the two side walls. IFL, IFR, ICL, ICR, IBL and IBR are the six groups of five PT1000 sensors mounted onto the detector frame in the cryostat; EFL, ECL and EBL are groups of five PT1000 installed at the left external wall of the cryostat (though inside the thermal insulation). Each group of PT1000 sensors measures the LAr temperature at five equally spaced heights.

#### 9.1. The LAr level meters

The level meters are cylindrical capacitors, shielded by a stainless-steel tube, grounded to the detector frame. Two different types of level meters are installed: 12 commercial level meters<sup>15</sup> with a

<sup>15</sup>Cryo Anlagenbau GmbH, Wilnsdorf, Germany.

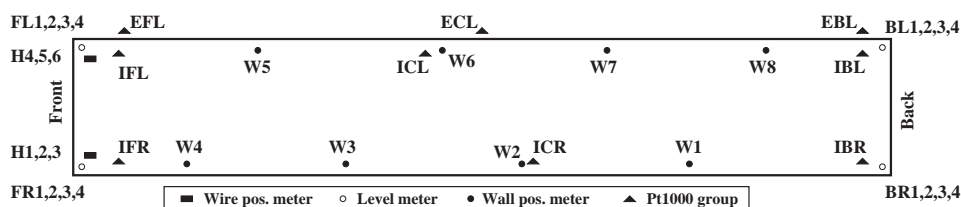


Fig. 30. Schematic view of the cryostat seen from the top. Indicated are the approximate locations of the different slow control sensors (see the text for a description of the sensors' labelling).

length of 1.3 m each used to measure the LAr level during the filling phase with a precision of about 15 mm, and four custom-made precision level meters with a length of 0.5 m. The absolute precision obtained with a single level meter is about 1.5 mm.

Four level meters are mounted onto the top of each other at the four corners of the cryostat, overlapping for about 20 cm and covering a total height of 3.8 m. Three commercial level meters cover a height up to 3.5 m, while the precision level meter is mounted onto the top. The precision level meters are built from two concentric stainless-steel tubes (length: 500 mm, outer diameter of inner cylinder: 25 mm, inner diameter of outer cylinder: 26 mm) held together by glass fibre, enforced epoxy end caps. The capacitance of the sensor in vacuum is 710 pF and the sensitivity to LAr is 0.7 pF/mm (the relative dielectric constant of LAr is 1.495 at 88 K). The capacitance of the sensor varies linearly with the fraction immersed in LAr.

### 9.2. The wall position meters

Eight wall position meters are mounted at half-height on the detector frame along the two side walls of the cryostat (Fig. 30). They measure the inward deformation of the side walls when the cryostat is pumped and the outward deformation when the cryostat is tested for leaks with argon gas pressure up to 1.3 bar (absolute) and when the cryostat is filled with LAr (Section 4.1).

Also the wall position meters are cylindrical capacitors made of stainless-steel and end-cap bearings made out of glass fibre enforced epoxy. The inner and outer parts are movable relative to



Fig. 31. Wall position meter mounted onto the detector frame. The inner cylinder of the sensor is pushing against the cryostat wall and moves with the wall.

each other along the axial direction. The capacitance changes linearly with the relative displacement over a range of 65 mm.

A wall position meter is shown in Fig. 31. The sensor is fixed to the detector frame with a polyethylene clamp and a spring pushes the inner cylinder against the wall, sensing its movement. The sensor has a length of 314 mm (in the OUT position) and the gap between the cylinders is 0.5 mm. The capacitance varies between about 130 pF (IN) and 30 pF (OUT) and the sensitivity is 1.6 pF/mm; the precision of the displacement measurement is about 0.2 mm.

### 9.3. The wire position meters

The movable frame of the wire chambers is attached to a spring system in order to maintain

approximately constant the mechanical tension of the wires (as described in Section 7.1). In case of a sudden cooling, the wires would cool down faster than the heavy chamber frame, due to their small heat capacity, i.e. they contract faster than the frame leading to an increased wire tension. The springs partially compensate this increase of tension.

Seven wire position meters have been installed in each T300 module to measure the movement of the spring mechanism during the cooling phase. The horizontal wires of the Induction-1 plane are split in two coplanar, adjacent sets (1056 wires, 9.42 m long), stretched between the vertical beams of the wire frame and a central fixed beam. For both left and right chamber, three wire position meters are connected to the springs of the vertical beam at the front side of the cryostat. No sensors are installed at the back side. Another wire position sensor is connected to one of the springs along the horizontal beam of the wire frame holding the wires of the two planes with  $\pm 60^\circ$  wire orientation of the left chamber.

The wire position meters are cylindrical capacitors similar to the wall position meters. However, in order to increase the measurement sensitivity, they consist of 10 parallel cylindrical capacitors. A decomposed wire position meter is shown in Fig. 32. The inner surface of the outer cylinder has



Fig. 32. Decomposed wire position meter. The inner surface of the outer cylinder also has the same periodic structure as the one of the inner cylinder.

the same periodic structure as the one of the inner cylinder. The total length of the sensor (in the IN position) is 392 mm and the linear measuring range is 15 mm; the gap between inner and outer cylinder is 0.5 mm. The capacitance in the middle position is about 150 pF and the sensitivity of the sensors is 8.4 pF/mm. This results in a measurement of the spring movement with a precision of 0.1 mm.

#### 9.4. The temperature monitors

A total of 30 PT1000 platinum resistors<sup>16</sup> was installed on the detector frame inside the cryostat to measure the temperature distribution over the whole detector volume during the cooling and the data-acquisition phases. These sensors are bunched in groups of five. The five sensors of a group are distributed over the height of the detector at the same horizontal location (Fig. 30). Three groups of five PT1000 resistors are mounted onto the left external wall of the cryostat (inside the thermal insulation).

The resistors were cycled 10 times between room temperature and LN<sub>2</sub> temperature before mounting them on the detector. After the temperature cycling all the used sensors were calibrated in LN<sub>2</sub> at pressures between 1 and 2.5 bar covering the temperature range between about 77 and 88 K; the LAr temperature at 1 atm is 87.3 K and at the operating pressure of about 1.20 bar the LAr temperature is 88.9 K (Table 3).

At a given LN<sub>2</sub> temperature the measured PT1000 resistors showed an RMS variation of the resistance of  $\sigma_R = 0.45 \Omega$ . By using the same calibration curve for all the resistors, one obtains an RMS variation of the temperature readings (for a given temperature) of  $\sigma_T = 0.12 \text{ K}$  for the used PT1000 resistors.

## 10. HV system

The HV system has to produce a stable and uniform field over the 1.5 m maximum drift length

<sup>16</sup>Produced by Cyntec Co., Ltd., Shin-Chu, Taiwan; SA 10200524.

Table 8  
Main characteristics of the HV system

Number of cathode panels	9
Dimensions of a cathode panel	$2.0 \times 3.2 \text{ m}^2$
Cathode panel thickness	1.5 mm
Cathode panel pierced surface	58%
Race tracks dimensions	$18.1 \times 3.2 \text{ m}^2$
Number of elements race track	20
Race track diameter	34 mm
Race track thickness	0.8 mm
Race track pitch	49.6 mm

in the drift volume. The system is made of several components. These are described in detail in the following sections; their main features are summarized in Table 8.

### 10.1. Cathodes, electric field electrodes and HV degrader

The cathode is built up by an array of nine panels (Fig. 33) made of punched stainless-steel sheets. This solution is mechanically adequate to reduce the weight and allows a 58% optical transparency between the two drift regions. This allows the detection of the scintillation light by means of PMTs operating in LAr, positioned between the wire chambers and the cryostat walls. The cathode panels are held by PEEK supports linked to the inner mechanical structure. The drift electric field is generated by biasing the central cathode at a negative HV referred to the potential of the first wire plane.

The electric field in each drift volume is kept uniform by means of the race track electrodes (Fig. 34). These consist of 29  $18.1 \times 3.2 \text{ m}^2$  rectangular rings for each wire chamber, made of 2 m long stainless-steel tubular elements (34 mm diameter, 0.8 mm thick) connected by two welded terminals.<sup>17</sup> The distance between race tracks is 49.6 mm. In the upper part, between the race tracks and the GAR phase, a grounded metallic shielding is interposed. The race tracks are set at a potential linearly decreasing from the cathode

<sup>17</sup>The HV system mechanics was manufactured by Galli & Morelli Industry, Acquacalda, Italy.

potential to the first wire plane potential, to ensure uniform electric field and hence constant drift velocity inside the volumes.

The biasing potentials of the race tracks are obtained through resistive voltage degraders. The current flowing in each degrader ranges from 100 to 200  $\mu\text{A}$  for HVs ranging from  $-75$  to  $-150 \text{ kV}$ . The HV degrader is based on four resistor chains, one for each drift volume, with the “hot” end connected to the cathode and the “cold” end set to ground. Resistor chains are made of 30 steps. Intermediate contacts are connected to the field-shaping electrodes (Fig. 34).

The resistance value for each step is  $25 \text{ M}\Omega$  obtained by connecting four  $100 \text{ M}\Omega$  resistors in parallel. For a  $0.5 \text{ kV/cm}$  drift field the voltage across each resistor is  $2.5 \text{ kV}$ . The resistor type is METALLUX-969.11.<sup>18</sup> Each of the 240 resistors for the 1st half-module was successfully tested before installation under a HV of  $5 \text{ kV}$  at room temperature in air, at  $77 \text{ K}$  in  $\text{LN}_2$  and then again in air at  $300 \text{ K}$  (Fig. 35). During the installation a final test was performed on the HV system just before closing the cold body. The correct positioning of the HV electrodes was also verified.

The monitoring voltages for the left and the right drift volumes, measured through a special voltage divider in the last degrader step (Fig. 36) gives a proportionality of  $10^{-4}$  with the HV applied to the cathode, as calculated. All the 240 resistors of the HV divider were operated in their final working position, in air at  $5 \text{ kV}$  (twice the nominal running voltage) measuring the absorbed current. The deviation from uniformity along the divider chain resulted to be less than  $5 \times 10^{-3}$  in both left and right chains.

### 10.2. Drift field uniformity

The uniformity of the electric field inside the drift volumes has been checked by calculating the voltage contours near the field electrodes under normal conditions and in case of breakdown of one (Fig. 37), two or three of the four resistors in parallel in the same degrader step. After the test described in Section 10.1, during which more than

<sup>18</sup>Produced by METALLUX SA, Mendrisio, Switzerland.

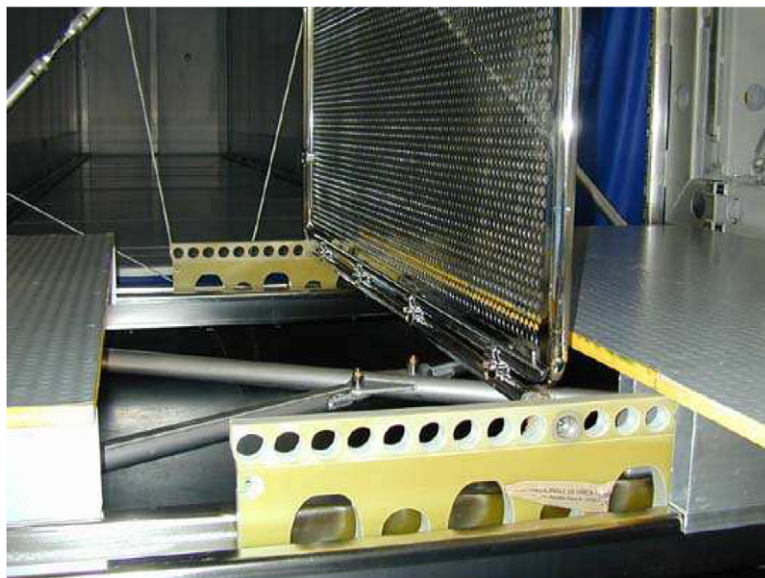


Fig. 33. Detail of one cathode panel.

300 resistors were tested, one can safely state that the possibility of one broken resistor has to be considered only hypothetical and the probability to have two (three) broken resistors in the same degrader step is, as an upper limit, of the order of  $10^{-5}$  ( $10^{-7}$ ). Nevertheless, calculations indicate that the detector can still satisfactorily operate under those unlikely conditions.

### 10.3. HV feedthrough

The HV generated by an external power supply is brought to the inner cathode via a novel-design hermetic feedthrough. A coaxial geometry has been adopted: the design is based on an inner conductor (HV) and an outer conductor (ground) insulated by UHMW PE (ultra-high-molecular-weight polyethylene) as shown in Figs. 38 and 39.

The outer conductor, made of a stainless-steel tube, surrounds the insulator extending inside the cryostat up to the LAr level. By such a geometry the electric field is always confined in regions occupied by high dielectric strength media (UHMW PE and LAr).

The inner conductor is made of a thin wall stainless-steel tube, in order to minimize the

heat input and to avoid the creation of argon gas bubbles around the HV lower end. A female contact, welded at the upper end for the connection to the HV cable and a round-shaped elastic contact for the connection to the cathode, screwed at the lower end, completes the inner electrode. Special care has been taken in the assembling to ensure the complete filling with the PE dielectric of the space between the inner and the outer conductors and to guarantee leak tightness at ultra-high-vacuum level.

In order to test its performance, the HV feedthrough has been inserted in a test cryostat filled with LAr with its cold end floating in the liquid. HV was applied and raised without discharges with a ramp-up rate of about  $-1$  kV/min, up to the maximum value of the power supply ( $-150$  kV, i.e. twice the nominal voltage of the T600 detector) with the power supply current meter constantly indicating a value compatible with the absence of current flow in the range  $0$ – $150$  kV. During these long-term tests, occasional micro-discharges were observed by looking at the output of a custom-built “corona detector” (Fig. 40).

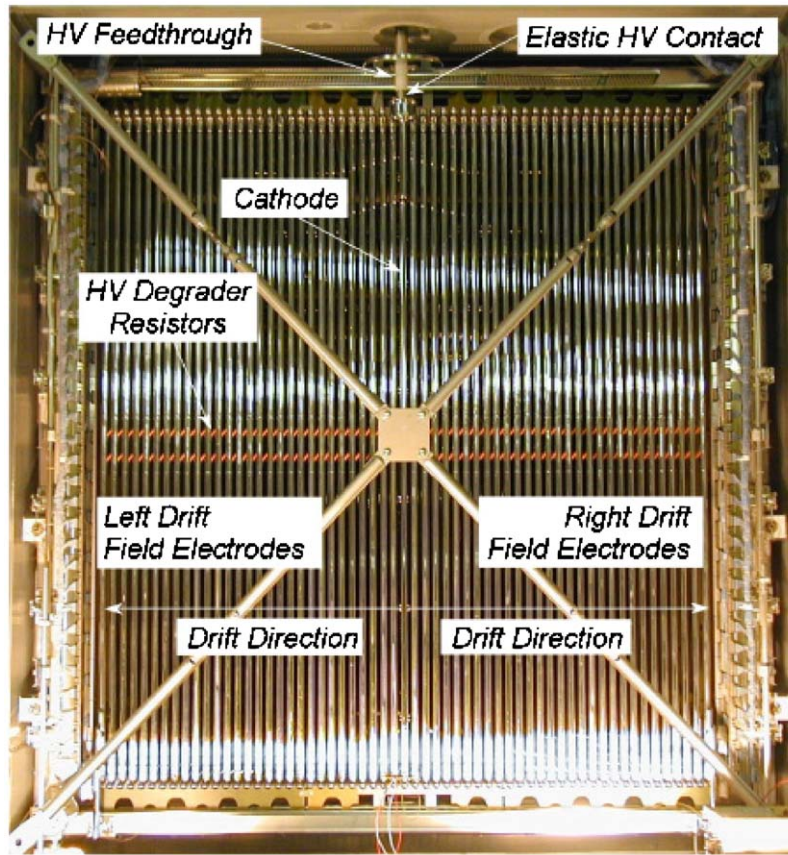


Fig. 34. The first half-module of the T600 detector before closing. Some components of the HV system are visible: feedthrough, cathode, field electrodes (race tracks), voltage divider.

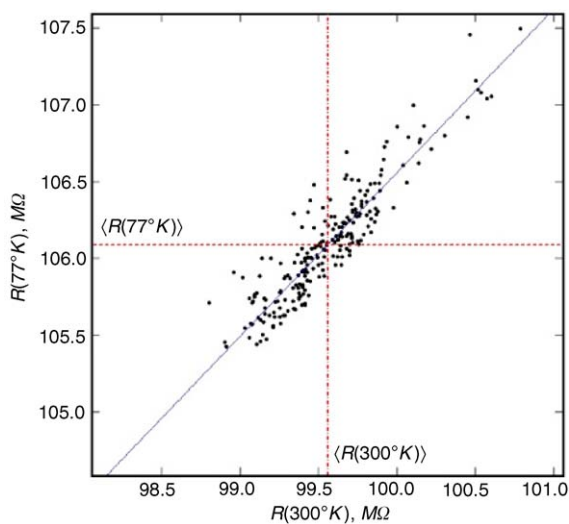


Fig. 35. Correlation between resistor values at 300 and 77 K.

Corona discharges are rather common in the power supply cable systems and are explained as due to the presence of moisture in the interstices at the cable-to-plug and at the plug-to-socket connections and mainly due to penetration through the conductive plastic tube surrounding the HV cable conductors. By filling these interstices by dry nitrogen gas through an inlet valve dedicated to this purpose, the micro-discharges immediately disappear.

Special care has been devoted to the design of the HV plug of the two T300 feedthroughs. Such a plug fits inside the feedthrough to make the cable hermetic to the air humidity and improve its tightness for Nitrogen pressurization, which significantly improve the prevention of discharges. Nitrogen vapours are largely available from the T600 cooling system exhaust and they have been used to pressurize the HV cable.

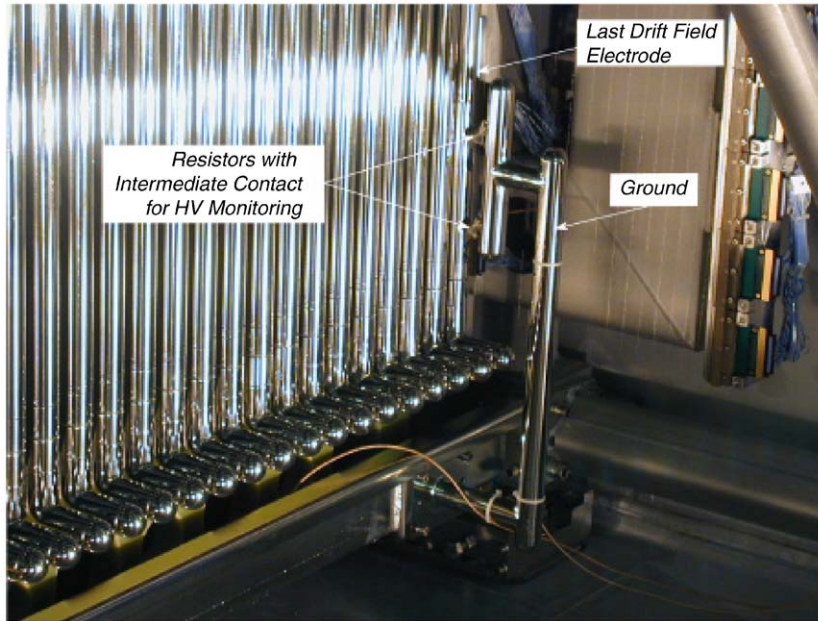


Fig. 36. The monitoring resistors on the right side of the voltage degrader.

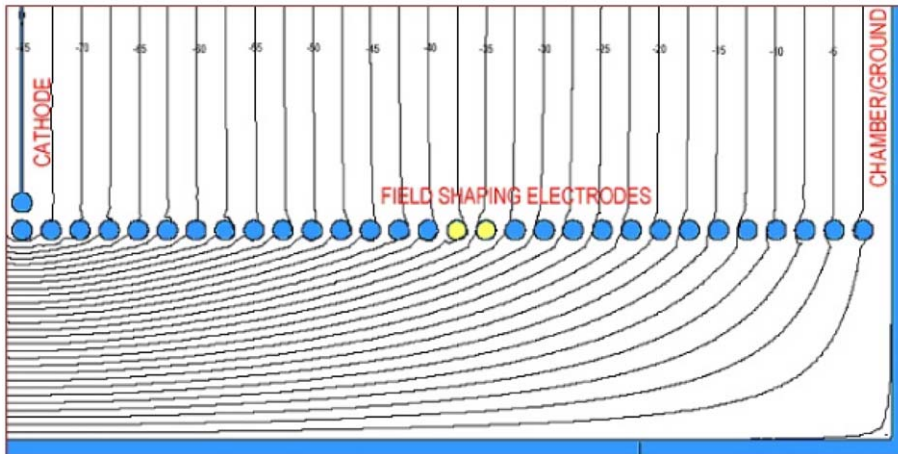


Fig. 37. Voltage contours, in 2.5 kV steps, in the lower-right region of the transverse cross-section of one half-module. The effect of breakdown is shown in one of the four resistors in parallel in the 15th step ( $R_{15} = 33.3 \text{ M}\Omega$ ) with all other degrader resistors equal to  $25 \text{ M}\Omega$ .

#### 10.4. HV power supply and residual ripple filtering

Operating the T600 detector at a drift field of  $0.5 \text{ kV/cm}$  requires an HV of  $-75 \text{ kV}$  applied to the cathodes and, with the four resistive voltage

degraders described in Section 10.1, a total current of  $0.4 \text{ mA}$ . To ensure the independent operation of the two half-modules, a configuration with one power supply per half-module has been adopted. During the first test run, the detector had been

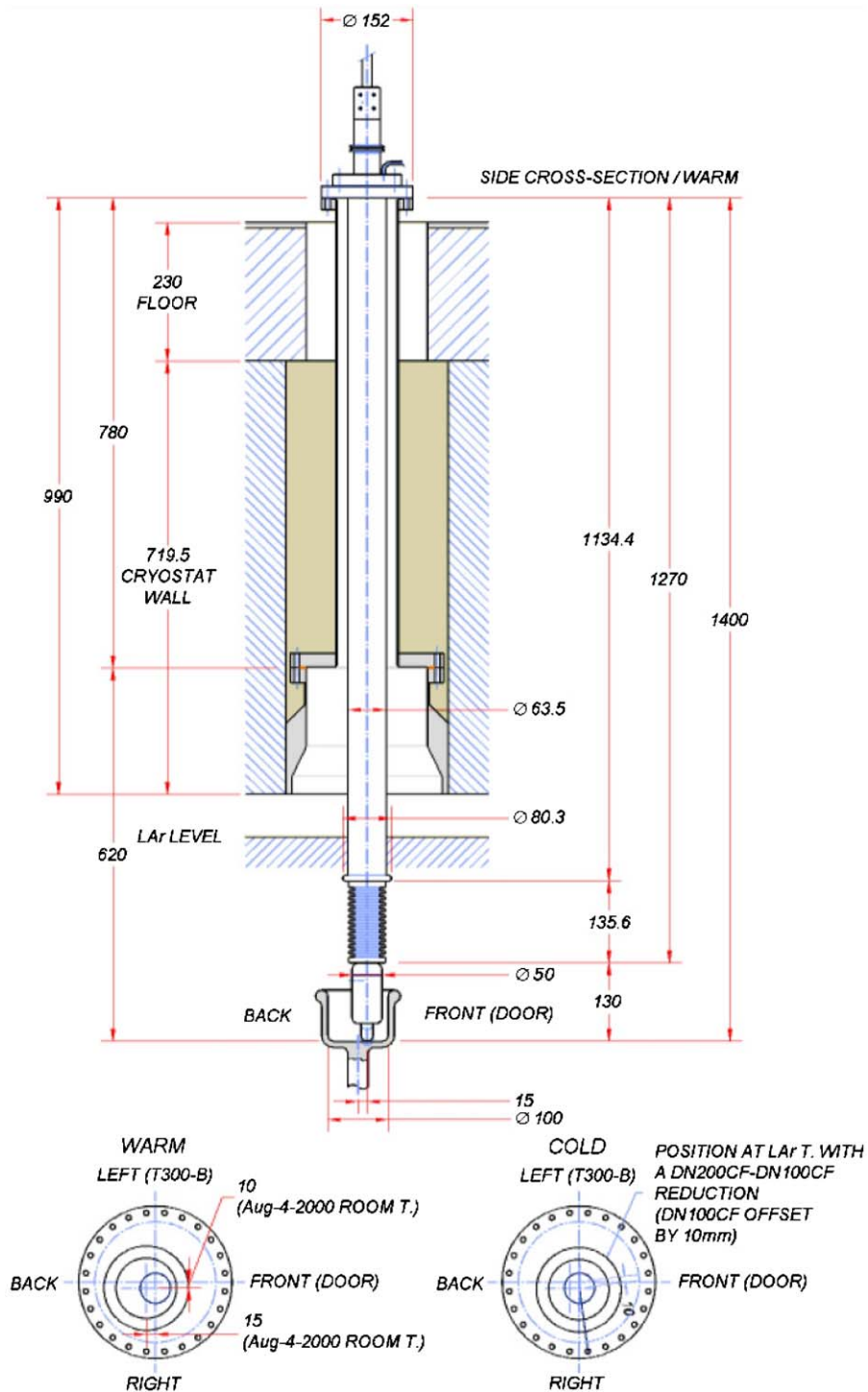


Fig. 38. The HV feedthrough position for the T600 detector. The lower figure describes the displacement of the feedthrough position due to thermal shrinks of the aluminium cryostat walls with respect to the female contact anchored to the stainless-steel cathode.

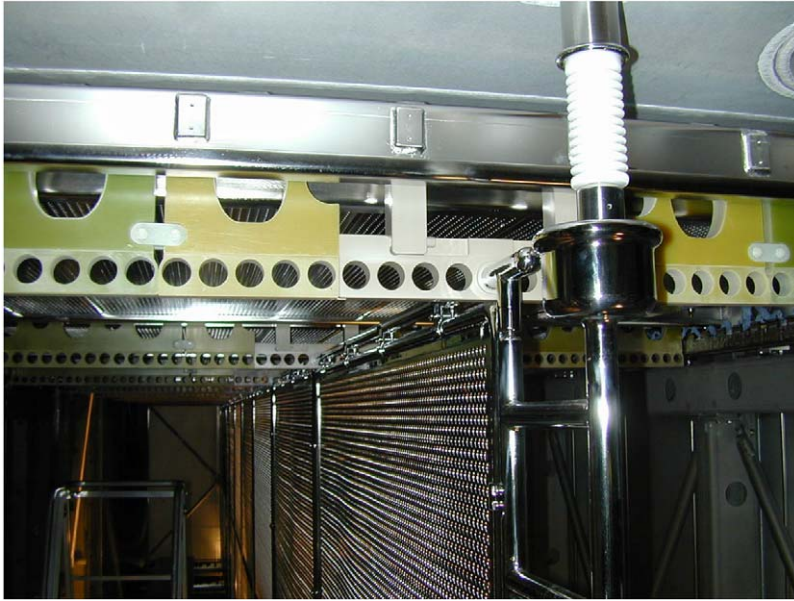


Fig. 39. Picture of the HV feedthrough and cup.

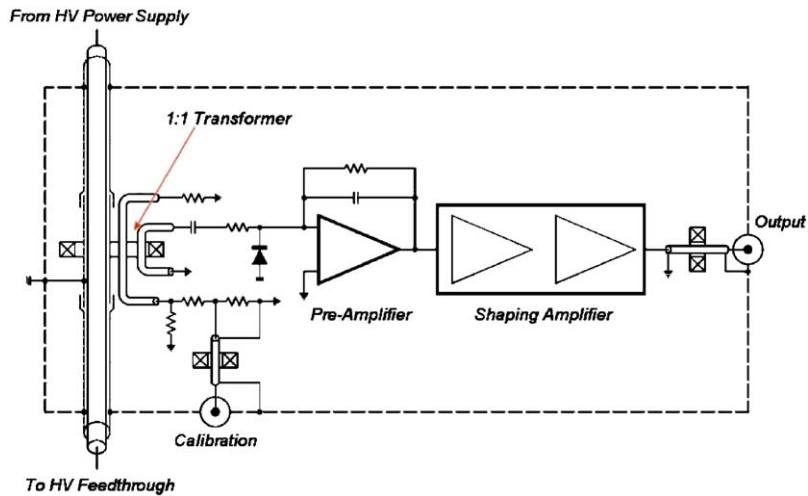


Fig. 40. Principle diagram of the “corona detector” module.

operated with  $HV = -150 \text{ kV}$  and  $I = 1 \text{ mA}$  to perform tests on HV components at twice the nominal voltage and verify the possibility of safe operation with a factor of two longer ( $\sim 3 \text{ m}$ ) drift length. Data of the power supply are reported in Table 9.

The PNC5 150.000-1 power supply has one of the best residual ripple figures between those available on the market. The HV cable has a polyethylene dielectric and its inner and outer conductors are wrapped with conductive plastics to ensure a uniform field across the dielectric. Its

linear capacitance is of about 100 pF/m. The residual voltage ripple at the maximum value of  $I = 1$  mA is quoted to be  $\leq 10^{-5} \times HV$  peak-to-

Table 9  
HV power supply data

Producer	Heinzinger
Model	PNC5 150.000-1 negative, switch mode, HV power supplies
Output voltage	0–150 000 V adjustable
Output current	0–1 mA adjustable
V-Ripple, p/p	$\leq 10^{-5}$ for voltage
Stability, p/p	$\leq 5 \times 10^{-4}$ for current
Temp. coefficient, p/p	$\leq 1 \times 10^{-4}/K$ for current
I-Ripple, p/p	$\leq 5 \times 10^{-4}$ for current

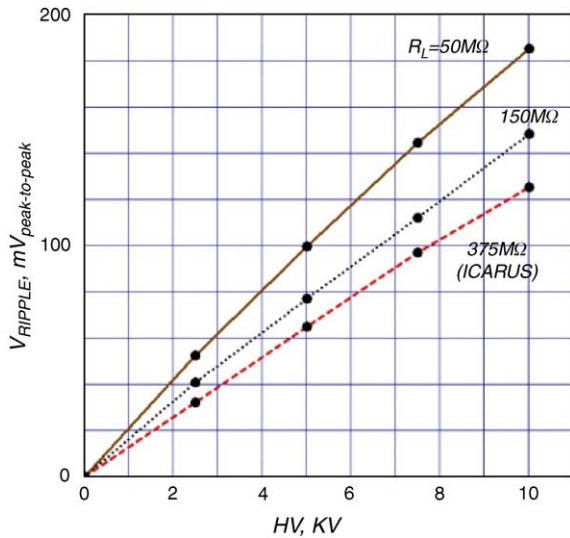


Fig. 41. Dependence of the voltage ripple (peak-to-peak) on the HV for different load resistors. (a) Solid line:  $R_L = 50$  M $\Omega$ ; (b) dotted line:  $R_L = 150$  M $\Omega$ ; (c) dashed line:  $R_L = 375$  M $\Omega$  (T600 working conditions).

peak. Under the operating conditions of the T300 for HV and current (HV = –75 kV,  $I = 0.4$  mA for each chamber = 0.2 mA) the residual ripple is reduced to 150 mV peak-to-peak.

The residual voltage ripple results to be the convolution of two contributions: (a) the 50 Hz ripple: 0.1 V peak-to-peak, independent from the output voltage and (b) the power supply switching frequency (37.45 kHz) residual ripple, a linear function of the output voltage and current, as shown in Fig. 41. For a further ripple reduction an additional filter had been designed and built. Fig. 42 shows the filter schematics. The rejection filter, a two-stage RC filter with time constants of  $\approx 10$  and  $\approx 14$  ms, consists of the 5.85 M $\Omega$  output resistor ( $R_{OUT}$ ) of the power supply, of the 16 m cable ( $C_{LINE} = 1.65$  nF) connecting the power supply to the HV feedthrough, of the 5 M $\Omega$  resistor ( $R_{FT}$ ) at the inner feedthrough end and of the capacitor  $C_{DEGR}$  (2.9 nF), formed by the capacitance of the cathode towards ground and by the field electrodes. The filter is able to remove the high-frequency ripple component and to attenuate by more than a factor of three ( $4 \times 10^{-7}$  p/p at –75 kV) the 50 Hz component.

As far as the read-out electronics is concerned, this residual ripple has only effect on the first wire plane (horizontal coordinate). This effect is reduced by the (drift time)/(ripple period) ratio ( $\sim \frac{1}{20}$ ) and by the finite bandwidth of the amplifier. The filter efficiency has been verified during normal data-acquisition conditions.

Results of the Fourier analysis of the noise signals on the TPC wires of the most exposed plane (Induction-1) are displayed in Fig. 43 for different HV conditions. The spectra clearly show

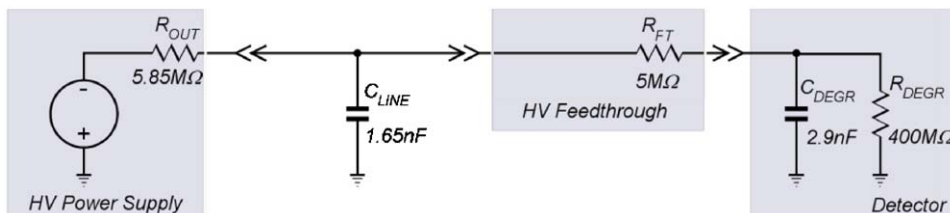


Fig. 42. Electric scheme of the external ripple rejection filter.

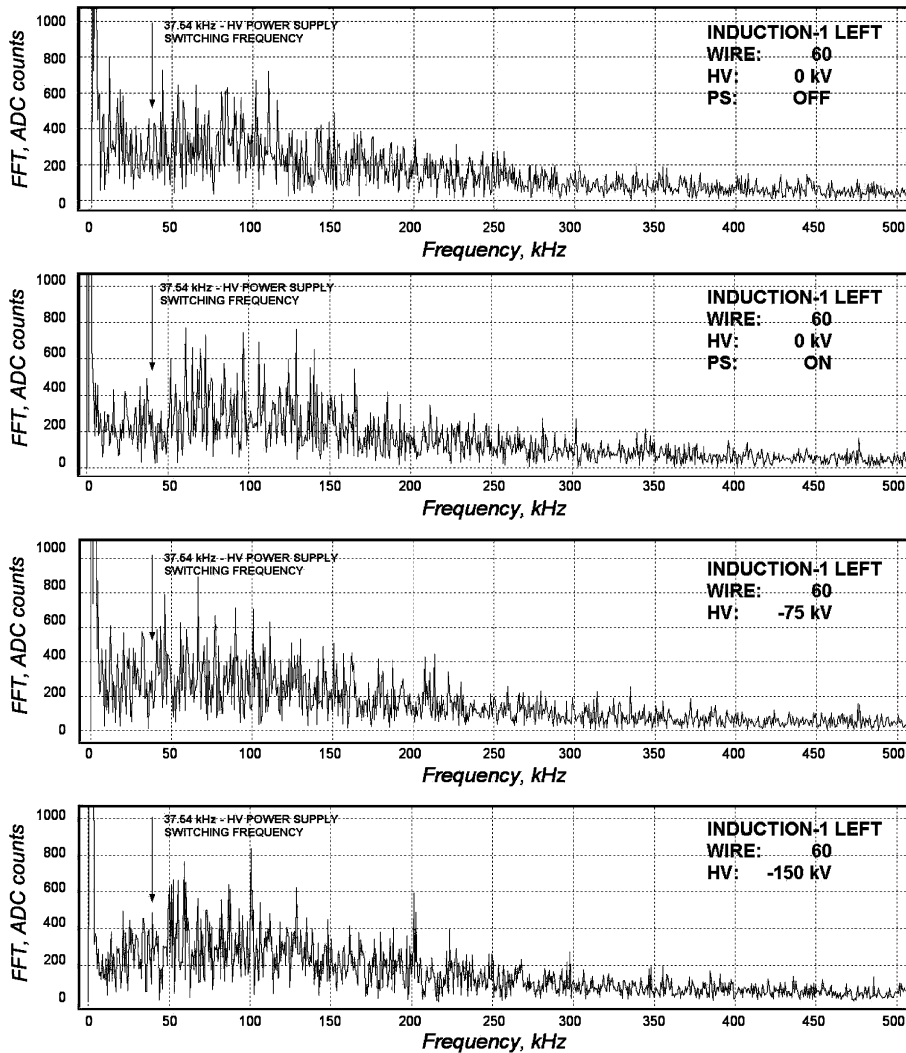


Fig. 43. Fast Fourier transform spectra of the signals on the wire number 60, in the Induction-1 left wire plane, with HV values of 0,  $-75$  and  $-150$  kV, respectively.

that there are no special peaks at the frequency of the switching power supply.

### 10.5. HV monitoring feedthrough

The HV operating conditions are locally monitored by displaying voltage and supplied current on the power supply instruments. Moreover, on each of the four voltage divider chains two of the four  $100\text{ M}\Omega$  resistors have an intermediate con-

tact at  $300\text{ k}\Omega$  towards ground (Fig. 36). This contact allows to measure a monitor voltage  $V_m = 10^{-4}$  times the voltage applied to the cathode, i.e. for a nominal voltage of  $-75\text{ kV}$  one has  $V_m = -7.5\text{ V}$ .

In the T600 the four voltages  $V_m$  are read out through coaxial cables connected to two feedthrough flanges. On the outer sides of the flanges a  $10\text{ k}\Omega$  series resistor and a diode limiter circuit protect the measuring instrumentation in case of

voltage spikes. A ferrite-based filter is used to prevent common mode external noise to enter the detector.

The four  $V_m$  values, the power supply voltage and current, together with the status of the voltage and current limit and the ON/OFF switch operation, are transmitted via a custom-made module to an analog-to-Ethernet interface (Burr Brown EDAS-1000). The EDAS-1000 interface allows for the remote monitoring of the T600 HV status; it receives analog signals to remotely control the setting of the maximum HV and of the current limit, as well as to programme the voltage ramp-up and ramp-down. A slow control programme has been developed for this purpose. It runs on a PC and, through Internet, takes control of the remote EDAS device. A graphic user interface allows to perform all the required operations by remote control:

- setting the ramping up/down rates and/or enabling them;
- setting the working voltage;
- setting the voltage and current limits;
- enabling the data recording on the running parameters.

## 11. Read-out electronics

### 11.1. General architecture

The read-out system is structured as a multi-channel waveform recorder that stores the charge information collected by the sense wires during the drift of electrons. Each wire is equipped with a current integrating amplifier followed by a 10 bit Flash ADC that samples the signal every 400 ns.

The converted data are stored in a digital memory for further evaluation. The scheme of this read-out chain is shown in Fig. 44.

To preserve the signal shape and to have, at the same time, a compact hardware structure, individual channels are grouped in sets of 16 and their signals are multiplexed at a rate of 40 MHz providing the required 400 ns sampling time for each channel.

The real-time analysis of the digitized signals is performed by the specially developed VLSI chip, called the hit finder chip or the DAEDALUS chip. Main functions of the chip are illustrated by the block diagram of Fig. 45. It processes four groups of four channels, starting by demultiplexing the 10 bit input data. The chip architecture is a six-stage pipeline: one stage is dedicated to demultiplex inputs, one to multiplex outputs, one to perform median filtering, while the hit finder requires three stages. Data move through the pipeline at a frequency of 2.5 MHz that matches the input data rate. The chip features programmable operating parameters: median filter size (up to 15 points), window size (up to 15 counts) and all the threshold values.

The chip development started with the prototypes operating on four channels and designed in VLSI 0.7  $\mu\text{m}$  CMOS standard cell technology. They performed according to the specifications. The final version of the chip has been designed in VLSI 0.5  $\mu\text{m}$  CMOS gate array technology and, as described above, it operates on a set of 16 channels.

The front-end electronics consists of three basic electronic modules, operating on sets of 32 channels: the decoupling board, the analog board and the digital board hosting two DAEDALUS chips. The modules are shown in Fig. 46

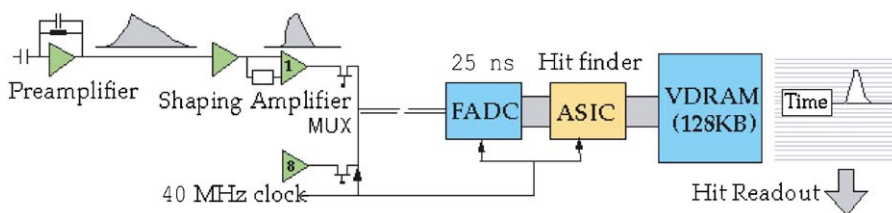


Fig. 44. Single wire read-out scheme.

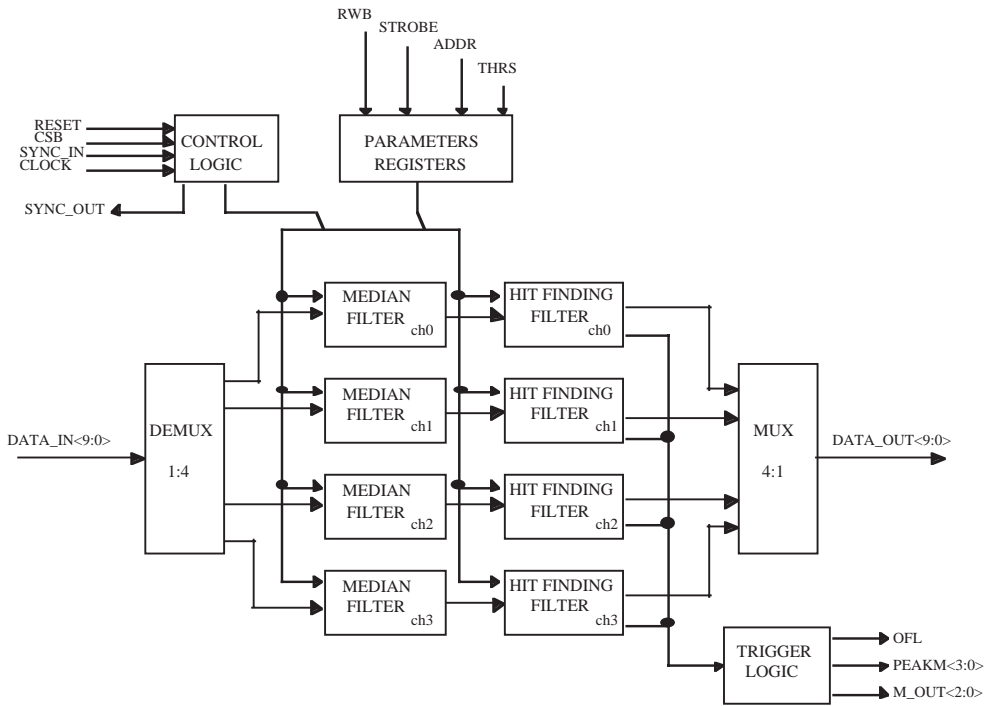


Fig. 45. Block diagram of the hit finder chip.

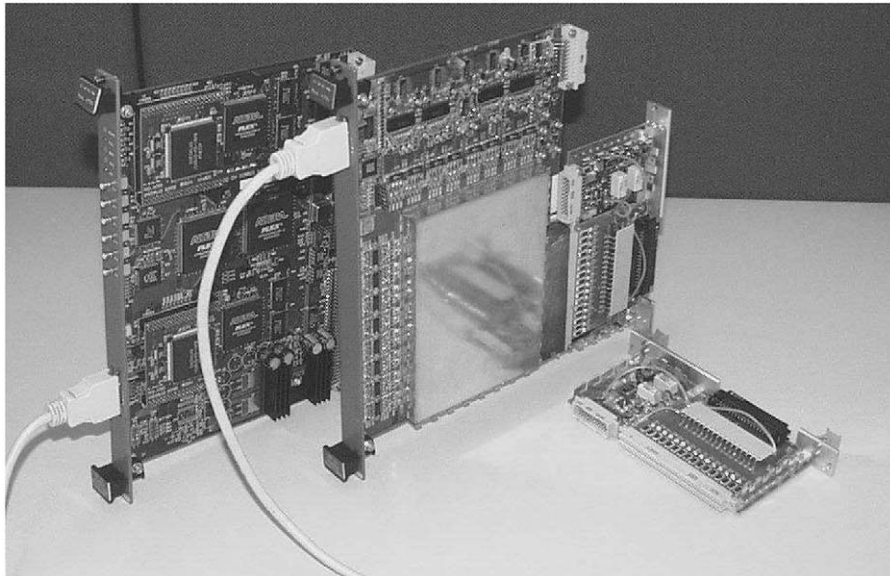


Fig. 46. The three basic electronics modules: the small decoupling board (DB) that receives 32 analog signals from the chamber via the feedthrough and passes them to the analog board; the analog board (V791 by CAEN) that houses the amplifiers for 32 channels; the digital board (V789 by CAEN) Arianna that has the two DAEDALUS VLSI, mounted onto small piggy back PCBs.



Fig. 47. The top of one T300 module showing the disposition of the electronic racks for the left chamber and of the chimneys with the feedthrough flanges for the right chamber.

and are discussed in detail in the following subsection.

The read-out scheme of the whole detector is organized in units. Each unit is made of a 30 unit rack that houses one VME-like analog crate (with 18 analog modules in front and 18 decoupling boards in the backplane), one digital crate (with 18 digital modules), the relative power supplies and their control and monitor. Therefore, a single unit can provide up to 576 read-out channels (18 modules of 32 channels each). In order to minimize the input capacitance due to the signal cables, the racks are positioned on top of the cryostat close to the signal feedthrough flanges (Fig. 47) mounted at the end of the chimneys.

For each T300 detector, 48 units in total (one per feedthrough flange) are used for the read out of the wires from the two, left and right, chambers (Table 6):

- 8 units are used for the horizontal wires of the Induction-1 planes (4 units for the left chamber

and 4 for the right one, placed at the corners of the cryostat ceiling), with 528 connected channels per unit (corresponding to  $2 \times 2112$  wires in total).

- 36 units (in two rows of 18 units each, one for the left and one for the right chamber) are used for the wires at  $\pm 60^\circ$  of the Induction-2 and Collection planes. In each of these units one half of the boards are dedicated to the Collection plane and one half to the Induction-2 plane. All 576 channels per unit are connected, with the exception of four units,<sup>19</sup> the first and the last of each row, with 448 connected channels (corresponding to  $4 \times 5056$  wires in total).
- the remaining 4 units (two per chamber, at the corners of the cryostat ceiling), each one with 544 connected channels, serve the wires of decreasing length at  $\pm 60^\circ$  from the corners of

<sup>19</sup>Part of the channels of each of these units serve a portion of wires from the corners (416 channels).

the wire frame (corresponding to  $4 \times 544$  wires in total).

The total number of electronic channels connected to wires is  $2 \times 13\,312$  per T300 module (53 248 in total for the T600).

### 11.2. Front-end electronics

The front-end electronics is composed of three basic modules. The first is the decoupling board (A764): it receives 32 analog signals from the wire chamber and passes them to the analog board via a decoupling capacitor of 4.7 nF, large compared to the input (wire+cable) capacitance (average value  $\sim 400$  pF for the horizontal wires of the Induction-1 plane and  $\sim 200$  pF for the wires at  $\pm 60^\circ$  of the Induction-2 and Collection planes, as discussed in Section 7.5); it also provides biasing (up to 500 V) of each electrode via a 100 M $\Omega$  resistor and the distribution of the test signals. The decoupling board is housed in the back side of a VME-like crate that houses in front the analog boards.

The second module is the analog board (CAEN-V791): it houses the amplifiers for 32 channels, based on the proprietary analog BiCMOS VLSI (two channels per chip); it also provides 16:1 multiplexing and analog-to-digital data conversion (10 bit) at 40 MHz rate. The data are transmitted to the digital board via a serial-link cable (21 bit) connected to the front panel.

The third module is the digital board (CAEN-V789) ARIANNA; it is housed in a VME crate and holds two DAEDALUS VLSI chips for hit finding and zero suppression, mounted onto a small piggy back PCB; the board serves 32 channels and receives the digital data (multiplexed) from the cable plugged into the front panel. The data are available via the VME bus.

#### 11.2.1. Analog crate

The analog crate is used to perform the following functions:

- distribution and decoupling of the bias voltage to the wires (A764);
- test pulse distribution and setting of baselines (V793);
- accommodation for 18 analog boards providing amplification, shaping multiplexing and analog to digital conversion (CAEN-V791).

The essential elements of the analog board are reviewed here:

*The front-end amplifier:* The schematics of the front-end pre-amplifier mounted onto the CAEN-V791 analog boards (32 channels per board) is shown in Fig. 48. The circuit is an integrator with a feedback time constant  $\tau_f = R_f C_f$  followed by a base-line restorer. The latter is introduced to attenuate the low-frequency fluctuations of the signal baseline and is characterized by a time constant  $\tau_r = (R_1 || R_2) C_z$ .

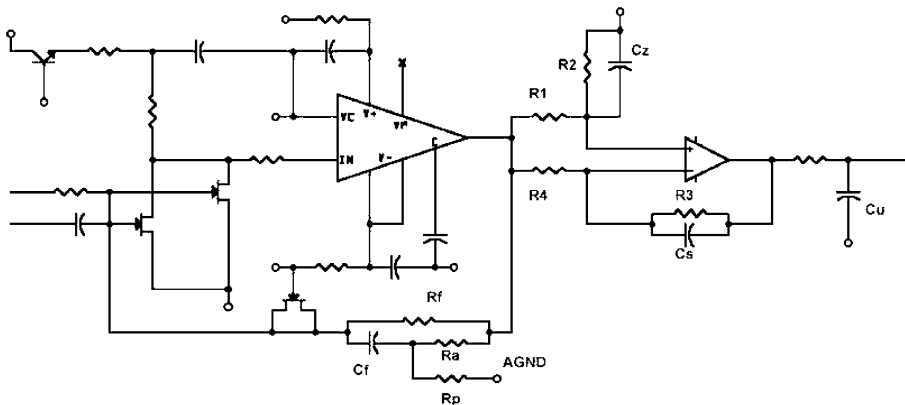


Fig. 48. Schematic layout of the front-end amplifier mounted onto the CAEN-V791 analog boards.

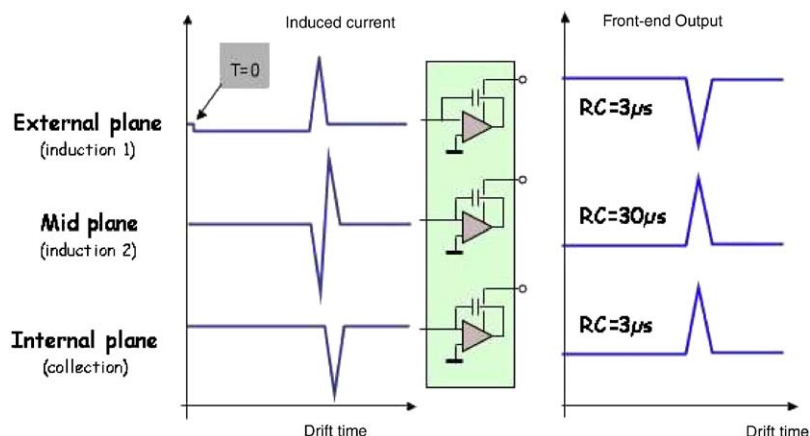


Fig. 49. Sketch of the signal shapes from the three ICARUS read-out planes.

Two versions of the CAEN-V791 analog boards are used in the DAQ chain. In order to avoid pile up and maximize the dynamic range, it was decided to adopt a “quasi-current” configuration (V791C) for the Collection plane and the Induction-1 plane where the induced current yields an approximately unipolar signal (Fig. 49). This means that the feedback amplifier time constant is small with respect to the typical signal width (3  $\mu$ s).

A “quasi-charge” configuration (V791Q: approximate integrator with long  $\tau_f$  with respect to signal width) was preferred for the Induction-2 plane (middle plane in Fig. 49), where the induced current is bipolar, because it allows the conditioning of the signal in such a way that the shape is similar to that of the other two planes. Both boards were optimized in terms of gain and signal-to-noise ratio in a test campaign performed with the 501 prototype detector [4].

The feedback constant is  $\tau_f \approx 1.6 \mu$ s on the V791C board and the gain is  $5.5 \pm 0.5$  ADC counts/fC. The electronic noise calculated in a time window of 50–100  $\mu$ s (comparable with a typical width over which a signal is searched for) is about 1.2 ADC counts for an input capacitance of 400 pF. Given the short value of  $\tau_f$  the base-line restorer does not play an important role, and therefore its time constant is set to a very high value ( $\tau_r \approx 100$  ms).

The overall decay time on the V791Q board was chosen to be  $\approx 30 \mu$ s (very large compared to the typical signal width). This value was obtained by combining a feedback time constant  $\tau_f$  of 100  $\mu$ s with a base-line restorer time constant  $\tau_r$  of 33  $\mu$ s. In this configuration the gain is  $6.5 \pm 0.5$  ADC counts/fC and the electronic noise is less than 1.2 ADC counts. Low-frequency fluctuations are present but do not affect signal reconstruction; the effect is mainly a reduction of the dynamic range of the whole read-out chain.

After the technical run in Pavia the performance of the V791 boards mounted onto the first T300 were found to be very close to the design values; only a slightly higher value of the electronic noise was measured (1.7 ADC counts) and this has been interpreted as due to the harsh environmental conditions in the assembly hall in Pavia.

*The analog to digital conversion:* The 32 analog signals treated by the ICARUS pre-amplifiers are also multiplexed (16:1) on the CAEN-V791 board, converted to 10 bit by Flash ADCs and sent to the digital board via a serial link (21 bit wide) at the rate of 40 MHz. Each channel is sampled every 400 ns; due to the multiplexing the actual sampling time is slightly shifted from channel to channel within the 400 ns period. The typical dynamic range of the whole chain is about 100, given that one minimum ionizing particle releases about 2 fC/wire or equivalently 10–12 ADC counts/wire.

*The calibration system:* Test capacitances with nominal value of  $1 \text{ pF} \pm 3\%$  are present at critical locations along the amplification chain: on the analog board itself, in front of the pre-amplifiers and on the decoupling board (A764). They have been used to determine gain and linearity of the read-out chain and the wire-to-wire uniformity (Section 7.6). Test pulses of any shape can be applied independently at different calibration points via the control module V793. On the decoupling board odd and even channels can be pulsed separately (for cross-talk measurement). Another test capacitance is located at the far end of the read-out wire, essentially to test the full availability of the read-out chain.

### 11.2.2. Digital crate

Following the digitalization, the whole of the read-out channel waveform streams are brought to the boards placed in the digital crate. This is where waveforms are temporarily stored and data buffers are formatted in occurrence of any given trigger condition. Eighteen digital boards sit on this VME crate together with a VME CPU and a trigger/clock distributor, handling a total of 576 channels.

*The V789:* Each board handles 32 channels and provides memory buffers, data reduction processing and trigger logic. A dual serial digital link brings two channel samples every 25 ns (16 channels are interlaced providing an effective 400 ns sampling rate). Incoming data are buffered on a circular buffer, which length is programmable from 64 to 4096 samples. In parallel, the stream is also evaluated by the DAEDALUS processor searching for signal shapes which fulfill the parametrized discrimination.

When a trigger condition is recognized by the trigger logic (external trigger, DAEDALUS trigger, etc.) the current buffer is frozen, a corresponding entry is pushed on a “First-in First-out” register (FIFO), and recording is switched to the next free buffer within the following sample with no intrinsic dead time. Together with the raw digitized data the buffer content is tagged with channel identification, trigger condition pattern and an absolute time field (clocked with 50 ns resolution).

*The DAEDALUS chip:* The digitized waveform data throughput entering each digital board reaches 160 Mb/s, whereas the interesting portion of the waveform takes only a little fraction. In order to reduce this throughput and its side effects such as dead time due to bandwidth limitations on building, huge event size, etc. an online data reduction device has been implemented within the read-out chain, aiming at a factor 100 of event size reduction. This function is performed by the DAEDALUS chip, which detects the region of interest (ROI) within the incoming waveforms.

An ROI is defined as a time window around a rising edge (hit). To identify a rising slope, one firstly computes the differences between each two consecutive signal samples inside a time-sliding window of fixed size (window size). Positive differences are accumulated, whereas occurrence of negative and null differences are counted. A hit is found when, for a given time window, the positive sum is above a fixed threshold (rising-sum-threshold) and the number of zero counter values are below two other thresholds (rising-zero-count and rising-negative-count). The end of the rising edge is detected when two conditions are met: the positive sum is below a given threshold (falling-sum-thresholds) and at least one of the two counters is above its corresponding threshold (falling-zero-count and falling-negative-count).

The DAEDALUS parameters need to be tuned on specific signal shapes. Most of the events collected during the technical run were taken with data reduction disabled. A software simulated DAEDALUS off-line processing can allow to find the set of parameters that optimize the track detection efficiency while minimizing the collection of spurious signals. These parameters will be used for the on-line data reduction for the next runs of the T600 detector.

*The V816:* This board receives the set of signals required for synchronization and trigger from the distribution and forwards them on a customized P2 backplane to the digital boards. This module can also be used to generate locally the required signals for test and diagnostics and to source fake data on a digital link output to stimulate single digital boards, hence allowing the acquisition without a whole DAQ chain.

*The MVME2100:* Each digital crate is equipped with a front-end read-out CPU (PPC 8240) embedded in a Motorola MVME 2100 board. This board provides the interface to the VME bus and the data-acquisition network through a 100 Mb/s Fast-Ethernet port, and is responsible for the local buffering and building of data fragments. Furthermore, this unit is also responsible for the parameter setting of the local DAEDALUS trigger logic. Given the available data processing resources a possible improvement implementing data compression algorithms at this level of the DAQ system is under study. The CPU software has been run under VxWorks real-time OS environment but work is in progress to port also the front-end part of the read-out software under the Linux OS.

### 11.2.3. Remote control rack

A custom-built controller resides in the read-out rack. Connected through an I<sup>2</sup>C bus, this device controls and monitors all the power supplies and drives the fan speed on the heat exchanger. Racks were built air tight to reduce the need of accessing the electronics after installation and keeping the internal temperature within operating ranges. Eight remote controllable digital I/O channels are also available for general use.

## 12. Data-acquisition system

Given the characteristics of the detector, the data-acquisition system (DAQ in the following) has been designed to allow a continuous data recording of the events occurring inside the drift chambers, avoiding as much as possible intrinsic dead time to meet the “continuously sensitive” feature of the detector. Strong design issues are that the system must be able to operate in the absence of any external trigger signals and to acquire data from different independent sources containing fragments of the same physics event.

### 12.1. DAQ layout

The data-acquisition system was based on the following assumptions:

- 96 electronics racks, hosting up to 55 296 digitizing channels;
- local buffering up to 4096 10-bit samples for each channel (1.6 ms);
- network architecture merging data from multiple independent sources;
- maximum sustained single hit rate of 1 Hz/wire (2 Mb/s/crate; ~200 Mb/s for the whole detector);
- intermediate data storage able to decouple raw data acquisition from pseudo-on-line filtering;
- at least four writing workstations to handle the data stream.

The adopted DAQ network is characterized by a two-level switching architecture (Fig. 50).

The front-end electronics crates distributed on top of the cryostat have their local CPU connected through a 100 Mb/s Fast Ethernet (FE) link to a fast 24 ports FE/GE switch. In this configuration each single chamber of the T600 is mapped to one single switch, allowing, if necessary, a natural topological segmentation of the detector. The final merging of all the data coming from the four chambers is performed through a central 1 Gb/s Giga Ethernet switch, connecting all the local switches to the PC farm. A second FE/GE switch connects some utility machines to the central GE/GE switch, such as the slow control units, run control tasks, external trigger interface and tape storage unit. There is also an interface with the cryostat monitoring machines provided by Air Liquide.

The main feature of the adopted design is that the PCs can have flexible roles since they can simply write data on file or execute filtering procedures, or run the event display. Each workstation receives event data until its disk is full and then gives the control to another PC while running the data processing, or, following a round-robin scheme, can process one single event at a time. Such architecture is open for scalability since the number of PCs in the farm can be selected according to processing power requirements and, thanks to the switched network, the bandwidth can be easily distributed among multiple workstations.

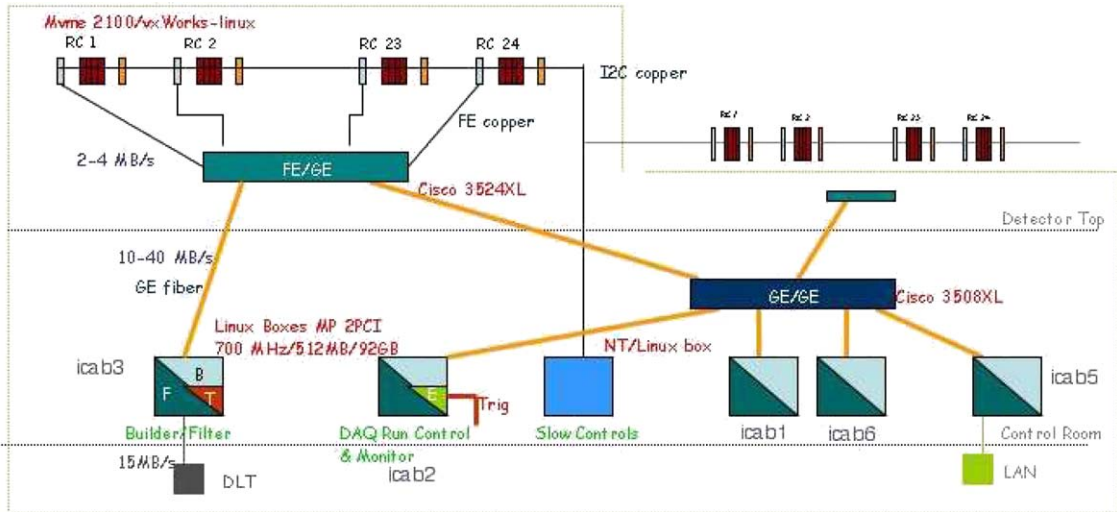


Fig. 50. Scheme of the architecture of the data-acquisition system.

## 12.2. Event building

The event builder has to merge fragments of data belonging to the same physical event appearing on any of the units and spread over a time window which can go up to one drift length (one or more milliseconds). The builder is based on a  $m \times n$  node switched network which interconnects all the DAQ components. The present layout provides a single receiving and merging workstation handling a complete read-out of one T300 (24 read-out units) thus reaching a maximum expected input of  $\sim 50$  Mb/s and safely exploiting the link at one-half of the available throughput. The event builder is composed of the following pieces:

*The event manager (EVM):* The main task of the event manager is to monitor the data flow collecting all the status and error messages, regulating trigger acceptance and the data destination selection. The system has also the responsibility of handling the system configuration, and to monitor dynamically the availability of the hardware running around the system. The EVM machine hosts a customized I/O board which feeds the trigger and the absolute clock and provides the synchronizing output (busy). Typical messaging rates the EVM can handle range around 1–2 kHz.

*The read-out unit CPU:* According to the configuration messages, it initializes the digital front-end boards. It performs the continuous scan of the front-end FIFO, moving data blocks to its internal memory as soon as any data are available. It has to generate status messages at the end of each scan loop or as soon a special condition has to be signaled and to forward them to the EVM. All data blocks and status messages are piped to the selected event writer. On “Event writer change” message it has to handshake the opening of the connection to the new destination. An additional parasitic stream can be used for online data spying. Average throughput to be handled is around 1–2 Mb/s both in input from VME and in output down into the net link.

*The event writer:* This component waits for event fragments from the active set of read-out units and merges the streams on a single file. Disk and building statistics are periodically sent back to the EVM. The parallel threads (one per read-out unit) aggregate about 20–30 Mb/s. The throughput is actually limited by the disk internal bandwidth.

## 13. The external trigger system

Detection of long muon tracks crossing the T300 detector at large zenith angles (“Horizontal

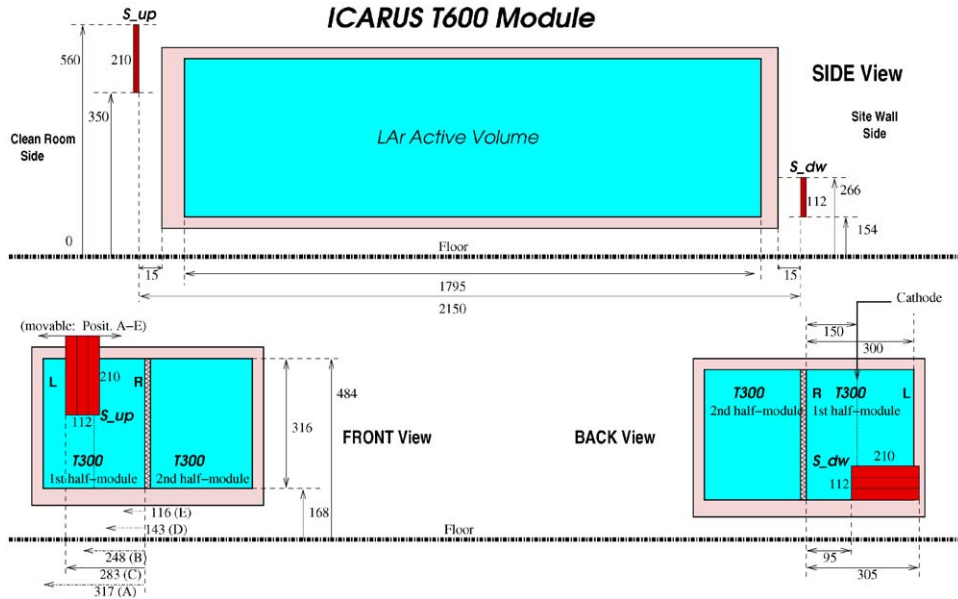


Fig. 51. Schematic view of the external trigger layout. Dimensions and position (in cm) of the  $S_{up}$  and  $S_{dw}$  layers relative to the floor and to the active LAr volume of the activated T300 unit are reported for one of the geometry used during the run (different positions for  $S_{up}$  were also tested).

Muons”,  $\mu_H$ ) along its longest dimension was one of the main goals of the test run. Collection of a large sample of such events with ionizing tracks up to  $\sim 20$  m long was deemed as extremely useful for an overall test of the detector performance, in particular, for checking the DAQ system and its capability to correctly reconstruct the event topology from several sections of the wire chamber and for a precise characterization of the detector response based on single event analyses [19].

Therefore, a dedicated external trigger system was set up to select and enable the acquisition system for this class of cosmic-ray events. The system consisted of two plastic scintillator layers suitably positioned and arranged in a proper coincidence trigger logic to pick up the interesting muon events out of the overwhelming background of atmospheric showers. Additional layers of plastic scintillators were also used for vetoing cosmic-rays coming from above.

Each scintillator layer ( $210 \times 112 \text{ cm}^2$ ) was composed of four scintillator slabs ( $210 \times 28 \text{ cm}^2$ , 2 cm thick) housed in a metallic frame.

The signal read-out was provided by a single 2 in. PMT at the light-guide end of each slab.

The geometry of the trigger set-up (Fig. 51) was designed by means of a Monte Carlo simulation, in order to optimize the acceptance of  $\mu_H$  data. The two scintillator layers  $S_{up}$  and  $S_{dw}$  were positioned at staggered heights onto the two end caps of the instrumented half-module, at a distance of 21.5 m parallel to the drift coordinate. The  $S_{up}$  plane had the bottom edge at 350 cm from the floor, while the  $S_{dw}$  plane bottom edge was at 154 cm from the floor. The  $S_{up}$  layer was movable along a rail allowing several positions with respect to the T300 active volume (positions A–E). The adopted geometry selected muons in the zenith angle range ( $\theta_{min} = 79^\circ$ ,  $\theta_{max} = 88^\circ$ ) and within about  $9^\circ$  range in azimuthal angle for any position of  $S_{up}$ . This corresponded to muon track lengths of  $l_{min} \simeq 15.5$  m,  $l_{max} \simeq 18.5$  m in the LAr-sensitive volume.

The signature for  $\mu_H$  events was provided by the measurement of the muon time-of-flight (ToF) from  $S_{up}$  to  $S_{dw}$ . Assuming ultra-relativistic muons and taking into account the distance between the

two planes and the geometrical acceptance, the ToF range was expected from 68 to 72 ns. The time resolution for a single PMT hit is of the order of 5 ns, considering the typical rise time of the PMT signal; therefore the ToF, recorded via CAMAC TDC, could be determined with about 10 ns of precision for  $\mu_H$  crossing the two planes.

Physical background events are mainly expected from air showers. Stochastic background of accidental coincidences from the slabs of the two layers is also unavoidably present. A suitable trigger logic for  $\mu_H$  was set up to discard most of the shower events by realizing a standard NIM “Exclusive OR” logic among the four slabs of each layer (i.e. requiring *one and not more than one* hit per layer from *any* of the four slabs), followed by an “AND” logic among the two layers. Most of air showers produce hits in more than one slab of the two layers. With the implemented logics these events were largely reduced.

Analog signals from the PMTs were discriminated to provide NIM signals with a given width of 35 ns. Logic signals from  $S_{up}$  were delayed by 70 ns, in order to have  $S_{up}$  and  $S_{dw}$  signals overlapping at the AND logic input stage in case of physical signals ( $\mu_H$ ). The choice of 35 ns for the width of the  $S_{up}$  and  $S_{dw}$  signals allowed to collect triggers in a range of about  $\Delta t_{trig} = 70$  ns centred around the crossing muon ToF peak.

The trigger signal to the DAQ was provided by the AND logic output with a fixed delay. The expected trigger rate of crossing muons at sea level

(Pavia experimental hall) was evaluated by Monte Carlo simulations. Exact dimensions and material composition of the T300 and of the trigger system have been coded. The cosmic muon flux was generated according to appropriate energy and to zenith/azimuth angle distributions. For the latter, a suitable function has been used to take into account the flux increment at large zenith angle for higher energy muons. The integral flux has been normalized to a sea-level reference value of  $\Phi_{tot} = 1.3 \times 10^2$  Hz/m<sup>2</sup> [25].

An expected  $\mu_H$  rate of  $R_{\mu}^{MC}(T300) = (0.029 \pm 0.015)$  Hz corresponding to two muons per minute crossing the T300 detector was obtained. The error comes from the absolute flux normalization and from uncertainties on the zenith angle distribution at large zenith angles. The minimum energy of muons enabling the trigger logic is 3.7 GeV, while the average muon energy is 29.2 GeV. The average deposited energy in the LAr-sensitive volume is 3.8 GeV (i.e. the energy needed to cross an average length of 16.6 m in the LAr volume). As an example the 3D off-line reconstruction of a  $\mu_H$  event triggered by the external trigger system is shown in Fig. 52. The track is about 18 m long and corresponds to a total energy deposition of about 4 GeV.

During the test run the total trigger rate of the external trigger has been routinely monitored whenever a  $\mu_H$  run was started. The average total trigger rate was  $R_{tot}^{meas}(T300) = 0.2$  Hz.

The DAQ system was not able to read out and record information from the whole detector at the

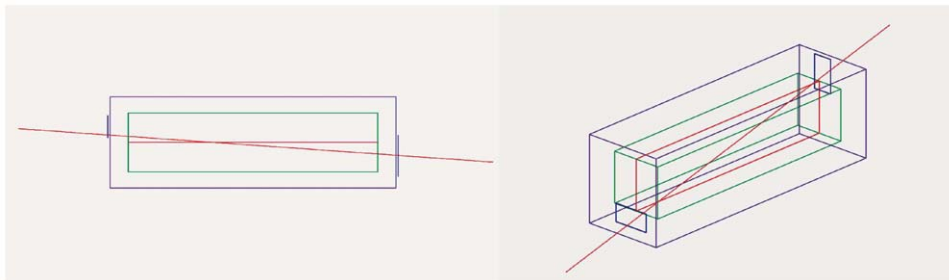


Fig. 52. Run 893, Event 4. 3D reconstruction of a 18 m long, penetrating muon track. The track, triggered by the external scintillator system, is first detected by the right chamber and, after crossing the central cathode, by the left chamber. The absolute orientation is  $\theta_{Zenith} = 80.9^\circ$ ,  $\phi_{Azimuth} = 92.9^\circ$ ; the deposited energy is  $\sim 4$  GeV.

speed required by the trigger rate. The DAQ rate was on the average about a factor ten lower.  $\mu_H$  events were selected from background by off-line visual scanning. The signal-to-background ratio was of the order of  $\frac{1}{13}$ , in agreement with expectations.

## 14. Commissioning and technical run

The T600 detector was commissioned in the assembly hall in Pavia in April 2001. The main purpose of the following tests was the check of the overall detector functionality and also a concluding demonstration of the detector technology as realized with industrial construction techniques at a scale appropriate for physics.

The test was performed with the first half-module fully assembled, instrumented and filled with LAr, while the second one was left empty, although functional from the point of view of cryogenics but with no inner detector and purification systems installed.

A test programme for a total nominal duration of about 3 months was set up covering all the relevant technical aspects:

- cryogenics;
- LAr purification;
- wire chamber mechanics;
- HV systems;
- read-out electronics;
- DAQ;
- slow control system and auxiliary instrumentation;
- LAr scintillation light detection and read out;
- automatic control system for cryogenics.

Cosmic-ray event runs with different trigger conditions were taken in order to study the features of the reconstruction and analysis programs and to test and optimize the event simulations. Apart from an excessive LN<sub>2</sub> consumption rate for the detector cooling, the test run was completely successful. The detector went smoothly into operation with all the subsystems performing according to their nominal specifications. The run lasted 104 days including the start-up and shut-down phases of 36 days. During the 68 days of

detector lifetime about 30 000 cosmic-ray events were collected and their analysis is currently in progress. A summary of the relevant technical results obtained from the test run is reported in the following paragraphs.

### 14.1. Start-up procedure

The process of bringing the dewar from the initial room temperature conditions to the completion of the filling with purified LAr is the most delicate phase of the detector commissioning since it requires the activation of several subsystems in three main phases:

- (1) vacuum pumping in the inner volume;
- (2) cooling of the cryostat and of the inner detector structures;
- (3) filling with purified LAr.

The final goal of the process is to obtain a LAr purity corresponding to a drift electron lifetime of about 100  $\mu$ s. These operations must be carried out under specified thermal conditions in order to avoid excessive stress of the inner detector structures. A number of sensors integrated with a common read-out and display interface (Section 9), provides a continuous monitoring of all the relevant parameters:

- temperatures of the inner detector and cryostat structures;
- pressure in the main cryostat;
- deformations of the LAr container and movement of the wire tensioning devices;
- LAr purity and level.

On the other hand, the *automatic control system* of part of the cryogenics and purification devices provides a direct control of the cooling and purification systems allowing for their remote handling, and providing a continuous monitoring and storage of the working parameters (valves apertures, temperatures along the transfer lines, pressures at various locations on the argon and nitrogen circuits, pumps speed, etc.). Several automatic procedures have been implemented to set ON/OFF the various subsystems and to handle both steady-state and emergency conditions on the basis of a set of critical parameters.

### 14.1.1. Vacuum

The first operation of the start-up procedure is the vacuum pumping of the volumes to be filled with LAr or GAr, in order to remove air and other polluting gases. This includes the main LAr volume, and also the purifiers, the argon transfer lines and recirculation units. During this phase all the valves connecting these volumes are opened. The target pressure in the main volume is  $10^{-3}$  mbar or less required to reach the so-called molecular regime and let all surfaces (in particular, cables and plastic components) to outgas the impurities collected during the detector assembly. We recall that all the materials installed in the inner detector passed a cleaning procedure including washing in ultrasonic bath and drying in vacuum oven and remained packed into an inert gas atmosphere (nitrogen or argon) until assembly. However, after the assembly, they remained exposed to the atmosphere for a rather long period.

During the evacuation the aluminium container suffers the largest mechanical load (both the containers were previously tested for mechanical stiffness and vacuum tightness in the assembly workshop). Therefore, the deformations of the container walls during the test run were monitored by means of the slow control system described in Section 9.

Search for major leaks was carried out by operating the LAr container at moderate high and low pressures (1.3–0.3 bar abs) before the final vacuum pumping started. The pumping system is composed of four identical groups, each consisting of a 24 m<sup>3</sup>/h primary, dry-scroll pump and of a 1000 l/s turbo-drag pump installed on four DN200 ports on top of the LAr container.

The turbo-molecular pumps are switched on when the pressure of 1 mbar is reached. For a pressure below  $10^{-1}$  mbar (this is normally achieved after 20 h) further systematic searches for leaks start. Fig. 53 shows the pressure in the cryostat during the pumping phase as a function of the effective pumping time. This curve is compatible with the simulations made for the design of the pumping system.

The displacement of the walls, as a function of the internal pressure and of the time is shown in Figs. 54 and 55, respectively, as measured by the eight position meters (Section 9.2). As expected from mechanical simulations and tests made at the Air Liquid workshop, the walls are deformed linearly with the pressure.

The wall deformations during the vacuum phase and a leak test with overpressure were not front/back symmetric (Fig. 56) with a maximal deformation at about a quarter of the detector length from the front end for both walls. This effect is most

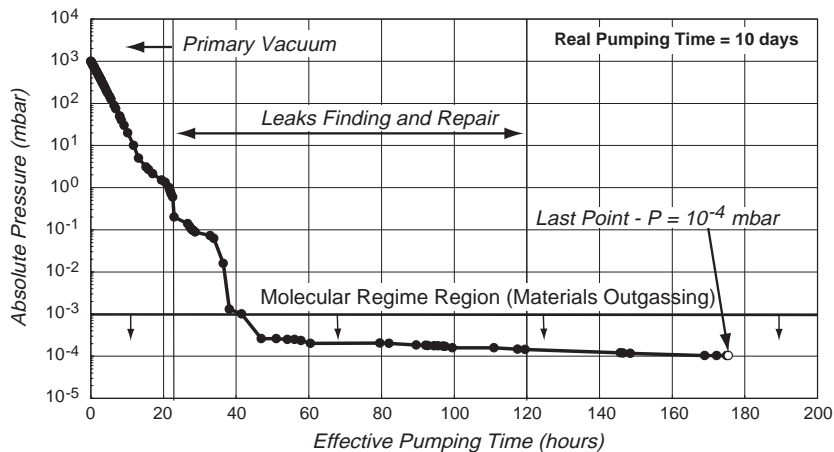


Fig. 53. Pressure in the cryostat as a function of the effective pumping time.

likely caused by the asymmetric distribution of the mechanical stress within the wall, due to the fact that the end cap at the front side is bolted through a reinforcing flange to the cryostat, whereas at the back side it is welded.

At the end of the vacuum phase the measured displacements deviated from the linear dependence on the pressure. From the moment when the turbo pumps were switched on until the vacuum breaking, the pressure change was 1 mbar and the expected movement of the walls was less than

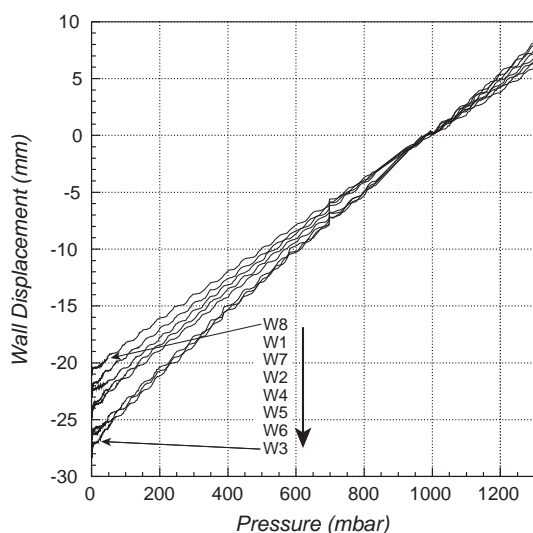


Fig. 54. Wall displacement measured by the eight wall position meters, as a function of the cryostat pressure. Positive (negative) displacement values mean outward (inward) movement (see Section 9 for the sensor's labelling).

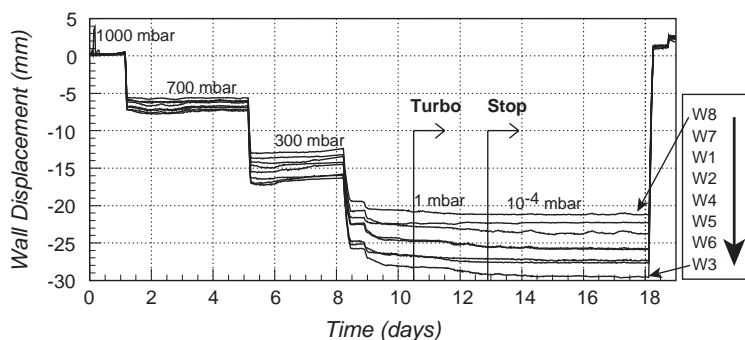


Fig. 55. Wall displacement during the vacuum phase. The approximate values of the internal pressure are given for the different time periods. The arrows indicate the time when the turbo-pumps were switched on and when they were stopped (see Section 9 for the sensor's labelling).

0.03 mm. However, the walls continued moving for about 3 days, releasing the stress in the cryostat. The right- and left-side walls moved on average by 1.4 and 0.6 mm, respectively. This left–right difference could be due to a contact of the left-side wall with the inner detector frame.

Vacuum pumping was stopped 10 days after the beginning of the operation (about 175 h of effective pumping time). The final pressure reached was  $10^{-4}$  mbar, corresponding to a global leak rate of about  $3 \times 10^{-1}$  mbar l/s, in good agreement with the expectations, given the behaviour of the various material surfaces and the time during which they were exposed to the atmosphere.

The detection of the residual gas in the dewar, performed with two quadrupoles installed on two

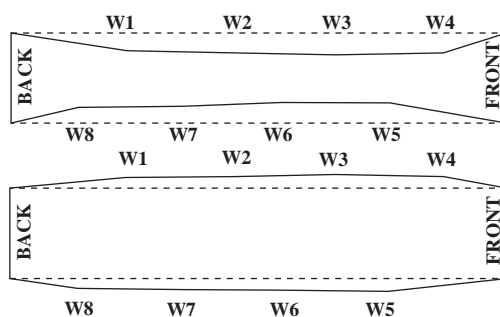


Fig. 56. Schematic top view of the cryostat walls at the moment of maximal deformation during the vacuum phase (top) and a leak search with overpressure (bottom). Indicated are the points where the deformation is measured by the wall position meters. The walls deformation is magnified.

of the top flanges, showed an appreciable content of water (from outgassing) and (less important) of air: Oxygen and nitrogen with relative weight around  $\frac{1}{3}$ , coming from real leaks or from the slow evacuation of interstices and partially closed volumes in the inner detector structures. The relative content of air and water amounted to about  $\frac{1}{10}$  showing that outgassing is the dominant source of the residual gas; contributions from other components were negligible. The vacuum was broken with purified argon gas and the cooling phase started.

#### 14.1.2. Cooling

The cooling down of the cryostat was performed in two steps:

- pre-cooling with a mixture of LN<sub>2</sub> and GN<sub>2</sub>. In order to avoid large thermal stress in case of abrupt injection of LN<sub>2</sub> into the cooling circuit, the first phase of the cooling (down to about  $-40^{\circ}\text{C}$  average internal temperature) was carried out by injecting a controlled temperature mixture of LN<sub>2</sub> and GN<sub>2</sub>;
- cooling with LN<sub>2</sub> pressurized at 2.4 bar abs and at a temperature of  $\sim 89\text{ K}$ .

In this phase it is important to reach the LAr temperature in the fastest way while keeping the temperature gradients on the inner detector within specifications ( $\Delta T$  less than  $50^{\circ}\text{C}$  along the same vertical).

During the pre-cooling, a root pump ( $300\text{ m}^3/\text{h}$ ) forced the circulation of nitrogen gas through the cooling circuit. The temperature of the gas was progressively (automatically) decreased according to a preset ramp down by injection of increasing amounts of LN<sub>2</sub> in the main gas flow. Thanks to the low GN<sub>2</sub> thermal capacity, a smooth cooling of the piping and the surrounding materials was achieved, thus avoiding the thermal stress that would have otherwise been caused by the abrupt injection of LN<sub>2</sub> in the cooling circuit.

Being the first time that the cryostat was cooled, a prudential approach was adopted by halving the ramp down slope with respect to the foreseen nominal procedure at detector start-up. The negative counterpart of this choice is an extra pollution of the LAr volumes caused by the

outgassing of the internal surfaces at relatively high temperatures for a longer time period.

The input temperature of the gas decreased from room temperature to  $-150^{\circ}\text{C}$  in 9 days by applying a slow rate at the beginning ( $-0.5^{\circ}\text{C}/\text{h}$ ) and then increasing it up to  $-2^{\circ}\text{C}/\text{h}$  as the input temperature was decreasing (the thermal contraction coefficients of the materials decrease at low temperatures). The input temperature was then left constant for the following 2 days until an equilibrium was almost reached between the cooling power of the pre-cooling system and the heat injected through the insulation.

After 10 days the average temperature of the inner detector structures was about  $-50^{\circ}\text{C}$  (Fig. 57) with a maximum temperature difference of about  $25^{\circ}\text{C}$  (Fig. 58). At this point the pre-cooling system was stopped and the LN<sub>2</sub> injection started by activating the LN<sub>2</sub> circulation pump in the circuit of the first half-module. The second half-module, not to be filled with LAr, was cooled by the first one through thermal conduction. The second pump and the circuit of the second half-module were activated only at the end of the test run for a LN<sub>2</sub> consumption rate measurement. After injection of LN<sub>2</sub> in the cooling circuit the internal temperatures started to decrease quite rapidly.

Fig. 57 shows the measured temperature inside the cryostat (top) and on the outside wall (bottom) during the cooling phase. The temperature differences in the cryostat measured within the different PT1000 groups (Section 9.4) and the maximal difference between any two internal PT1000 sensors are reported in Fig. 58. The observed highest temperature differences exceeded the upper limit for the temperature difference of  $50^{\circ}\text{C}$ . This largest difference occurred during the LN<sub>2</sub> injection due to the high cooling speed, and required to stop the process for some time, in order to avoid exceeding too much the specified maximum gradient on the inner detector structures.

After a stop of about 10 h the LN<sub>2</sub> circulation in the cooling circuit restarted, allowing 1 day later, to start the LAr transfer in the main volume. The gradients became smaller when the filling procedure of the cryostat with LAr started. The largest temperature difference reached all over the inner

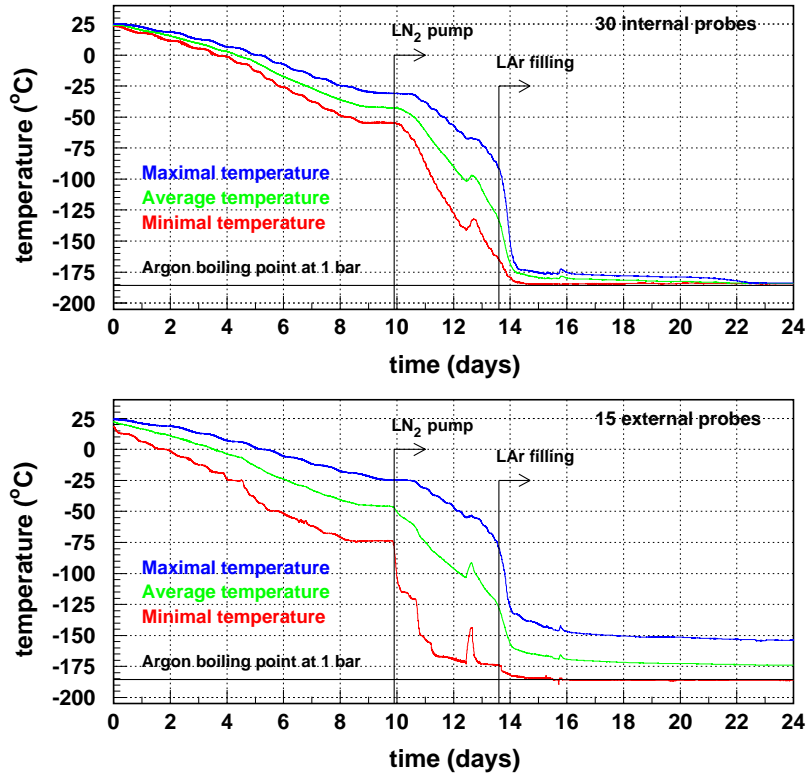


Fig. 57. Top: highest, lowest and average temperatures in the cryostat during the cooling phase, measured by the 30 internal PT1000 sensors. Bottom: highest, lowest and average temperatures measured by the 15 PT1000 sensors placed on the external side of the cryostat walls. The Argon boiling point is also shown.

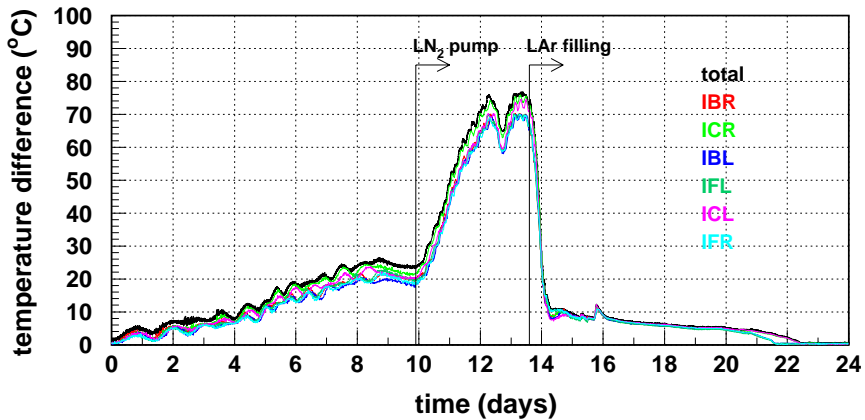


Fig. 58. Measured temperature differences during the cooling down of the detector, between any two internal PT1000 sensors (total), and within the different PT1000 groups. The arrows mark the starting of the LN<sub>2</sub> circulation and of the LAr filling (see Section 9 for the sensor's labelling).

detector was about 77°C. The measured movement of the springs attached to the wires of the chambers were all smaller than 300  $\mu\text{m}$  during the cooling procedure and even over the whole test run period.

#### 14.1.3. Filling

During the cooling process the pressure of the argon inside the main volume was kept to at least 70 mbar above atmospheric pressure to minimize the risk of air contamination or leaks caused by possible cracks from the relative movements following the thermal contraction of components. The water content in the argon volume was periodically measured by means of a hygrometer installed on one of the top flanges. At the end of the pre-cooling phase the water contamination was about 10 ppm and decreased to about 6 ppm during the first day of cooling down with LN<sub>2</sub>. About 1 day before starting the filling of the cryostat the two argon gas recirculators were activated for the rest of the test run.

The gas in the main volume was recirculated about 3.5 times, with a total recirculation rate of about 40 m<sup>3</sup>/h in the 24 h preceding the filling. The corresponding reduction of impurities (assuming 100% efficiency for the absorption from the filters, and perfect gas mixing) was more than a factor 30. The water content measured just before start filling with LAr was below the sensitivity of the instrument (2 ppm). An independent measurement performed with one of the purity monitors installed in the inner detector and operated in gas showed correspondingly an increase of the electrons' lifetime in the argon gas from  $\sim 50$  to  $\sim 900$   $\mu\text{s}$ , namely by a factor 18, compatible with the estimates. Absolute values, however, do not have an immediate interpretation since measurements with purity monitors in gas are affected by large uncertainties from geometrical effects. Moreover, there is no simple relationship between the electron capture cross-sections in the gas and in the liquid phases.

In the gaseous phase cross-sections depend rather strongly on the applied electric field and the dependence changes with the type of impurities. The quality of argon at the entrance of the purifier units was periodically monitored by means

of a gas chromatograph (H<sub>2</sub>O and O<sub>2</sub> concentration sensitivity  $\leq 0.2$  ppm). The same instrument was also connected to the output of the first purifier unit and provided a rough check of its functionality. The measurements performed during the filling phase indicated a quite good quality of the supplied LAr (H<sub>2</sub>O and O<sub>2</sub> concentration  $\leq 0.3$  ppm).

The filling operation itself was quite simple and smooth. When the mean temperature inside the cryostat went below  $-150^\circ\text{C}$  an increasing amount of argon gas and, at given point, of LAr was injected to compensate for the de-pressurization of the main volume. Argon was always taken from the liquid outlet of the external storage in order to have the best gas quality. When the liquid started to fill the main volume, due to the contact with hotter materials (still a few tens of degrees centigrade above the LAr temperature) the pressure suddenly increased and, by opening some manual valves on top of the container, this fast evaporation partially evacuated the internal volume from the gas that remained in the container during the cooling phase. The valves were left partially open during the filling to allow for the exhaust of the gas coming from flushing and to increase the filling speed.

By regulating the pressure of the external storage dewar one could set the filling rate to the specified nominal value (2 m<sup>3</sup>/h). However, limited by the external supply capability, the average filling speed was about 1 m<sup>3</sup>/h, corresponding to a LAr level increase of about 1.5 cm/h (Fig. 59).

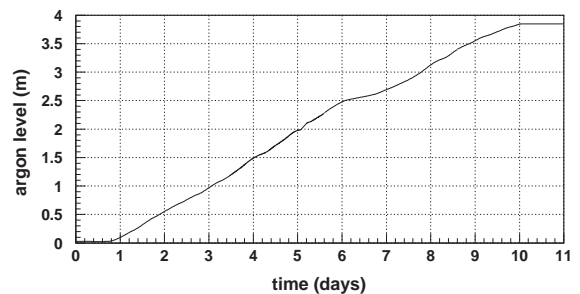


Fig. 59. LAr level in the cryostat as a function of time during the filling procedure.

Due to the LAr static pressure the cryostat walls were deformed outwards by about 11 mm on average.

Most important at the end of the filling was the precise setting of the LAr level in the cryostat which has to lie within the safety limits. The upper limit is imposed by the requirement that enough space has to be left free to allow for the LAr thermal expansion, when the equilibrium pressure raises to the maximum allowed (1.45 bar abs before the opening of the safety valves). This corresponds to a volume (level) increase of 0.7% when the equilibrium pressure goes from 1 bar absolute to 1.5 bar absolute. Considering the extra volume needed for boil off and adding a safety margin one could define the expansion volume as 1.5% of the total LAr volume. This corresponds to a free space of 65 mm from the ceiling of the LAr container. The lower limit ensures the covering with LAr of all the detector parts at HV, especially the field-shaping electrodes (race tracks) and the bottom end of the HV feedthrough. Should the LAr level go below this limit, spark discharges could cause irreversible damage to the HV system. For this reason an alarm was issued in case of a LAr level outside the allowed limits.

The filling lasted about 10 days. The gas evacuation valves on top of the container were progressively closed in the few hours following the filling completion. The LAr level was set at  $65 \pm 5$  mm from the container ceiling. Figs. 60 and 61 show, respectively, the measured variation of the LAr level and of the LAr temperature in the cryostat during the period following the filling. In the first 10 days the LAr was still being cooled down, resulting in a contraction of the LAr volume and hence in a decrease of the LAr level. However, after the equilibrium temperature was reached, the LAr level continued to decrease. Fitting a straight line to the data from day 10 of data taking to day 58 one obtains a decreasing rate of the LAr level of  $0.570 \pm 0.001$  mm/day corresponding to  $39.6 \pm 0.3$  l/day. This is likely due to leaks occurring on the top flanges after detector filling.

The disuniformity in the response of the TPC due to variations of the drift velocity is caused by the temperature gradient in the LAr. Thus, the

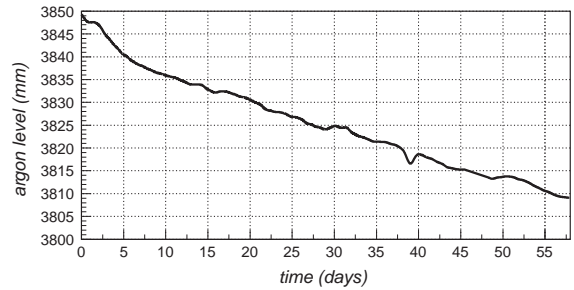


Fig. 60. LAr level as a function of time during the data taking period.

maximum temperature difference between any two points in the detector volume is required to be less than  $1^\circ\text{C}$ . No significant temperature difference between different LAr levels was found (Fig. 61, top). The largest difference measured between any two PT1000 sensors oscillated between  $0.5^\circ\text{C}$  and  $0.7^\circ\text{C}$  during the whole data taking period (Fig. 61, bottom).

#### 14.1.4. LAr purification after filling

The LAr purity has been routinely measured during the Pavia test. The set of measurements provided a precise indication of the lifetime evolution during the run.

The free-electron lifetime in the LAr volume measured right after filling ranged from 30 to 60  $\mu\text{s}$  depending on the position; this is at the lower limit (or even below) of the sensitivity range of the purity monitors. These values were about a factor 2.5 lower than the nominal target value and are most likely a consequence of the increased pre-cooling time.

After filling with LAr and as soon as the pressure inside the main container was stabilized, the liquid recirculation started. A few days later, as the lifetime went definitively in the sensitivity range of the purity monitors, the positive trend of the LAr purity became evident (provided that the liquid and gas recirculation units were active) and the purity improved continuously up to the maximum lifetime value reached (1.8 ms).

The liquid recirculation could be operated together with the wire read-out, since no microphonic noise was observed. The behaviour of the

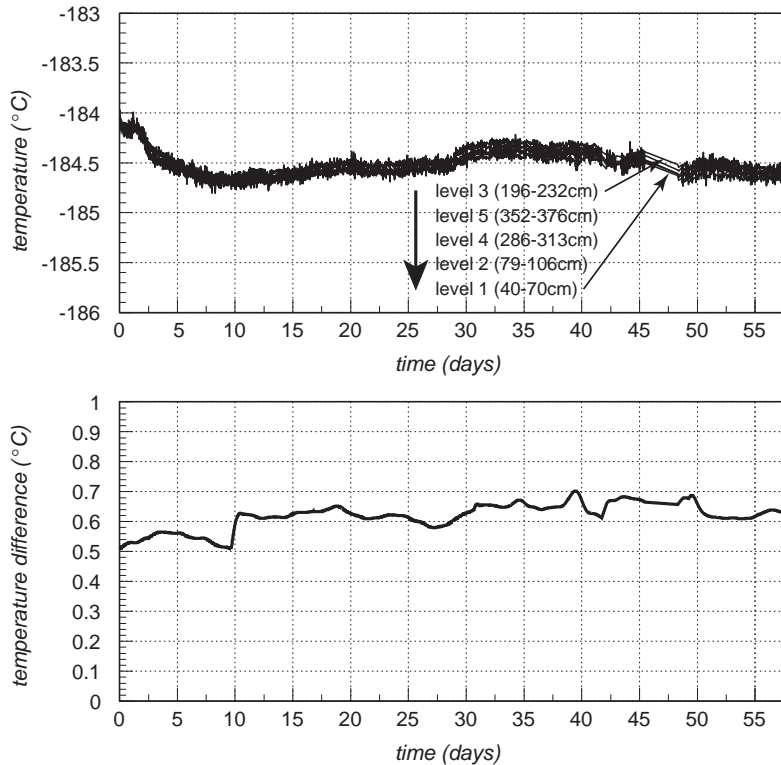


Fig. 61. Top: average LAr temperature measured at five levels during data taking. Indicated are the height ranges of the different levels. Bottom: the corresponding largest temperature difference in the cryostat.

LAr contamination during the 2 months of detector life-time was studied in Ref. [20].

#### 14.2. Detector commissioning

The chamber read-out electronics and the HV distribution for the wire planes were tested after detector filling. Dead channels were replaced (about 1%) and a few others (some tens), dead for shorts on the internal crimping connectors, were excluded from the HV distribution. The voltage setting on the wire planes at this stage was:

- 0 V on the Induction-1 plane (horizontal wires, facing directly the cathode);
- +180 V on the Induction-2 plane (wires at  $-60^\circ$ , middle plane);
- +420 V on the Collection plane (wires at  $+60^\circ$ ).

The HV on the cathode was raised with a programmed ramp-up slope of  $-0.5$  kV/min up

to  $-112.5$  kV (1.5 times the nominal running voltage) to verify the safe running at  $-75$  kV. After 1 hour the voltage was lowered (ramp-down slope = 1 kV/min) down to the working voltage of  $-75$  kV (500 V/cm electric field).

Data taking started when the electron lifetime was still below  $100 \mu\text{s}$ ; however, short tracks occurring near the wire planes were already visible. The inner detector response was then optimized by searching for sources of noise, ground loops, etc. The field configuration between the wire planes was then changed during this period to optimize the transparency and the signal-to-noise ratio on all the wire planes. The final voltage setting was:

- $-220$  V on the Induction-1 plane;
- 0 V on the Induction-2 plane;
- +280 V on the Collection plane.

The optimization of the detector response was not pushed to the limit since the working conditions at

Gran Sasso will be significantly different. At the end of June 2001 the detector working conditions were judged to be satisfactory and the following month was dedicated to continuous data taking with cosmic-rays.

Several trigger conditions were defined using both the external trigger and the signals coming from the internal PMTs reading the scintillation light of the LAr, in order to collect a variety of event samples. During the data-taking period about 30 000 events were gathered by triggering on:

- long horizontal muon tracks;
- vertical muon tracks;
- energetic cosmic-ray showers;
- low-energy events.

Calibration runs were also performed by using test signals injected on the various test inputs of the electronics and distribution chains.

The HV system operated in a very stable and reliable way during the 2 months run. Effects of a possible residual power supply ripple (filtered by the custom made HV filter) were not observed and the characteristic switching frequencies of the power supply were absent in the frequency spectra of the wire signals (Fig. 43).

A test of the maximum power supply voltage (–150 kV) was performed successfully. This value was kept during 24 h to demonstrate, together with the electron lifetime of 1.8 ms, the feasibility of a detector configuration with a 3 m long drift path. This was the highest voltage ever tested in noble liquids. After the test the HV was lowered in steps of 15 kV down to zero. At each step data were collected with a trigger for particles crossing the active volume diagonally in a vertical plane containing the drift direction. The analysis of these data allowed to obtain a direct estimate of the drift velocity and an alternative check of the electron charge attenuation at different electric field values. The HV was then restored to –75 kV for the final period of data taking and finally brought to zero on 1st August, at the end of the test run.

#### 14.3. Cryostat draining and warming up

After completion of the test programme (cryogenics, HV, trigger, read-out) and of the data

taking, the cryostat was emptied of LAr. In a first phase the cooling system was kept working and the LAr was extracted at the bottom of the cryostat and transferred into trucks by static pressure. After about 75% of the LAr was taken out, the cooling system was stopped and the remaining argon was pushed out by the gas pressure. Only 10% of the LAr was lost (due to evaporation) during the emptying procedure.

The cryostat started to heat-up towards the external temperature when the cryostat was emptied (Fig. 62). At the beginning the cooling system was still working and both the absolute temperature and the maximum temperature difference were maintained low. When the LN<sub>2</sub> circulation pump stopped a large temperature difference up to a maximum of about 65°C was observed between the regions still immersed in LAr and the regions in gas. It took about 1 month for the whole detector to reach room temperature.

## 15. Exposure to cosmic-rays

### 15.1. Event imaging: charge read-out

In this section some of the events collected during the test run are shown and discussed to illustrate the detection features of the LAr TPC technique. We remind that one of the main goals of the test was to show the ability of detecting long muon tracks traversing the full detector length. This goal was achieved and the results have been published [19].

The Collection view of a cosmic-ray event composed of many parallel tracks is displayed in Fig. 63. The event extends up to the full length (about 18 m) and drift (1.5 m) of the detector, as shown in the upper image. The zoomed regions show several electromagnetic and hadronic showers, muon tracks and low-energy electrons from  $\gamma$ -conversion.

Some of the muons entering the detector deposit all their energy, stop and decay in the LAr active volume. This type of event can be easily recognized by the presence of a low-energy muon track followed by the emission of an electron. The low-momentum muon track undergoes large angle

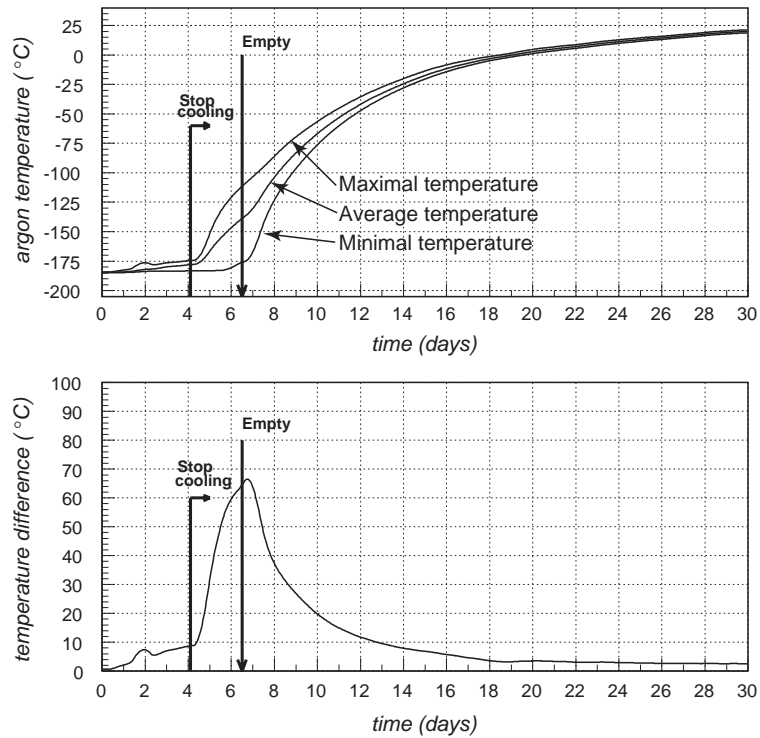


Fig. 62. Top: maximum, minimum and average temperature in the cryostat after the cooling stopped. Bottom: maximum temperature difference between any two measuring points inside the cryostat. The arrows mark the stopping of the cooling system and the moment when the cryostat is completely empty of LAr.

multiple scattering and the ionization rapidly increases near the end point. The electron energy ranges between 0 and about 53 MeV.

Fig. 64 shows the three views of an event matching the previous pattern. The muon extends about 60 cm in the increasing wire number coordinate. The last part of the track shows the increasing energy deposition figure, indicating that the muon stopped rather than decayed in flight. The short track corresponds to the emitted electron. The track shows many changes of direction, due to multiple Coulomb scattering. The fitted energy deposition of the electron is about 20 MeV.

Fig. 65 shows one view of a hadronic interaction inside the detector. A charged hadron enters the detector from the top and travels around 1 m in LAr before interacting. Several secondary particles are produced and undergo different interactions.

The cleanest image of the interaction is shown in the Collection view. A  $\delta$ -ray is produced at the beginning of the hadron track. Among secondary particles, the conversion of a pair of photons most likely coming from the decay of a  $\pi^0$  is evident at the bottom of the picture. A neutral particle (probably a neutron) is produced in the upper part of the figure giving rise to an additional hadronic interaction. One of the charged hadrons coming from the main interaction vertex travels about 1.7 m undergoing secondary hadronic interactions along its path. Secondary, heavily ionizing nuclear debris are also visible.

A good example of the imaging capabilities of the LAr TPC is given by the electromagnetic shower shown in Fig. 66. The real dimensions are about  $75 \times 170 \text{ cm}^2$ . The electron initiates an electromagnetic cascade (bottom-left corner of the figure) as pair production and bremsstrahlung

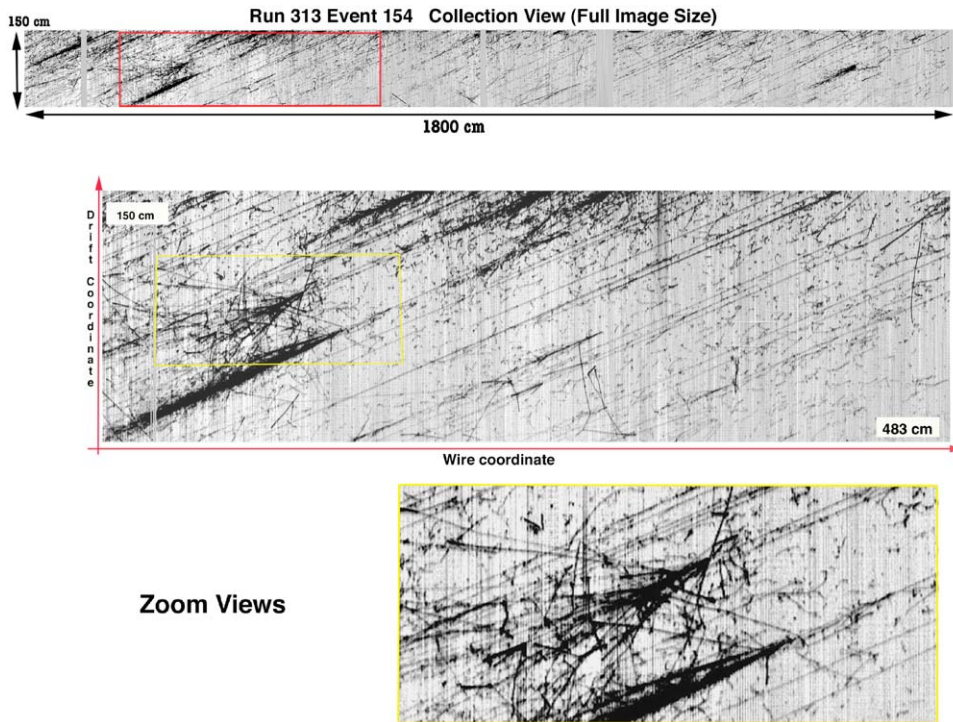


Fig. 63. Run 313, Event 154, Collection view. Extensive air shower.

generate more electrons and photons of lower energy. The grey level of the pixels codes the electronic pulse-height proportional to the collected charge, so that the longitudinal and transverse developments of the cascade can be studied. The black dots that appear all around the main shower are due to Compton electrons of very low energy ( $\sim 1$  MeV). This shows the excellent performance of the electronic LAr imaging. The overall drift time (vertical axis) corresponds to about 75 cm of distance. The shower spreads over about 15 radiation lengths.

### 15.2. Scintillation light read-out

An example of how the PMT information can be associated to the tracks reconstructed in the data analysis is shown in Fig. 67. The trigger logic based on the coincidence of at least four PMTs in the same chamber selects horizontal tracks. The time sampling of the four PMT outputs is shown in the plot on the right of the figure. Two PMTs

are positioned along the 18 m long wire chamber structure in correspondence of the ionization event shown in the left part of the figure. The image is only a detail (about  $1.5 \times 1.5$  m<sup>2</sup>) of the full drift volume. Three tracks (one of which is horizontal) can be easily recognized in the image. The PMT pulses that have induced the trigger signal for the data-acquisition generated by the horizontal track are identified in the data sampling at  $t \sim 0$   $\mu$ s. The pulses generated by the two additional tracks placed at time  $> 400$   $\mu$ s are present only in the PMTs (1 and 2) facing the event. This indicates that the tracks correspond to different events occurring in the drift volume at three different times.

## 16. Off-line event reconstruction

The purpose of the reconstruction procedure is to extract the physical information provided by the wire output signals, i.e. the energy deposited by the

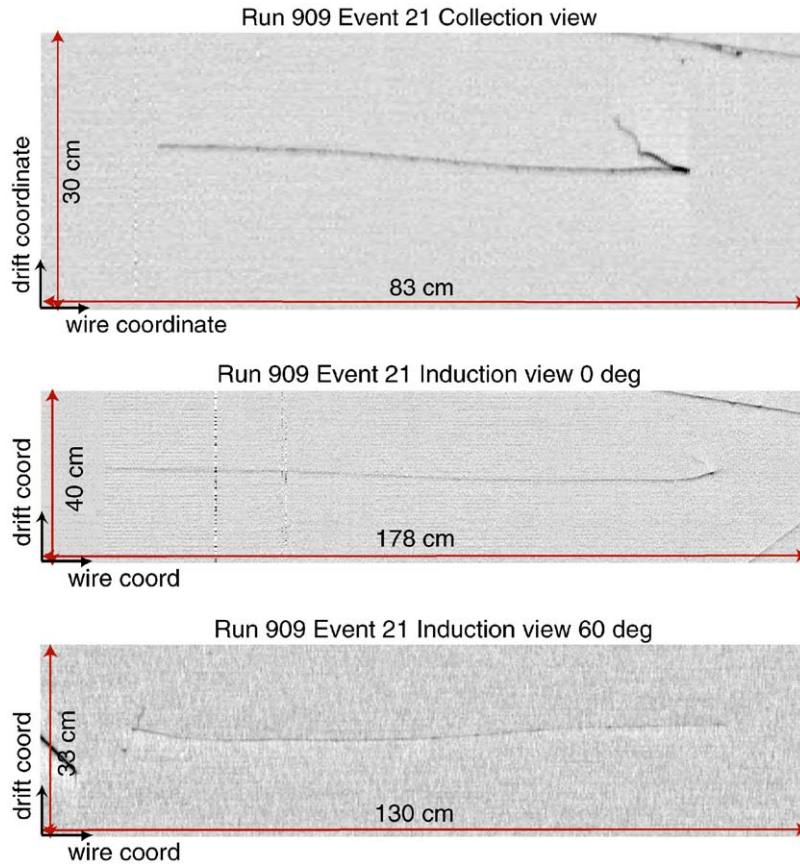


Fig. 64. Run 909, Event 21. From top to bottom: Collection, Induction-1 ( $0^\circ$ ) and Induction-2 ( $60^\circ$ ) views. Muon decay into electron.

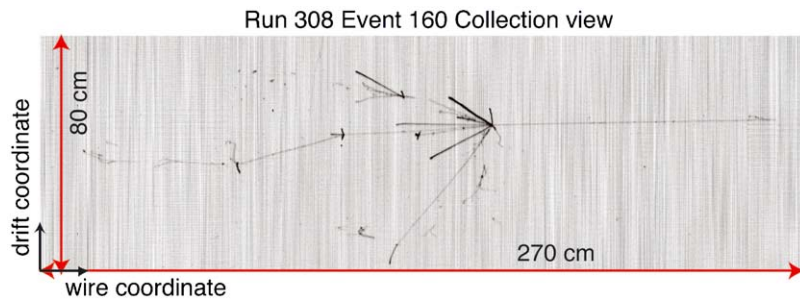


Fig. 65. Run 308, Event 160, Collection view. Hadronic interaction (see the text for the explanation).

different particles and the point where such a deposition has occurred, to build a complete 3D and calorimetric picture of the event. The basic building block of a track is called hit, defined as

the segment of track whose energy is detected by a given wire of the read-out wire planes.

The off-line reconstruction procedure consists of the following steps:

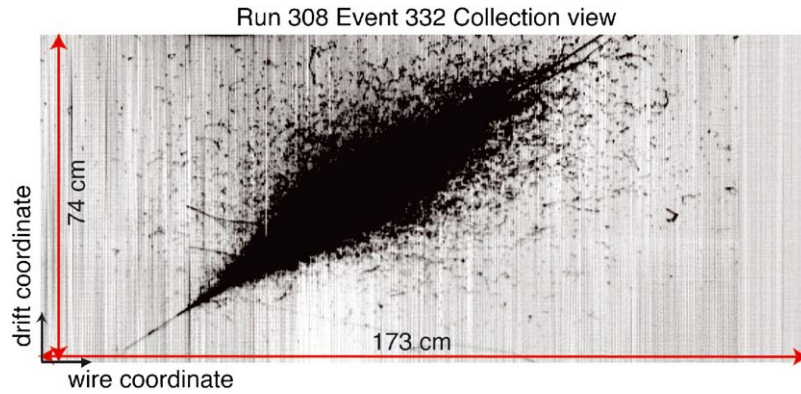


Fig. 66. Run 308, Event 332, Collection view. Electromagnetic shower.

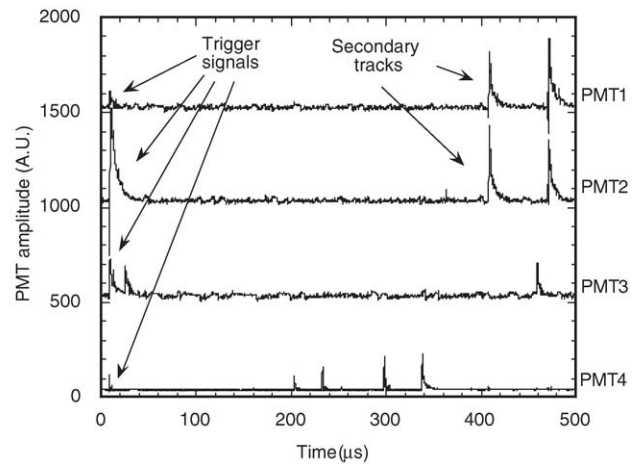
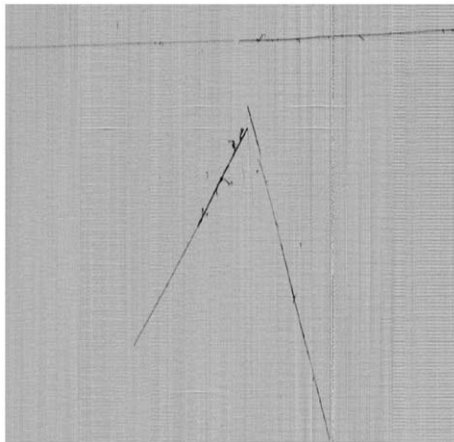


Fig. 67. Time structure reconstruction in the T600 detector (see the text for details).

- *hit identification*: the hits are independently searched for in every wire as output signal regions of a certain width above the baseline output value;
- *fine hit reconstruction*: the parameters defining the hit (position, height, area), which contain the physical information, are precisely determined;
- *cluster reconstruction*: hits are grouped into common charge deposition distributions based on their position in the wire/drift coordinate plane;
- *3D hit reconstruction*: the hit spatial coordinates are reconstructed by using the association of hits from different views into common track segments.

In this section, we describe the different steps of the hit reconstruction procedure.

### 16.1. Hit identification

The hit identification aims at distinguishing signals produced by ionization electrons from

electronic noise. Hits are identified as signal regions of a certain width with output values above the local mean. The hit identification procedure also establishes rough preliminary bounds to the hit range along the drift coordinate, which will be of utmost importance in ulterior steps of the reconstruction procedure. No information from adjacent wires is used at this stage.

Each sample is compared to its local mean. A value above the local mean by more than *threshold* samples triggers a hit candidate. The hit candidate is built with all the subsequent output samples above the threshold and is characterized by its width, i.e. the distance (in drift samples) between the hit initial and final points. Rejection of fake (noise) candidates is achieved by imposing a minimal width value of *width* samples. Further rejection can be carried out for Collection and Induction-1 wires, where the hits are expected to have an exponential falling slope. An extra requirement on the minimum distance from the peak position to the hit end (*fall*) is imposed. Fig. 68 illustrates the meaning of the hit search

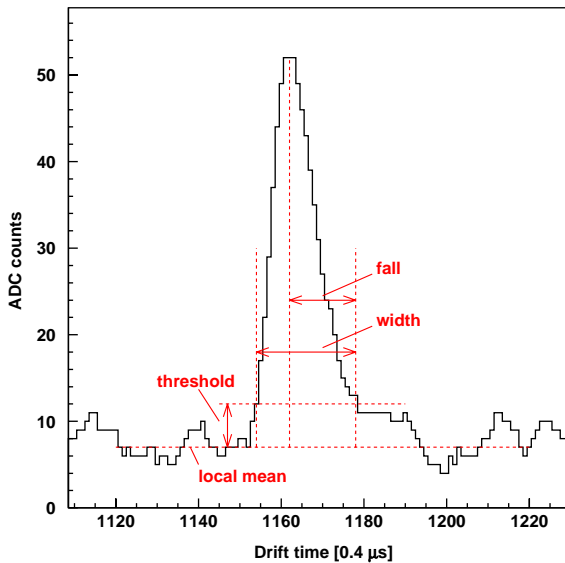


Fig. 68. Example of a hit produced by a minimum ionizing particle on a Collection wire. Marked are the parameters used in the hit search. The output signal has been passed through the low frequency filter.

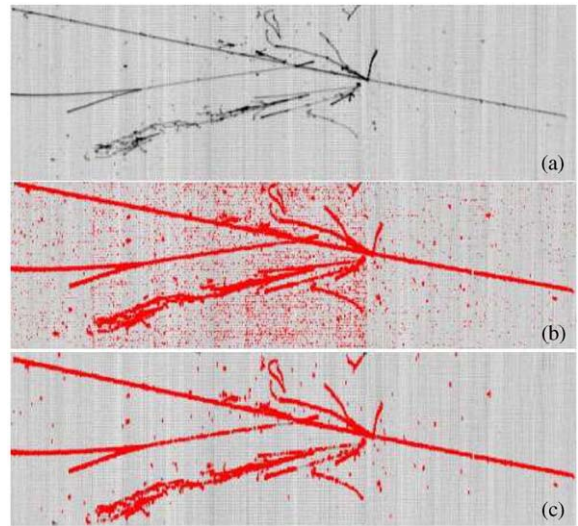


Fig. 69. Illustration of the effect of the free parameter values on the hit finding algorithm. Top: grey scale mapping of the output signal in a selected region of the Collection view. Middle: in bold, hits found with a loose selection of the free parameters. Bottom: in bold, hits found with the optimized parameters.

parameters. Fig. 69 shows the effect of the optimization of the parameter values on the hit finding algorithm.

Once the hit has been detected, a finer hit reconstruction is performed aiming at extracting in a optimal way the parameters defining the hit (position, height, area) which contain the physical information of the original associated track segment. The hit spatial reconstruction is entirely based on the determined hit peak position, whereas the hit area in Induction-1 and Collection wires (or height in Induction-2 wires) is proportional to the energy deposited by the ionizing particle, and therefore constitutes the base of the calorimetric reconstruction.

The approach (hit fit method) consists in performing a fit of the output signal around the hit region with an analytical function that reproduces well the hit shape, and in extracting the parameter values from the fitted function. This method requires the determination of a optimal window. This is illustrated in Fig. 70.

Once a proper window has been defined, the output signal within the window is fit using the

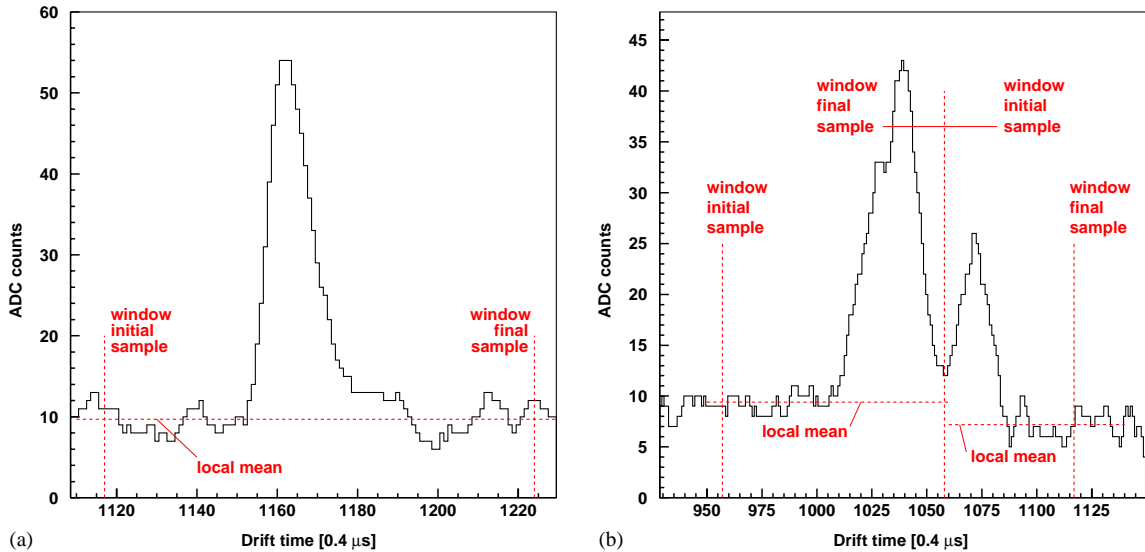


Fig. 70. Examples of computed local mean and hit windows for an isolated hit (left) and two close hits (right).

following analytical function of the drift time  $t$ :

$$f(t) = B + A \frac{e^{-(t-t_0)/\tau_1}}{1 + e^{-(t-t_0)/\tau_2}}$$

where  $B$  is the baseline,  $A$  the amplitude,  $t_0$  the point for which the height of the function with respect to the baseline is equal to  $A/2$ , and  $\tau_1$  and  $\tau_2$  are related to the falling and rising characteristic times, respectively. Fig. 71 illustrates how well this function fits the signals.

## 16.2. Cluster reconstruction

A cluster is defined as a group of adjacent hits within the wire/drift coordinate plane. The goal of the cluster reconstruction is to perform a first grouping of hits belonging to common charge deposition distributions, such as tracks or showers. Clusters provide identification criteria for the different patterns, and thus determine which reconstruction procedure must be followed. Clusters also provide a criterion for discrimination between signal and noise hits, based on the cluster hit multiplicity.

A *link* is defined as a pair of hits coming from consecutive wires and having overlapping drift

coordinate ranges, where the drift coordinate range of a hit is defined as the one computed by the hit finding algorithm (Section 16.1). Therefore, clusters can be defined as groups of hits with links among them. Links are also of great importance during the 3D hit reconstruction algorithm (Section 16.3).

Clusters are built in a two step approach. In the first step (pass I), preliminary clusters are built as groups of hits being connected by links. The second step (pass II), attempts to expand and merge together the clusters found in pass I, in order to reduce the number of the resulting clusters. The reconstruction algorithm takes as input a list of hits from a given wire plane, and constructs all possible clusters out of them, using only the information obtained by the hit finding algorithm.

In pass I, a preliminary grouping of the hits to a cluster is performed. The goal of cluster reconstruction pass II is to expand and join cluster fragments produced by pass I. It proceeds as follows: the regions around the cluster borders are examined (where a cluster border is defined as a hit linked at most with one hit within the cluster). The cluster fragments found are merged hence elim-

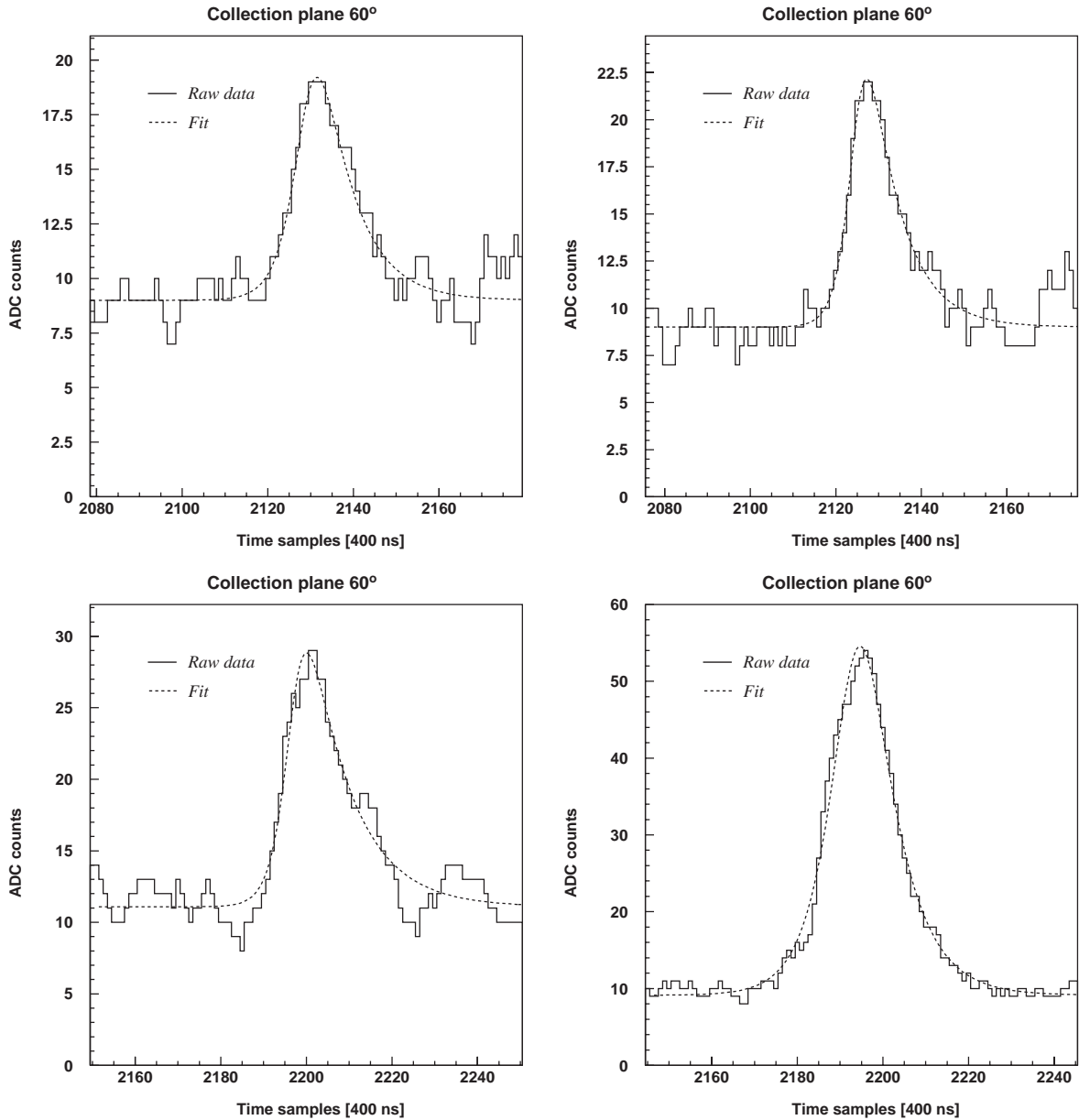


Fig. 71. Fitted signals from four hits along the track of a muon stopping inside the detector (Collection view).

inating the fragmentation produced in pass I. When no clusters are found, new hits are searched for in the region close to the cluster borders and are added to the cluster, hence reducing the cluster fragmentation caused by hit misidentification. Attempts for clusters merging/expansion are per-

formed both along the wire and the drift time coordinate directions.

Once no further expansion along the wire coordinate is possible for any of the existing clusters, the merging of clusters along the drift coordinate direction is attempted. For that, the

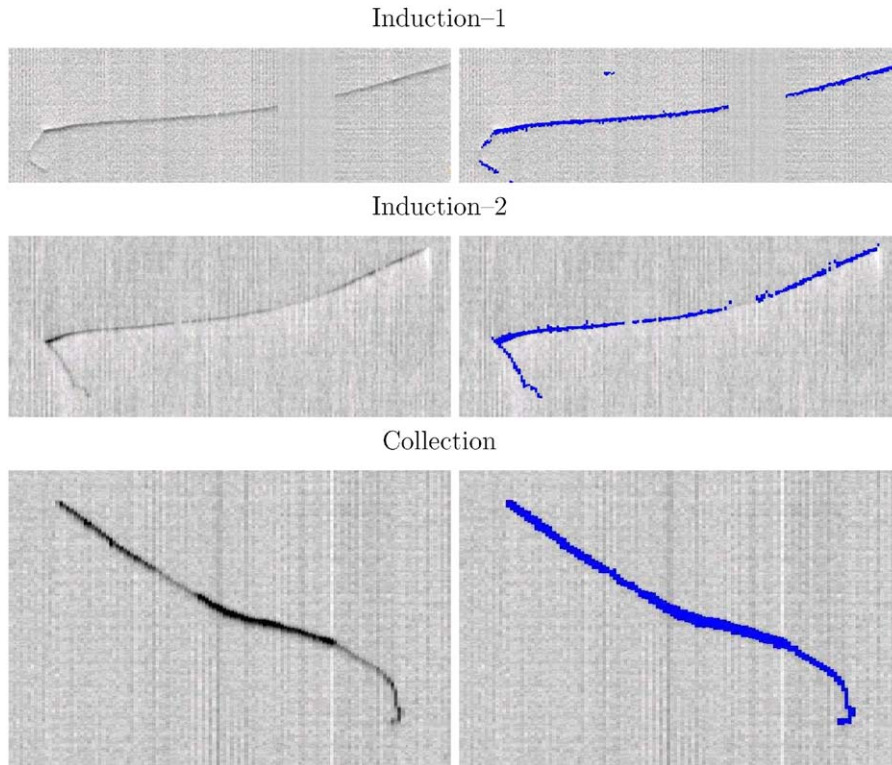


Fig. 72. Run 939, Event 95. Example of the performance of the cluster reconstruction algorithm on a stopping/decaying muon event for the Induction-1 (top), Induction-2 (middle) and Collection (bottom) views. Left: grey scale representation of the wires output signal in the wire/drift time plane. Right: in bold, hits associated to any reconstructed cluster.

hits at the maximal and minimal drift coordinate values are compared among different clusters. Cluster merging is carried out for those pairs of clusters for which their respective minimal and maximal drift coordinate hits are in the same or consecutive wires, and whose drift coordinate ranges overlap.

The overall performance of the clustering is illustrated in Fig. 72.

### 16.3. 3D hit reconstruction

The goal of the 3D reconstruction of a hit is the determination of the space coordinates of the different energy deposition segments produced by the ionizing tracks traversing the LAr-sensitive volume. Each wire plane constrains two spatial degrees of freedom of the hits, one common to

all the wire planes (the drift coordinate) and one specific for each plane (the wire coordinate). The redundancy on the drift coordinate allows the association of hits from different planes to a common energy deposition, and together with the wire coordinates from at least two planes, allows the hit spatial reconstruction of the hit.

We define the Cartesian reference frame as in Fig. 73. These coordinates are related to the wire and drift coordinates by means of the following expressions:

$$x_{1,2} = \frac{p}{2 \cos \theta_w} (w_1 - w_2 + w_0)$$

$$x_3 = pw_3$$

$$y = \frac{sv}{f}$$

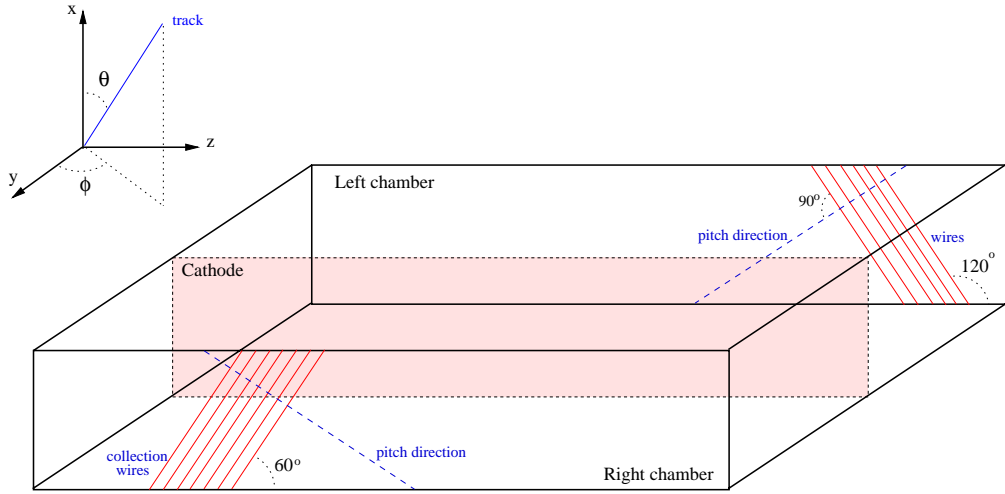


Fig. 73. Sketch of the first half-module and the Cartesian reference frame.

$$z_{1,2} = \frac{p}{2 \sin \theta_w} (w_1 + w_2 - w_0)$$

$$z_{2,3} = \frac{p}{\tan \theta_w} \left( w_3 + \frac{w_2 - w_0}{\cos \theta_w} \right)$$

$$z_{1,3} = \frac{p}{\tan \theta_w} \left( \frac{w_1}{\cos \theta_w} - w_3 \right)$$

where the constants entering the formulae are the following:  $p$ , the wire pitch at LAr temperature;  $\theta_w$ , the angle of the Induction-2/Collection wires with respect to the horizontal (in the range  $[0, 90^\circ]$ );  $w_0$ , half the number of wires from the Induction-2 (Collection) planes intersecting with a wire from the Collection (Induction-2) plane; and  $f$ , the read-out sampling frequency.

The values of the constants are summarized in Table 10.  $v$  is the electron drift velocity, which depends on the drifting field and the LAr temperature.

$w_1, w_2, w_3$  and  $s$  are related to the indices of the wires sensing the hit in the different wire planes and the drift time coordinate (in number of samples), respectively.  $w_1$  corresponds to the wire index in the  $60^\circ$  wire plane whose wire number 0 is placed at coordinates  $(x, z) = (0, 0)$ ;  $w_2$  is the index of the wire sensing the hit in the complementary  $60^\circ$  wire plane (with wire number 0 at

Table 10  
Values of the constant parameters entering the formulae for the 3D Cartesian coordinates

Parameter	Value
$p$	2.991 mm
$\theta_w$	$60^\circ$
$w_0$	528
$f$	2.5 MHz

$(x, z) = (x_{\max}, 0)$ ). Finally,  $s = s^0$  (where  $s^0$  is the drift coordinate) for the left chamber, and  $s = 2S_{\max} - s^0$  (with  $S_{\max} = 4096$  the total number of samples in an event) for the right chamber.

The possibility of multiple determinations of  $x$  and  $z$  coordinates is due to the presence of three wire planes, providing each of them a two dimensional projection of the event. The combination of the different values results in an improvement on the precision of  $x$  and  $z$  coordinates determination. On the other hand, any combination of wire coordinates from two wire planes, together with the drift sample coordinate allows the determination of the spatial position of a hit within the LAr active volume.

The 3D reconstruction of hits performs efficiently on events of low track multiplicity composed of tracks (not necessarily straight). Since it is

purely based on topological criteria, the reconstruction method is not meant to be carried out on events with more complex energy deposition patterns, such as electromagnetic or hadronic showers. For this kind of event, a method combining spatial and calorimetric relations among hits needs to be developed.

We present some examples of the performance of the spatial reconstruction algorithm on events of different nature. The presented figures show different views of the reconstructed hits in their spatial positions, joined by lines representing the links between the hits.

Fig. 74 shows two views of a muon decay event (Fig. 72 for the initial wire/drift plane views). Figs. 75 and 76 illustrate the hit spatial reconstruction performance on straight line muon tracks, where it is important to stress the reconstruction of

the  $\delta$ -ray sub-track. Finally, Figs. 77 and 78 depict the reconstruction of simple low-multiplicity hadronic interaction events, where all the tracks and interaction vertices have been properly reconstructed.

## 17. Conclusions

We have presented a detailed description of the ICARUS T600 detector, a large-mass LAr TPC meant as the basic unit for a 3000 ton astroparticle observatory and neutrino detector to be installed in the underground Gran Sasso Laboratory.

The design, the description of the basic components, assembly, start-up and run procedures of the detector have been given, as well as the demonstration of the off-line event reconstruction

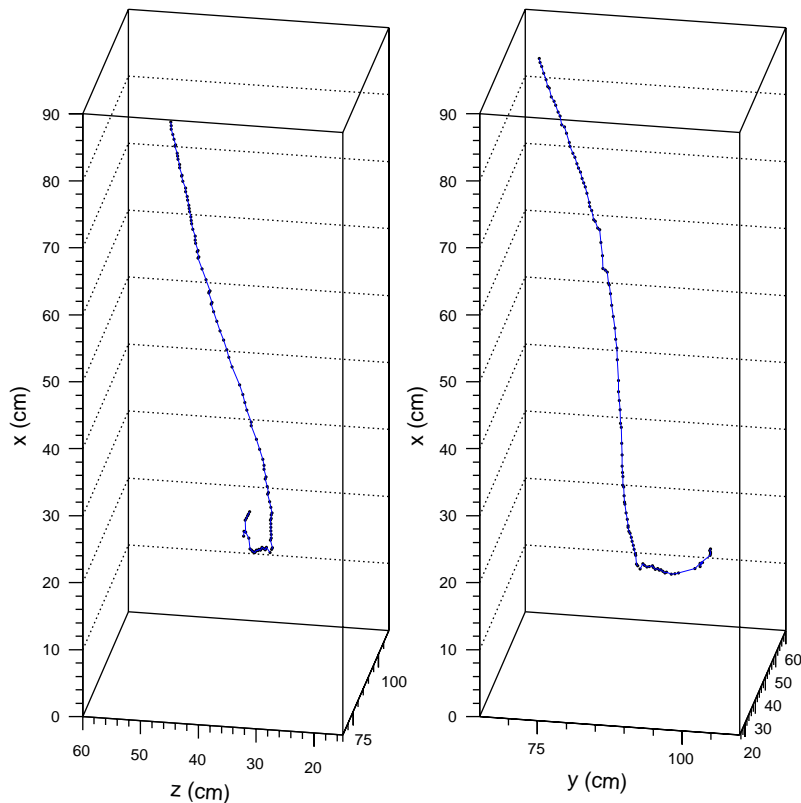
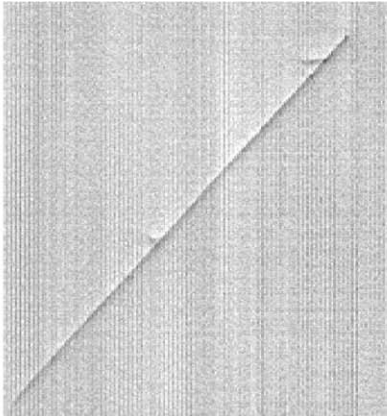
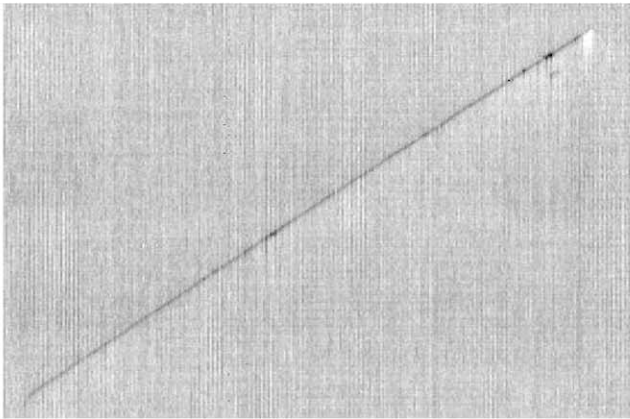


Fig. 74. Muon decay event. The pictures show two different views of the 3D reconstructed hits (dots) together with the links established among them (lines). The corresponding 2D projections provided by the wire planes are shown in Fig. 72.

Induction-1



Induction-2



Collection

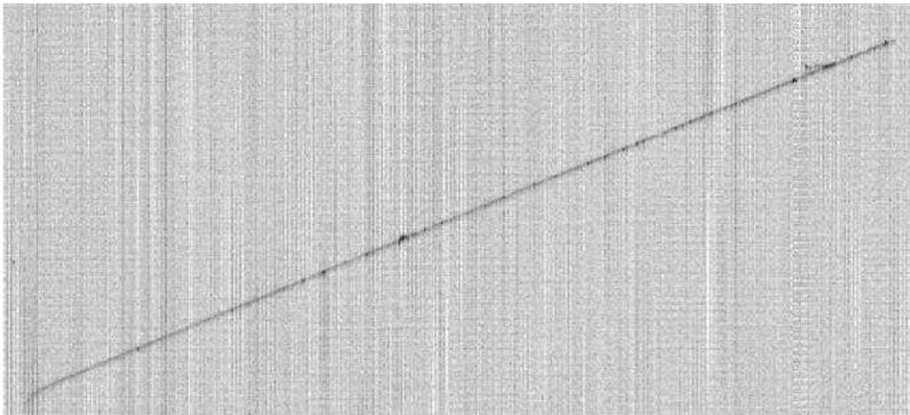


Fig. 75. Passing through muon with a  $\delta$ -ray emission. From top to bottom, Induction-1, Induction-2 and Collection view projections. The pictures are a grey scale representation of the output signal in the drift coordinate (vertical) versus wire (horizontal) plane.

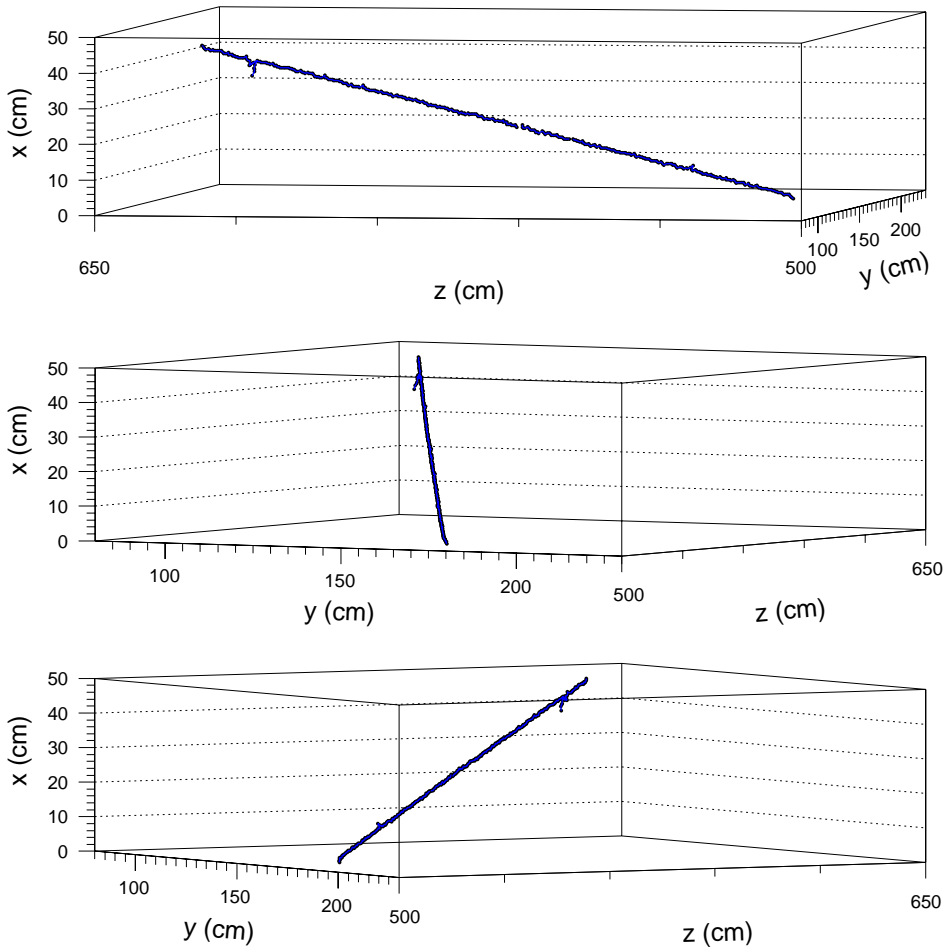


Fig. 76. Passing through muon event with a  $\delta$ -ray emission. The pictures show three different views of the 3D reconstructed hits (dots) together with the links established among them (lines). The corresponding 2D projections provided by the different wire planes are shown in Fig. 75.

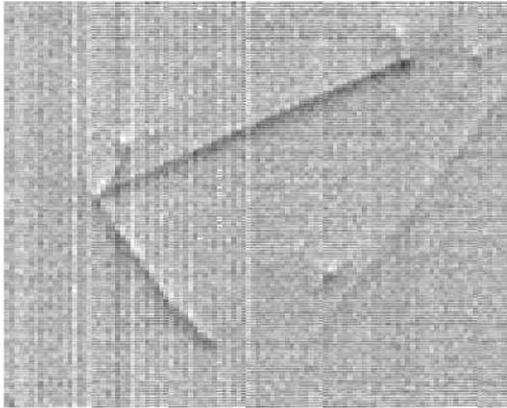
capabilities. The motivations of the design choices have been illustrated and justified for each relevant parameter. Results and figures of merit obtained during the final test run at surface in the Pavia experimental hall have been presented and discussed.

The main conclusion is that the measurements and the experimental results demonstrate that it is feasible to master all technical issues related to the construction and operation of a large size LAr TPC, within and sometimes beyond the design specifications:

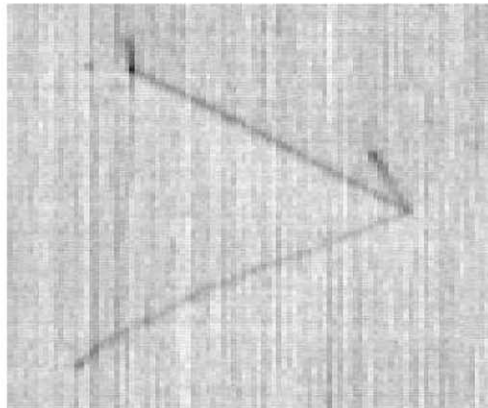
- LAr handling and purification;
- wire chambers mechanical construction;
- HV system for the electron drift;
- electronic noise;
- scintillation light detection;
- triggering, read-out and data handling;
- detector monitoring and control.

The collection of events shown in the last sections gives only a flavour of the detector imaging capability and of its calorimetric performance. The detector space and energy resolution,

Induction-1



Induction-2



Collection

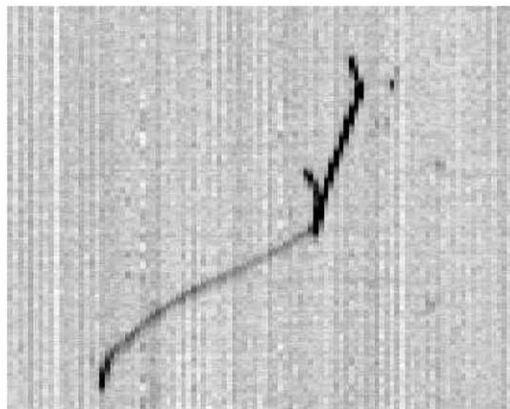


Fig. 77. Low-multiplicity hadronic interaction. From top to bottom, Induction-1, Induction-2 and Collection view projections. The pictures are a grey scale representation of the output signal in the drift coordinate (vertical) versus wire (horizontal) coordinate.

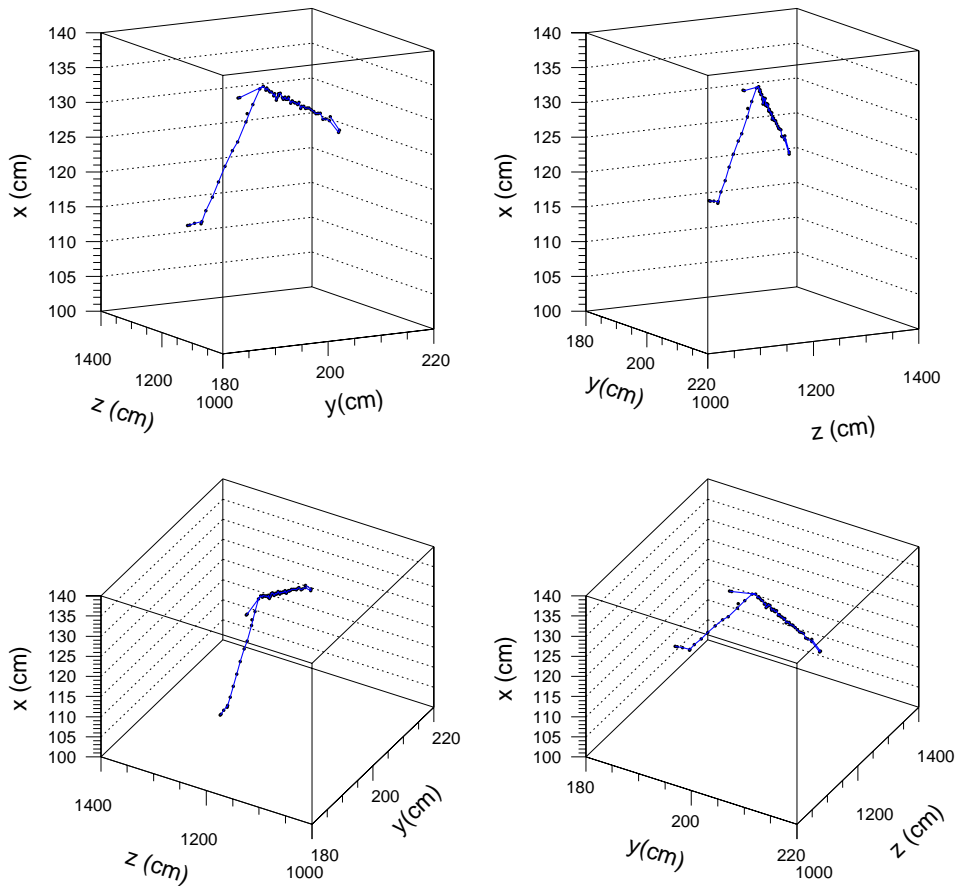


Fig. 78. Low-multiplicity hadronic interaction. The pictures show four different views of the 3D reconstructed hits (dots) together with the links established among them (lines). The corresponding 2D projections provided by the different wire planes are shown in Fig. 77.

particle identification and full events reconstruction are the subjects of several analyses that are currently being carried out with the events collected during the test run. From preliminary results one can anticipate that the T600 event reconstruction capabilities are analogous to those of smaller scale prototypes.

The adoption of fully industrial techniques for the detector construction, together with the very positive results of the test run, lead to serialization as an immediate solution for the extension to much larger active masses. The T600 is going to be transported to the INFN Gran Sasso Underground Laboratory where it will start to take data with atmospheric and solar neutrino interactions.

## Acknowledgements

We would like to warmly thank the technical collaborators which contributed to the construction of the detector and to its operation. In particular, we are indebted to A. Capsoni and F. Vercellati for the mounting of the inner detector, to S. Bricola, T. Locatelli, C. Marciano, G. Musitelli, R. Nardó and P. Novelli for the construction and operation of the wiring device, to B. Romualdi, A. Rotilio and E. Tatananni for their contribution to the realization and the installation of the purity monitor systems, and to S. Marchini and M. Negrello for their activities on the read-out electronics. A special thank goes to

M. Cominardi of BREME TECNICA for the skill and competence he showed in the design and in the technical direction of the mounting operation for the inner detector. Finally, we wish to acknowledge the work of the many people who contributed to the development of the ICARUS technology during the many years of R&D phase that made possible the realization of the T600 detector. We are glad of the financial and technical support of our funding agencies and in particular of the Istituto Nazionale di Fisica Nucleare (INFN), Italy, of ETH Zürich and of the Fonds National Suisse de la Recherche Scientifique, Switzerland. The Polish groups acknowledge the support of the State Committee for Scientific Research in Poland, 2P03B09520, 2P03B13622, 105,160,620,621/E-344,E-340,E-77,E-78/SPS/ICARUS/P-03/DZ211-214/2003-2005; the INFN, FAI program; the EU Commission, TARI-HPRI-CT-2001-00149. The group of Granada has been kindly supported by the Ministry of Science and Technology (project FPA2002-01835).

## References

- [1] C. Rubbia, The Liquid-Argon Time Projection Chamber: A New Concept For Neutrino Detector, CERN-EP/77-08 (1977).
- [2] P. Benetti, et al., A 3 Ton Liquid Argon Time Projection Chamber, Nucl. Instr. and Meth. A 332 (1993) 395.
- [3] P. Cennini, et al., Performance of A 3 Ton Liquid Argon Time Projection Chamber, Nucl. Instr. and Meth. A 345 (1994) 230.
- [4] F. Arneodo, et al., The ICARUS 50 l LAr TPC in the CERN neutrino beam, arXiv:hep-ex/9812006.
- [5] F. Arneodo, et al., First observation of 140-cm drift ionizing tracks in the ICARUS liquid-Argon TPC, Nucl. Instr. and Meth. A 449 (2000) 36.
- [6] F. Arneodo, et al., Determination of through-going tracks' direction by means of delta-rays in the ICARUS liquid Argon time projection chamber, Nucl. Instr. and Meth. A 449 (2000) 42.
- [7] P. Cennini, et al., Detection of scintillation light in coincidence with ionizing tracks in a liquid Argon time projection chamber, Nucl. Instr. and Meth. A 432 (1999) 240.
- [8] F. Arneodo, et al., Performance evaluation of a hit finding algorithm for the ICARUS detector, Nucl. Instr. and Meth. A 412 (1998) 440.
- [9] P. Cennini, et al., A neural network approach for the TPC signal processing, Nucl. Instr. and Meth. A 356 (1995) 507.
- [10] P. Cennini, et al., Improving the performance of the liquid Argon TPC by doping with tetramethyl germanium, Nucl. Instr. and Meth. A 355 (1995) 660.
- [11] P. Benetti, et al., A 3D image chamber for the LAr TPC on multilayer printed circuit board, Nucl. Instr. and Meth. A 346 (1994) 550.
- [12] P. Benetti, et al., Argon purification in the liquid phase, Nucl. Instr. and Meth. A 333 (1993) 567.
- [13] A. Bettini, et al., A study of the factors affecting the electron lifetime in ultrapure liquid Argon, Nucl. Instr. and Meth. A 305 (1991) 177.
- [14] S. Bonetti, et al., A study of the electron image due to ionizing events in a two-dimensional liquid Argon TPC with a 24-cm drift gap, Nucl. Instr. and Meth. A 286 (1990) 135.
- [15] F. Arneodo, et al., Performance of the 10 m<sup>3</sup> ICARUS liquid Argon prototype, Nucl. Instr. and Meth. A 498 (2003) 293.
- [16] F. Arneodo, et al., Detection of Cherenkov light emission in liquid Argon, Nucl. Instr. and Meth. A 516 (2004) 348.
- [17] G. Aquistapace, et al., The CERN neutrino beam to Gran Sasso (NGS), CERN 98-02 and INFN/AE-98/05 (1998); R. Baldy, et al., The CERN neutrino beam to Gran Sasso, Addendum to report CERN 98-02, INFN/AE-98/05, CERN SL-99-034 DI and INFN/AE-99/05 (1999).
- [18] P. Aprili, et al., The ICARUS experiment: A second-generation proton decay experiment and neutrino observatory at The Gran Sasso Laboratory, Cloning Of T600 Modules To Reach The Design Sensitive Mass. (Addendum), CERN-SPSC-2002-027; ICARUS Collaboration, A second-generation proton decay experiment and neutrino observatory at The Gran Sasso Laboratory, LNGS-P28/2001; ICARUS Collaboration, A first 600 ton ICARUS detector installed at The Gran Sasso Laboratory, Addendum to Proposal by the ICARUS Collaboration, LNGS-95/10 (1995).
- [19] F. Arneodo, et al., Observation of long ionizing tracks with the ICARUS T600 first half-module, Nucl. Instr. and Meth. A 508 (2003) 287.
- [20] S. Amoruso, et al., Analysis of the liquid Argon purity in the ICARUS T600 TPC, Nucl. Instr. and Meth. A 516 (2004) 68.
- [21] S. Amoruso, et al., Study of the electron recombination in liquid Argon with the ICARUS TPC, Nucl. Instr. and Meth. A 523 (2004) 275.
- [22] S. Amoruso, et al., Measurement of the Muon decay spectrum with the ICARUS T600 liquid Argon TPC, Eur. Phys. J. C33 (2004) 233.
- [23] ICARUS Collaboration, Evaluation of the Muon multiple scattering in the ICARUS T600 detector, 2004, to be submitted.
- [24] T. Doke, et al., Nucl. Instr. and Meth. A 269 (1988) 291.
- [25] K. Hagiwara, et al., Particle data group, the review of particle physics, Phys. Rev. D 66 (2002) 010001.
- [26] A. Bideau-Mehu, et al., J. Quant. Spectrosc. Rad. Transf. 25 (1981) 395; G.M. Seidel, et al., Nucl. Instr. and Meth. A 489 (2002) 189.

- [27] W.F. Schmidt, *Liquid State Electronics Of Insulating Liquids*, CRC Press, Boca Raton, FL, 1997.
- [28] NIST—National Institute of Standards and Technology, NIST Chemistry WebBook, NIST Standard Reference Database N. 69, in: P.J. Linstrom, W.G. Mallard (Eds.), March 2003, Gaithersburg MD, 20899 (<http://webbook.nist.gov>).
- [29] G.L. Raselli, M. Rossella, C. Vignoli, A. Votano, LAr scintillation light detection in the ICARUS T600 apparatus, INFN Report FNT/AE-2001/12;
- C. Vignoli, *Studio Della Luce Di Scintillazione Dell'Argon Liquido Per La Determinazione Del Tempo Assoluto Degli Eventi Nel Rivelatore ICARUS*, Ph.D. Thesis, Univ. degli Studi di Pavia, AA 1995/1996 (in Italian).
- [30] G. Carugno, et al., *Nucl. Instr. and Meth. A* 292 (1990) 580.
- [31] J. Rico, *First study of the stopping Muon sample with the ICARUS T600 detector*, Ph.D. Dissertation, ETH 14906, 2002.